6-23-2020

Changing Mantle Sources and the Effects of Crustal Passage on the Steens Basalt, SE Oregon: Chemical and Isotopic Constraints

Nicole E. Moore

A. L. Grunder

Wendy A. Bohrson

Richard W. Carlson

I. N. Bindeman

Geochemistry, Geophysics, Geosystems

RESEARCH ARTICLE
10.1029/2020GC008910

Key Points:
- The Steens Basalt is derived from two distinct mantle sources: an enriched and a depleted component, contributing varying proportions throughout stages in time
- Isotope and trace element data support changes in magmatic processes over the life of volcanism, including variable recharge, fractionation, and assimilation
- Lower B Steens Basalt has unusually high osmium concentrations derived by scavenging of fractionated sulfides from passage of subsequent recharge magmas

Supporting Information:
- Supporting Information S1
- Table S1
- Table S2

Correspondence to:
N. E. Moore,
nicole.moore@pomona.edu

Citation:
Moore, N. E., Grunder, A. L., Bohrson, W. A., Carlson, R. W., & Bindeman, I. N. (2020). Changing mantle sources and the effects of crustal passage on the Steens Basalt, SE Oregon: Chemical and isotopic constraints. *Geochemistry, Geophysics, Geosystems*, *21*, e2020GC008910. https://doi.org/10.1029/2020GC008910

Received 10 JAN 2020
Accepted 18 JUN 2020
Accepted article online 23 JUN 2020

Changing Mantle Sources and the Effects of Crustal Passage on the Steens Basalt, SE Oregon: Chemical and Isotopic Constraints

N. E. Moore[1], A. L. Grunder[1], W. A. Bohrson[2,3], R. W. Carlson[4], and I. N. Bindeman[5]

[1]College of Earth, Ocean and Atmospheric Sciences, Oregon State University, Corvallis, OR, USA, [2]Department of Geological Sciences, Central Washington University, Ellensburg, WA, USA, [3]Department of Geology and Geological Engineering, Colorado School of Mines, Golden, CO, USA, [4]Earth and Planets Laboratory, Carnegie Institution for Science, Washington, DC, USA, [5]Department of Earth Sciences, University of Oregon, Eugene, OR, USA

Abstract Continental flood basalts are more prone to compositional modification from passage through thicker and (or) more felsic crust in comparison to their oceanic counterparts. The Steens Basalt in southeast Oregon (~17 Ma) is among the oldest and most mafic members of the Columbia River Basalt Group and provides a record of the early stages of flood basalt volcanism. We evaluate the balance of mantle sources in time during the onset of Columbia River Basalt Group magmatism and assess the effect of crustal passage using stratigraphically controlled Sr, Nd, Pb, Hf, Os, and O isotopic compositions, as well as whole rock major and trace element data.

Mixing models indicate that depleted and enriched mantle sources identified by previous workers contribute in varying proportions during the life of the magmatic system, with the greatest contribution by depleted mantle when eruption rate and presumed intrusion rate increase. During waxing, enrichment of $\delta^{18}O$ in some flows signals cryptic deep fractionation of abundant clinopyroxene followed by shallow fractionation of olivine ± clinopyroxene ± plagioclase. Os concentrations are among the highest worldwide at a given MgO (0.29–0.86 ppb at 6.0 to 10.9 wt.%). We argue that high Os results from scavenging of sulfides by recharging magmas passing through earlier crystallized magmas. Elevated $^{87}Sr/^{86}Sr$ in the latest stage supports modest assimilation of partial melts from mafic accreted terranes, facilitated by thermal priming of crust by persistent magmatism. This work provides a more detailed schematic view of the Steens Basalt magmatic system, from mantle origin through crustal staging.

Plain Language Summary Continental Flood Basalts are voluminous outpourings of basaltic lava from dozens to hundreds of fissures over a widespread area. Basalt is the type of magma that is formed from mantle melting and records chemical properties of the mantle from which it melted. Magmas that erupt at the surface that have undergone minimal changes during their traverse from mantle to crust retain many of the chemical properties of the mantle from which they were generated, in particular radiogenic isotope ratios, as these do not change during cooling and crystallization of magma. We present new radiogenic and stable isotope compositions for the Steens Basalt, among the earliest members of the Columbia River Flood Basalt Group, western United States, that gives insight into the mantle and crustal sources, and assess the magmatic processes that produced the Steens Basalt. The compositional changes in successively younger flows exposed at Steens Mountain record three distinct stages that track the onset, waxing, and decline of volcanism. Two chemically distinct mantle sources, one depleted and one enriched in isotopic character, contribute in varying proportions throughout the three stages. During these stages, varied cooling, crystallization, incorporation of crustal melts, and scavenging of previously crystallized mineral phases occurs.

1. Introduction

The very existence of vast, rapidly emplaced volumes of mafic magmas, expressed as large igneous provinces (LIPs), continues to generate debate about their origin and effects on Earth's mantle, crust, climate, and biological evolution. The processes that generate LIPs remain contentious. The thermal or compositional buoyancy of upwelling mantle anomalies that generate magmas are variously attributed to mantle plumes (aka hotspots; e.g., Richards et al., 1989), to meteorite impacts (e.g., Ingle & Coffin, 2004), or to continental

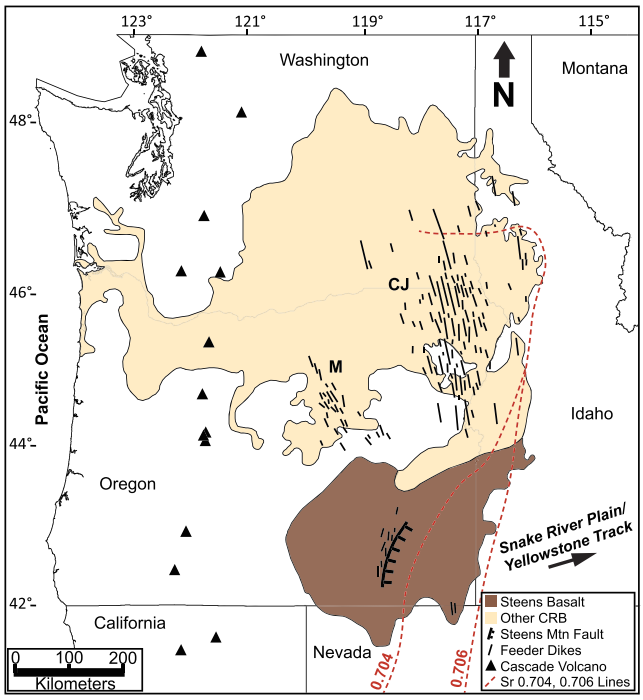

Figure 1. Regional map of the CRBG. Brown shaded region shows the full extent of Steens Basalt (Bondre & Hart, 2008; Brueseke et al., 2007; Camp et al., 2013); tan region is the remainder of the CRBG. Solid black lines are schematic feeder dikes; the Steens dikes near Steens Mountain, the Chief Joseph (CJ) swarm in Northeast Oregon and Southeast Washington, and the monument (M) swarm in north Central Oregon. Hatched curved black line is the highest relief segment of the Steens Mountain escarpment along the Steens fault, one of several north northeast striking normal faults in the northern basin and range province. Black triangles are the major Cascade volcanoes. Red dashed lines are the $^{87}Sr/^{86}Sr_i$ 0.704 (western line) and 0.706 (eastern line) isopleths (Pierce & Morgan, 2009); the 0.706 line is the inferred western boundary of the North American craton (Kistler & Peterman, 1973).

breakup (e.g., Carlson & Hart, 1987; Cox, 1978; McKenzie, 1984; White & McKenzie, 1989). Others suggest that LIPs may be formed by delamination of dense lithospheric crustal roots and resulting mantle upwelling (Anderson, 2005; Elkins-Tanton, 2005). Volume estimates for LIPs range from 2.1 × 10^5 km^3 (Columbia River Basalt Group, CRBG; Reidel et al., 2013) to 4.4 × 10^7 km^3 (Ontong Java; Courtillot & Renne, 2003). Duration of LIP emplacement is largely from 1 to 5 Ma but ranges to as long as 50 Ma (Ernst, 2014).

The relatively primitive compositions of many LIPs, including some continental flood basalt (CFB) lavas (Coffin & Eldholm, 1994), allow for interpretation of mantle source character using isotopic compositions. CFB are more prone to compositional deviation from their original mantle parentage due to storage, differentiation, and potential contamination within the crust, compared to their oceanic counterparts. CFB provinces include high-Mg primitive lavas but also contain basaltic compositions consistent with crustal differentiation from high-Mg melts (e.g., Cox, 1980; Garfunkel, 2008; Thompson et al., 1983). Another suggestion to account for CFB compositions with lower MgO (~8 wt.% MgO) and Ni (<200 ppm) is that CFB are derived from melts of metasomatized mantle sources (e.g., Hawkesworth et al., 1999; Turner et al., 1996) or of eclogite (e.g., Camp & Hanan, 2008; Luttinen et al., 2010; Takahahshi et al., 1998).

Isotopic characteristics are critical for evaluating contributions from crustal versus mantle sources (cf. Camp & Hanan, 2008; Carlson, 1984; Heinonen et al., 2016; Melluso et al., 2006; Wolff et al., 2008; Wolff & Ramos, 2013). Our aim is to assess the mantle sources and the effects of crustal passage for the Steens Basalt, which is among the earliest and most mafic members of the CRBG, which in turn, is the youngest and overall least primitive CFB worldwide (Figure 1; Moore et al., 2018, and references therein). The main eruptive center of the Steens Basalt is preserved in a 1 km high fault scarp that exposes most of the eruptive history (Camp et al., 2013). Detailed stratigraphic control of geochemical analyses throughout the Steens Basalt section (Moore et al., 2018) gives important constraints on changes in mantle and crustal input and the staging of magmas during the onset of CFB magmatism.

There is broad agreement that the radiogenic isotope composition of lavas of the CRBG have at least two mantle contributions: a depleted mantle end-member (e.g., C1; Figure 2), reflecting upwelling of depleted mantle owing to extension, and a more incompatible trace element enriched component (e.g., C2 and IC; Figure 2) that has a plume source or old lithospheric mantle contribution. The more mafic members of the CRBG (Steens, Imnaha, and Picture Gorge Basalts) fall broadly on an array between such components (Figure 2; Carlson, 1984; Hooper & Hawkesworth, 1993; Camp & Hanan, 2008; Wolff et al., 2008; Wolff & Ramos, 2013). Additional components are required to account for differences and scatter in and among members. Wolff et al. (2008) and Wolff and Ramos (2013) suggest that the Steens and Picture Gorge Basalts are contaminated by either arc derived fluids (Picture Gorge; see also Cahoon et al., 2020; Brandon et al., 1993) and/or mafic accreted terranes (Steens). The later and more voluminous Grande Ronde lavas were extensively contaminated by cratonic crust (ibid.). In contrast, Camp and Hanan (2008) suggest that delamination and melting of deep eclogitic crustal roots accounts for crust-like isotopic signatures in the main CRBG pulse.

We present new Sr, Nd, and Pb isotopic data (Figure 2) and first report of Hf, Os, and $\delta^{18}O$ isotopic data from a comprehensive stratigraphic section of samples of the Steens Basalt. We couple the isotope data with major and trace element geochemical interpretation of the three-phase evolution of the Steens Basalt (Moore et al., 2018). Our focus is on temporal changes in mantle source character and the effects on magma composition by passage through the deep and shallow crust at the onset of CRBG magmatism rooted in the context of the detailed stratigraphically constrained compositional and petrologic constraints.

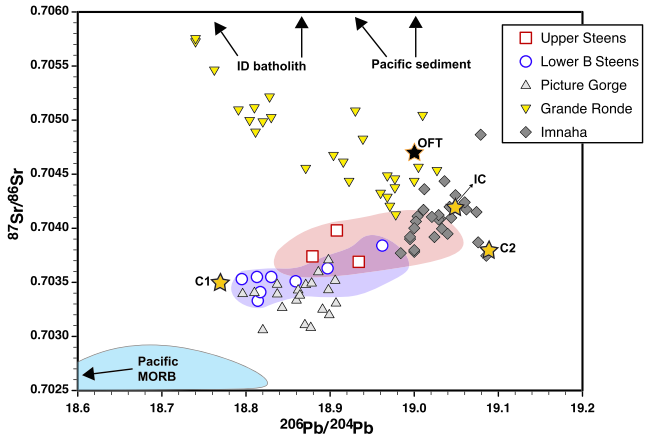

Figure 2. $^{87}Sr/^{86}Sr$ versus $^{206}Pb/^{204}Pb$ diagram for the main eruptive stages of the Columbia River Basalt Group, with emphasis on the expanded range of Steens basalt compositions from this study. Imnaha, Grande Ronde, and Picture Gorge data from: Carlson et al. (1981); Carlson (1984); Hooper and Hawkesworth (1993); Brandon et al. (1993); Camp and Hanan (2008). Lower B (open blue circles) and upper (open red squares) from Wolff et al. (2008). Blue and red fields encompass the full range of lower B and upper Steens Basalt data presented in this study, and lower A Steens Basalt samples fall in the region where the blue and red fields overlap (see Figure 12 for detail). C1 and C2 are mantle end-member components of Carlson (1984). IC is the Imnaha component defined by Wolff and Ramos (2013), which is similar to C2 and is interpreted by many to be a plume component (e.g., Brandon & Goles, 1988; Hooper et al., 2007; Wolff & Ramos, 2013). The star labeled OFT is a representative the Olds Ferry Terrane composition (Table 3). Black arrows show the direction toward Idaho Batholith (Gaschnig et al., 2011) and Pacific sediment compositions, after Wolff & Ramos, 2013. The Pacific mid-ocean ridge basalt (MORB) field (Stracke et al., 2003) extends to lower $^{87}Sr/^{86}Sr$ and $^{206}Pb/^{204}Pb$ beyond the scale of this diagram.

2. Geologic Setting and Petrologic Context

The Steens Basalt flows cover an area of 53,000 km^2 and have a total estimated volume of 31,800 km^3 or ~15% of the 210,000 km^3 estimated volume of the entire CRBG (Camp et al., 2013; Reidel et al., 2013; Figure 1). The Steens Basalt erupted as early as 17.0 Ma ago (Moore et al., 2018) and together with the Picture Gorge Basalt of north-central Oregon (17.2–16.1 Ma; Cahoon et al., 2020) represents the onset of Columbia River Flood Basalt volcanism, 95% of which erupted between 16.7 and 15.9 Ma (Kasbohm and Schoene, 2018). At Steens Mountain, locus of many Steens dikes, the stack of sequential Steens Basalt flows is the thickest and the compositional range is the widest (Figures 1 and 3; Johnson et al., 1998; Brueseke et al., 2007; Bondre & Hart, 2008; Camp et al., 2013; Moore et al., 2018). A kernel density function analysis of 49 Steens ages (compilation of Camp et al., 2013; Moore et al., 2018) suggests greatest activity (most ages) between 16.8 and 16.4 Ma and lingering activity to ~16 Ma. At Steens Mountain, the ~1 km-thick basalt section overlies Oligocene volcanic rocks. The basement of eastern Oregon consists of accreted Paleozoic to Mesozoic mafic arc terranes stitched together by Mesozoic plutons (Walker et al., 1991). Just to the northeast of Steens Mountain, the midcrustal basement rocks are part of the late Triassic to Cretaceous Olds Ferry arc terrane (Kurz et al., 2017).

The earliest flows of the Steens Basalt are of reversed polarity and transition to normal polarity around the 16.7–16.5 Ma Steens magnetic reversal (Jarboe et al., 2008, 2010; Mahood & Benson, 2017) during the upper Steens Basalt eruptions (Figure 3). Shortly after the magnetic reversal and coeval with the third, waning stage of the Steens eruptions, volcanism of the CRBG shifted north-northeast to the Columbia Plateau where flows emanated from the Chief Joseph Dike Swarm first to produce the Imnaha Basalt and then the most voluminous of the CRBG formations, the Grande Ronde flows (Figures 1 and 3). These units (Figure 3) constitute the bulk of CRBG volcanism, though eruptions continued until ~6 Ma (Reidel et al., 1989).

The type section of Steens Basalt at Steens Mountain (Camp et al., 2013) has been well sampled and studied throughout the full thickness of the section (Camp et al., 2013; Gunn & Watkins, 1970; Helmke & Haskin, 1973; Johnson et al., 1998; Moore et al., 2018). Compositional distinctions with stratigraphic order resulted in an informal designation between lower and upper Steens Basalt (Camp et al., 2003; Camp et al., 2013; Johnson et al., 1998). Moore et al. (2018) modify the stratigraphy by dividing the lower section into lower A Steens Basalt overlain by lower B Steens Basalt, which in turn is overlain by upper Steens Basalt. The Steens Basalt is known for flows with very large (1 cm to as long as 6 cm) and abundant plagioclase phenocrysts, also described in other CFB as giant plagioclase basalts (e.g., Cheng et al., 2014; Higgins & Chandrasekharam, 2007; Sheth, 2016). These flows are present in each Steens Basalt stage but vary in texture throughout the section (Moore et al., 2018). $^{87}Sr/^{86}Sr$ of plagioclase from a variety of lava textures in the Steens Basalt are generally in equilibrium with whole rock $^{87}Sr/^{86}Sr$, indicating the bulk of the crystals grew within the Steens magmatic system and are not xenocrystic (Toth, 2018). Giant plagioclase basalts also occur in the Imnaha Basalt (Hooper et al., 1984; Reidel et al., 2013) and in the Picture Gorge Basalt (Bailey, 1989) of the CRBG.

Moore et al. (2018) establish a three-stage evolution of the onset, waxing, and waning of a major pulse of basalt interacting with the crust on its way to eruption to produce the Steens Basalt. The earliest stage, the lower A Steens Basalt, has relatively low eruption rate and produces the smallest volume of lavas. The lavas are characterized by initially heterogeneous compositions, ranging from tholeiitic to slightly alkaline basalts, that are derived from variable recharge proportions and crystal fractionation (Figure 3). The second stage, represented by lower B Steens Basalt, has the highest eruption rate and volume. This waxing stage

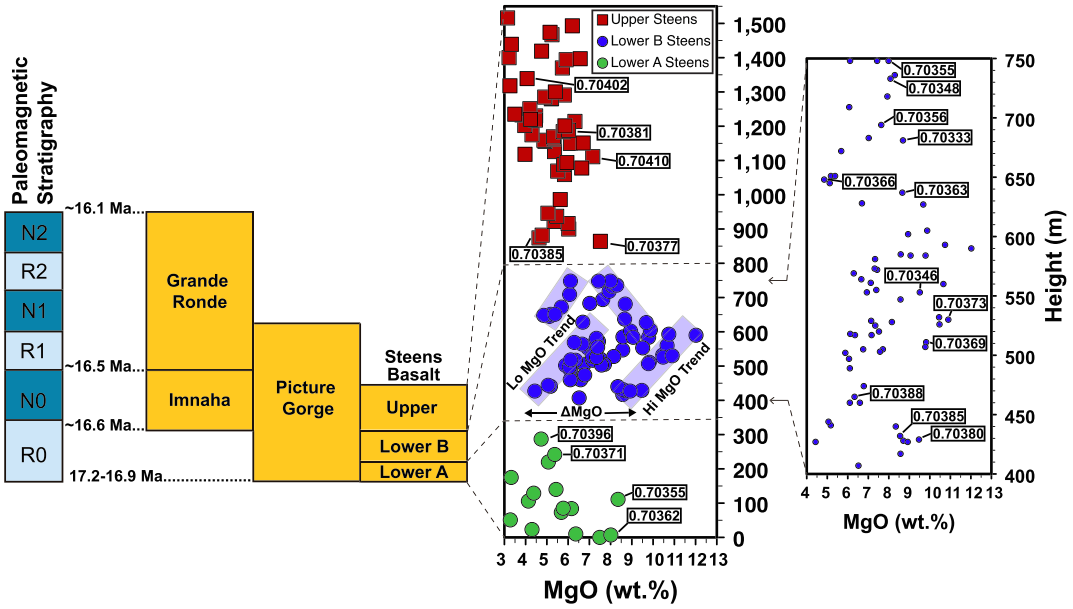

Figure 3. Schematic regional stratigraphy for the informally designated main stage eruptions of the CRBG and MgO compositional variation with stratigraphy (height in meters) for the three stages of the Steens Basalt. The Steens reversal (R0 to N0) is estimated at 16.6 Ma (Baksi, 2010; Jarboe et al., 2008), at 16.7 (Jarboe et al., 2010), and is revised to 16.5 Ma (Mahood & Benson, 2017). Range of Picture Gorge Basalt from Cahoon et al. (2020); we note that there is not yet paleomagnetic cross correlation on these new ages. Blue transparent bars highlight the high and low MgO trends in the lower B Steens stage, and emphasize the early increasing magnesian character at consistent ΔMgO. Values in black rectangles are $^{87}Sr/^{86}Sr$ for select samples to show detail of changing composition across and within the three stages. The stratigraphic section to the far-right shows detail of $^{87}Sr/^{86}Sr$ changes up section within the lower B Steens stage. Paleomagnetic stratigraphy from Jarboe et al. (2008, 2010). Age of initiation of Steens Basalt, MgO data and Steens Basalt stage designations from Moore et al. (2018). Other age estimates from Barry et al. (2013), the compilation of Camp et al. (2013), Kasbohm and Schoene (2018), and Cahoon et al. (2020). Stratigraphic section modified from Camp and Ross (2004), Camp and Hanan (2008), and Wolff and Ramos (2013).

contains the most primitive, dominantly olivine-phyric tholeiitic lavas, with compositions that are poor in incompatible trace elements. Recharge dominates over crystal fractionation early in this stage, as deduced from a general trend of increasing MgO low in the section (Figure 3). Notably, MgO increases upsection for both of two distinct MgO trends, a high and low MgO array (Figure 3), which display consistent ΔMgO of ~4–5 wt.% (the difference in MgO concentration of samples at approximately equivalent stratigraphic height; Figure 3). The low-MgO array is interpreted as the fractionated daughters (~15% fractionation) of the strongly recharging high-MgO array. Fractionation is in some cases accompanied by minor assimilation of cumulates, intercumulus melt, or more rarely wall rock, to explain variations in Fe, incompatible elements, and isotopic composition (Figure 4; Moore, 2018; see below). Similar repeated cycles of recharge and differentiation are observed for thick sections of basalt flows cored on the Snake River Plain (Potter et al., 2018; Shervais et al., 2006).

Fractional crystallization outpaces recharge late in stage B, as evident in the more evolved compositions up section (Figure 3), which signal a waning stage with less frequent eruptions, called the upper Steens Basalt. During eruption of the upper Steens stage, the magmatic system becomes more evolved, producing more alkalic compositions ranging to basaltic trachy-andesite with higher incompatible trace element abundances and more radiogenic Sr and Pb isotopic ratios (Figures 2 and 3; Wolff et al., 2008; Wolff & Ramos, 2013; Moore et al., 2018). This is a consequence of both reduced basaltic recharge relative to fractional crystallization and a contribution by crustal assimilation, which is facilitated by prolonged magmatism that has thermally primed the crust. Major element modeling of the lower B and upper Steens Basalt stages using the Magma Chamber Simulator (MCS; Bohrson et al., 2014) indicate that recharge masses in the lower B Steens are nearly double those of the upper Steens, but conversely that fractional crystallization masses are nearly double in the upper Steens compared to the lower B stage (Bendaña et al., 2017; Graubard, 2016). Assimilation of crustal melts in the lower B stage is minor but becomes significant in the

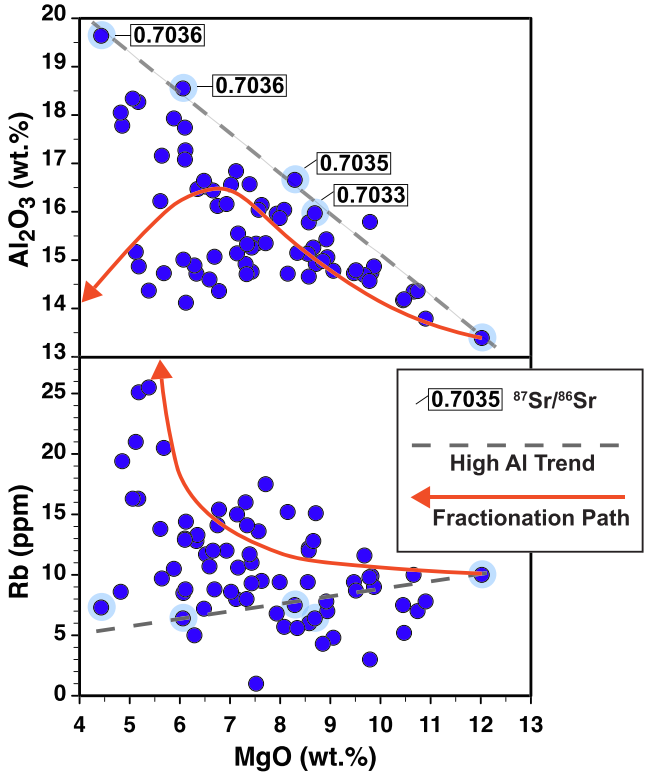

Figure 4. Al_2O_3 and Rb versus MgO for the lower B Steens Basalt. Gray dashed line shows a trend in the lower B Steens data toward high Al_2O_3 but low Rb, consistent with assimilation of plagioclase cumulates. Red lines show the fractionation trend from a basaltic parent of 12 wt.% MgO and 0.5 wt.% H_2O at 400 MPa, calculated using the MELTS program (Gualda et al., 2012); the arrow points in the direction of increasing amounts of fractionation. Samples outlined in light blue define the high Al_2O_3 trend and have $^{87}Sr/^{86}Sr$ compositions as shown in the black outlined boxes. Al_2O_3, MgO, and Rb compositions from Moore et al. (2018).

generation of the more evolved upper Steens lavas. An important outcome of initial energy balance modeling (EC-RAFC, Spera and Bohrson (2001) Bohrson and Spera (2001) and MCS) is that a single magma chamber is untenable. To repeatedly raise MgO from fractionated low-MgO compositions to nearly primitive compositions would require unreasonable volumes of magma to be accommodated in the crust. Crustal staging of the Steens Basalt must therefore occur in a tiered, multilevel magmatic system (Moore, 2018).

3. Analytical Methods

New isotopic data are presented for samples collected from several stratigraphic sections along Steens Mountain (Moore et al., 2018) and from samples collected by Johnson et al. (1998) from the type section at Steens Mountain (Camp et al., 2013). Whole rock major and trace element compositions for NMSB-series samples are reported in Moore et al. (2018) and for the JS- and MF94-series samples in Johnson et al. (1998) and Wolff et al. (2008).

3.1. Radiogenic Isotopes

Preparation and analysis of samples for Sr, Nd, Pb, Hf, and Os were performed at the Carnegie Institution for Science Earth and Planets Laboratory (EPL) and for Sr, Nd, and Pb at New Mexico State University Analytical Geochemistry Research Laboratory (NMSU). Analytical methods for NMSU are detailed in Bendaña (2016); Pb and Nd analysis was on the ThermoFinnigan Neptune Plus MC-ICP-MS, Sr by thermal ionization mass spectrometry using a VGSector54. The procedures used at EPL are most recently described in Carlson et al. (2018). For the data measured at EPL, Sr data were obtained using static multicollection with 8 s integrations with a signal size from 3 to 27 $\times 10^{-11}$ amps of ^{88}Sr. Potential Rb interference was monitored at ^{85}Rb. The $^{85}Rb/^{86}Sr$ was below 1×10^{-5} for all analyses. Mass fractionation was corrected using exponential mass dependency and $^{86}Sr/^{88}Sr = 0.1194$. The Sr standard NBS987 was measured multiple times during analytical sessions and averaged 0.710243 ± 0.000002 for $n = 10$, where uncertainty is 2σ. Uncertainties for the individual sample runs are reported in the supporting information. In all cases, the uncertainty on $^{87}Sr/^{86}Sr$ was <0.00003, with typical errors <0.000003. Nd data also were obtained by static multicollection. Each ratio reported in Table 1 is the average of 240–270 ratios obtained using 8 s integrations with a signal size from 1.1 to 2.6 $\times 10^{-11}$ amps of ^{144}Nd. Mass fractionation was corrected using exponential mass dependency and $^{146}Nd/^{144}Nd = 0.7219$. The Nd standard JNdi was measured multiple times during analytical sessions and averaged 0.5121213 ± 0.0000018 ($n = 2$), 0.5121027 ± 0.0000015 (n = 2), and 0.5121150 ± 0.0000018 ($n = 5$), with the differences in values reflecting the aging of the faraday cups between analytical sessions. The reported uncertainties are 2σ. Data for the samples are adjusted to a JNdi value of 0.512115 (Tanaka et al., 2000) based on the average value determined for JNdi during the separate analytical sessions. Uncertainties for the samples are provided in the supporting information. In all cases, the uncertainty on $^{143}Nd/^{144}Nd$ was <0.00002, with typical errors <0.000005.

Lead and Hf isotopic compositions were measured on the Nu HR multicollector ICP-MS and Nu Plasma II multicollector ICP-MS at EPL. Lead samples were introduced into the plasma in 0.5 ml 0.4 N HNO_3 using a Teflon nebulizer with a 50 ml/min uptake and a glass cyclonic spray chamber. Each ratio reported in Table 1 is the average of 41–50 ratios obtained using 10 s integrations. ^{208}Pb signals ranged from 0.1 to 5.5 $\times 10^{-11}$ amps, and Tl was added to generate a ^{205}Tl signal of ~1 $\times 10^{-11}$ amps. Mass fractionation was corrected first to $^{205}Tl/^{203}Tl = 2.3875$ and then adjusted for the difference between the NBS981 Pb standards measured every three samples and the reported value for the standard (Todt et al., 1996). Average values for NBS981 obtained during analytical sessions for $n = 13$ measurements were $^{208}Pb/^{204}Pb = 36.701 \pm 0.005$, $^{207}Pb/$

Table 1
Sr, Nd, Pb, Hf, and O Isotopic Compositions for the Steens Basalt

Sample[a]	$^{87}Sr/^{86}Sr$	$^{143}Nd/^{144}Nd$	εNd	$^{208}Pb/^{204}Pb$	$^{207}Pb/^{204}Pb$	$^{206}Pb/^{204}Pb$	$^{208}Pb/^{206}Pb$	$^{207}Pb/^{206}Pb$	$^{204}Pb/^{206}Pb$	$^{176}Hf/^{177}Hf$	εHf	^{18}O
Upper Steens												
NMSB-2[b]	0.704030	0.512892	5.0	38.62	15.62	19.02	2.0312	0.8214	0.0526	0.283080	10.4	
JS62[b]	0.704040	0.512870	4.5	38.58	15.62	19.00	2.0307	0.8219				8.5
STM20[b]	0.703758	0.512927	5.6	38.54	15.61	18.90	2.0395	0.8259	0.0529	0.283100	11.1	
STM 6	0.703758	0.512928	5.7	38.54	15.61	18.90	2.0391	0.8257	0.0529	0.283100	11.1	
JS66	0.703950	0.512870	4.5	38.55	15.61	18.95	2.0348	0.8240				
JS63	0.703890	0.512900	5.1	38.60	15.63	18.97	2.0348	0.8242				
JS60	0.704020	0.512840	3.9	38.54	15.60	18.93	2.0358	0.8241				
JS58	0.703890	0.512870	4.5	38.77	15.70	19.05	2.0353	0.8243				6.18
STM 44	0.703781	0.512914	5.4	38.60	15.63	18.94	2.0373	0.8250	0.0527	0.283090	10.8	
JS57	0.703860	0.512860	4.3	38.57	15.61	18.98	2.0324	0.8226				6.25
STM 37	0.703898	0.512853	4.2	38.50	15.60	18.88	2.0395	0.8265	0.0529	0.283050	9.3	
JS55	0.703690	0.512920	5.5	38.63	15.67	18.95	2.0387	0.8268				
STM 34	0.703693	0.512929	5.7	38.46	15.59	18.84	2.0408	0.8271	0.0530	0.283102	11.2	
STM 33	0.703714	0.512936	5.8	38.48	15.59	18.85	2.0407	0.8270	0.0530	0.283100	11.1	
JS52	0.703780	0.512900	5.1	38.45	15.59	18.87	2.0379	0.8261				
JS46	0.703840	0.512900	5.1	38.46	15.60	18.88	2.0372	0.8264				
JS45	0.703740	0.512910	5.3	38.47	15.60	18.88	2.0372	0.8259				5.91/6.02
STM 15	0.703686	0.512932	5.7	38.48	15.59	18.87	2.0391	0.8262	0.0530	0.283097	11.0	
JS44	0.704095	0.512916	5.4	38.69	15.60	19.00	2.0363	0.8212	0.0526	0.283000	7.6	6.75
JS41	0.703970	0.512890	4.9	38.51	15.93	18.43	2.0350	0.8244				6.15
JS39	0.703680	0.512910	5.3	38.51	15.61	18.91	2.0368	0.8254				6.01/6.12
JS34	0.703690	0.512900	5.1	38.54	15.60	18.97	2.0315	0.8225				6.19
JS32	0.703850	0.512870	4.5	38.53	15.60	18.98	2.0303	0.8219				
JS31	0.703770	0.512930	5.7	38.52	15.62	18.91	2.0371	0.8260				
Lower B Steens												
NMSB-23[b]	0.703531	0.512981	6.7	38.64	15.65	19.00	2.0344	0.8236	0.0506	0.283140	12.5	
NMSB-25[b]	0.704021	0.512895	5.0	38.80	15.70	19.09	2.0324	0.8227	0.0515	0.283080	10.4	
JS29	0.703600	0.512950	6.1	38.64	15.68	18.96	2.0378	0.8268				
JS26	0.703480	0.512970	6.5	38.62	15.69	18.92	2.0413	0.8291				5.96
JS23	0.703560	0.512890	4.9	38.43	15.60	18.86	2.0374	0.8269				
JS22	0.703331	0.513028	7.6	38.48	15.62	18.81	2.0451	0.8302	0.0524	0.283170	13.6	6.15
NMSB-21	0.703739	0.512925	5.6	38.61	15.61	18.93	2.0405	0.8248	0.0528	0.283090	10.8	
NMSB-20A	0.703660	0.512921	5.5	38.61	15.61	18.93	2.0404	0.8248	0.0528	0.283110	11.5	
JS19	0.703700	0.512920	5.5	38.52	15.59	18.90	2.0382	0.8250				6.10/6.24
NMSB-19	0.703463	0.512993	6.9	38.60	15.60	18.94	2.0382	0.8239	0.0525	0.283180	13.9	
MF9472	0.703640	0.512930	5.7	38.53	15.60	18.93	2.0352	0.8240				6.49
NMSB-18	0.703727	0.512943	6.0	38.58	15.60	18.91	2.0397	0.8249	0.0528	0.283100	11.1	
MF9471[b]	0.703560	0.512940	5.9	38.91	15.77	19.09	2.0377	0.8262				
MF9471[a]	0.703560	0.512950	6.1	38.55	15.63	18.92	2.0376	0.8263				
MF9469	0.703693	0.512951	6.1	38.58	15.61	18.94	2.0367	0.8241				
MF9468	0.703670	0.512930	5.7	38.62	15.61	18.99	2.0342	0.8224				
NMSB-13	0.703590	0.512916	5.4	n.a.[c]	n.a.[c]	n.a.[c]	n.a.[c]	n.a.[c]	n.a.[c]	0.283120	11.8	
MF9467	0.703880	0.512930	5.7	38.61	15.62	18.95	2.0374	0.8243				6.24
NMSB-5	0.703850	0.512916	5.4	38.64	15.63	18.95	2.0396	0.8244	0.0525	0.283080	10.4	
MF9466	0.703805	0.512910	5.3	38.92	15.75	19.11	2.0365	0.8240				6.07/6.34
NMSB-36	0.703468	0.513000	7.1	38.40	15.60	18.79	2.0436	0.8301	0.0528	0.283130	12.2	
MF9464	0.703530	0.512963	6.3	38.44	15.58	18.83	2.0412	0.8275	0.0530	0.283110	11.5	
MF9463	0.703547	0.512943	5.9	38.39	15.58	18.82	2.0400	0.8278				
Lower A Steens												
NMSB-70[b]	0.703957	0.512861	4.4	38.58	15.61	18.94	2.0362	0.8240	0.0528	0.283056	9.5	
NMSB-69	0.703708	0.512930	5.7	38.49	15.59	18.88	2.0389	0.8259	0.0530	0.283111	11.5	
NMSB-64	0.703547	0.512981	6.7	38.45	15.57	18.92	2.0326	0.8231	0.0528	0.283119	11.8	

Note. δ18O of plagioclase in per mil, two values reported where replicate analysis performed. Uncertainties are presented in the supporting information. [a]Samples with reported 176Hf/177Hf were analzyed at DTM, all others at NMSU. [b]Samples are in stratigraphic order, excepting samples with this superscript, which are dikes and thus lack stratigraphic context. [c]Signal strength of Pb was insufficient for accurate isotope ratio measurements for two aliquots of sample NMSB 13.

$^{204}Pb = 15.492 \pm 0.002$, and $^{206}Pb/^{204}Pb = 16.940 \pm 0.002$ where uncertainty is 2σ. Uncertainties for the samples are provided in the supporting information. In all cases, the uncertainty on $^{208}Pb/^{204}Pb$ was <0.07, on $^{207}Pb/^{204}Pb < 0.03$, on $^{206}Pb/^{204}Pb < 0.03$, on $^{208}Pb/^{206}Pb < 0.0002$, and on $^{207}Pb/^{206}Pb < 0.0002$.

For Hf, each ratio reported in Table 1 is the average of 52–80 ratios obtained using 10 s integrations where signal size of ^{178}Hf ranged from 0.8 to 10.9×10^{-11} amps. Mass fractionation was corrected to $^{179}Hf/^{177}Hf = 0.7325$. The average of JMC475 obtained during analytical sessions for $n = 13$ measurements were $^{176}Hf/^{177}Hf = 0.282166 \pm 0.000002$ where uncertainty is 2σ. Reported $^{176}Hf/^{177}Hf$ values (Table 1) were adjusted by the offset between the average of the JMC475 standards run in each session and the reported value of 0.282160, which overlaps within uncertainty with the value of 0.282163 reported by BlichertToft et al. (1997). Uncertainties for the samples are provided in the supporting information. In all cases, the uncertainty on $^{176}Hf/^{177}Hf$ was <0.000007.

Os isotopic determinations were made using the Thermo-Fisher Triton thermal ionization mass spectrometer at EPL by peak hopping on an electron multiplier measuring all Os isotopes and ^{185}Re for potential interference. Mass fractionation was corrected to $^{192}Os/^{188}Os = 3.08259$. The EPL Johnson-Matthey Os standard was measured multiple times during analytical sessions and averaged $^{187}Os/^{188}Os = 0.17383 \pm 0.00006$ for $n = 3$ where uncertainty is 2σ. Replicate Os isotopic analyses on two separate dissolutions of two samples indicate reproducibility in Os concentration and $^{187}Os/^{188}Os$ of 4% and 0.8%, respectively, for NMSB5 and 6% and 1.4%, respectively, for NMSB18.

To test for interlaboratory bias, sample JS44 was analyzed at both EPL and NMSU. The isotopic standards used at both labs are identical for Sr, Nd, and Pb. Reproducibility between laboratories for $^{87}Sr/^{86}Sr$, $^{143}Nd/^{144}Nd$, $^{206}Pb/^{204}Pb$, $^{207}Pb/^{204}Pb$, and $^{208}Pb/^{204}Pb$ are 0.007%, 0.002%, 0.6%, 0.4%, and 0.3%, respectively. Samples with reported values for $^{176}Hf/^{177}Hf$ in Table 1 are those analyzed at DTM, and the remainder were analyzed at NMSU.

3.2. Oxygen Isotopes

Plagioclase mineral separates were extracted from crushed samples from 15 flows. The crushed samples were sieved to a grain size >0.3 mm, magnetically separated to remove groundmass, and the freshest plagioclase was hand-picked at 20X magnification. Oxygen isotopic compositions (Table 1) were measured via an integrated CO_2 laser fluorination MAT 253 isotope ratio mass spectrometer system, using BrF_5 as reagent, at the University of Oregon (Bindeman, 2008; Loewen & Bindeman, 2015). $\delta^{18}O$ ratios are reported in per mil (‰) deviations from Vienna Standard Mean Ocean Water in the delta (δ) notation. The range of material analyzed from each sample was 1.2 to 1.5 mg. The in-house Gore Mountain Garnet standard (UOG, accepted $\delta^{18}O = 6.52‰$) was measured five times during the analytical session to correct data to the international Vienna Standard Mean Ocean Water scale (Loewen & Bindeman, 2015). Analytical precision of UOG analyses from the session was 0.08% (2σ). Some slight variability between replicate analyses from separate aliquots of four samples is likely due to within sample variability in plagioclase.

3.3. Helium Isotopes

Helium isotope analyses on olivine separates from two samples were performed using a Nu Instruments noble gas mass spectrometer at Oregon State University, following procedures described in Graham et al. (2014). Helium concentrations were determined by peak height comparison to standards of known size. Over the course of this study the ^4He blank level was 2.2×10^{-11} std cm^3. Blank-corrected ^4He concentrations in the samples (NMSB19 olivine, 243 mg, and NMSB49 olivine, 101 mg) were 0.72 and 0.86×10^{-9} std cm^3/g, respectively. Both analyses were below the ^3He detection limit of 2.5×10^{-16} std cm^3 (6,700 atoms), which is estimated from the ^3He blank variability (defined as 3 standard deviations about the mean). The maximum $^3He/^4He$ ratio in the samples is therefore 0.25 R_A ($[2.5 \times 10^{-16}/0.72 \times 10^{-9}]/1.4 \times 10^{-6}$), indicating that at such low helium concentration levels, radiogenic crustal helium is dominant.

4. Results

4.1. Sr, Nd, Pb, and Hf Isotopic Compositions

Steens Basalt samples generally plot as an array between mid-ocean ridge basalt (MORB)-like (global/Pacific MORB fields) and more incompatible element enriched OIB-like compositions in most isotopic spaces

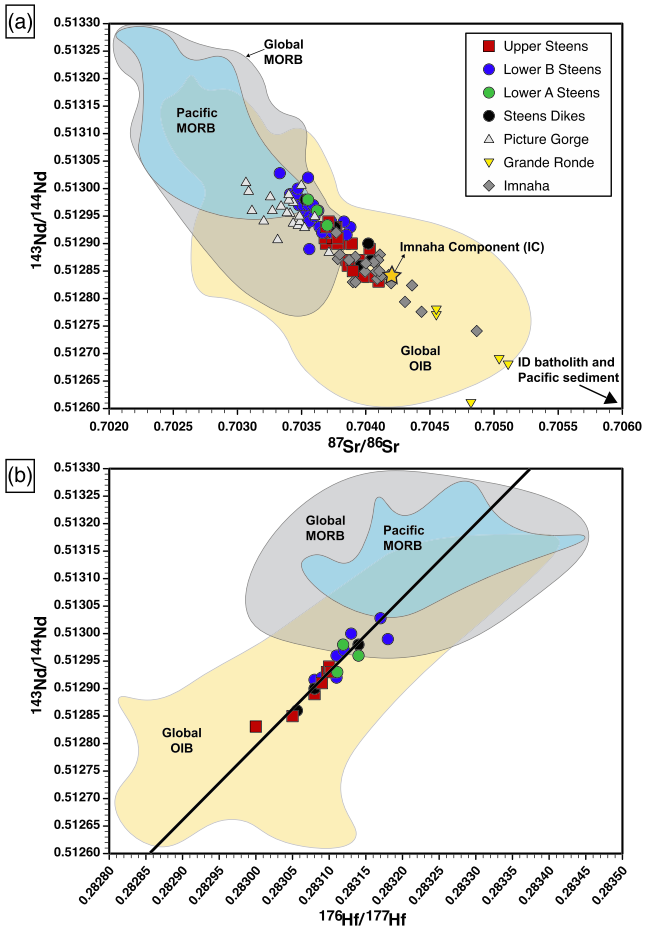

Figure 5. $^{143}Nd/^{144}Nd$ versus (a) $^{87}Sr/^{86}Sr$ and (b) $^{176}Hf/^{177}Hf$ for the Steens Basalt and other main stage formations of the CRBG. Some Steens Basalt data and all other CRBG data from Hooper and Hawkesworth (1993), Camp and Hanan (2008), and Wolff et al. (2008). Global OIB, global MORB, and Pacific MORB fields from Stracke et al. (2003). IC is the Imnaha component defined by Wolff and Ramos (2013). Black arrow shows the direction toward Idaho Batholith (Gaschnig et al., 2011) and Pacific sediment compositions (after Wolff & Ramos, 2013). Mantle array in (b) from Graham et al. (2006).

(Figures 2 and 5). All samples fall within the mantle array field (Hart et al., 1986) in $^{143}Nd/^{144}Nd$ versus $^{87}Sr/^{86}Sr$ (not shown; Figure 5a) and near the mantle array line (Graham et al., 2006) in $^{143}Nd/^{144}Nd$ versus $^{176}Hf/^{177}Hf$ (Figure 5b). At a given $^{206}Pb/^{204}Pb$, the lower Steens Basalt samples tend to have lower $^{87}Sr/^{86}Sr$ (Figure 2) and higher $^{143}Nd/^{144}Nd$ and $^{176}Hf/^{177}Hf$ than the upper Steens. In general, samples from the lower B Steens Basalt fall closer to the MORB fields, whereas most upper Steens Basalt lavas plot within the OIB fields. The lower A Steens Basalt compositions fall near the overlap of samples from the other two stages but are more similar to lower B stage lavas on the whole (Figure 5). In comparison to the other formations of the CRBG, lower B Steens Basalt overlaps with some Picture Gorge Basalt compositions, though the Picture Gorge Basalt has more MORB-like character overall (Figures 2 and 5). The upper Steens Basalt overlaps in $^{87}Sr/^{86}Sr$ with Imnaha Basalt compositions but does not range as high in values of $^{87}Sr/^{86}Sr$ and $^{206}Pb/^{204}Pb$ (Figures 2 and 5). These results are consistent with previous isotopic data reported for the Steens Basalt (Camp & Hanan, 2008; Carlson & Hart, 1987; Wolff et al., 2008), but the new data exhibit an expanded range of compositions (Figures 2 and 5).

4.2. Os Isotopic Compositions and Concentrations

$^{187}Os/^{188}Os$ for lower B Steens Basalt samples are remarkably homogenous (Figure 6). Though the lavas span MgO compositions from ~6–11 wt.%, $^{187}Os/^{188}Os$ only ranges from 0.1292 to 0.1311 and $^{187}Os/^{188}Os_i$ from 0.1282 to 0.1296 (Figures 6 and 7 and Table 2). This limited range of $^{187}Os/^{188}Os$ falls within the range of global MORB and at the low end of reported compositions for global OIB (Figure 6) and, therefore, does not distinguish lower B Steens Basalt as having more MORB or OIB-like character. Although $^{187}Os/^{188}Os$ is restricted in this stage of the Steens Basalt, the samples span the full range of $^{87}Sr/^{86}Sr$ for all lower B Steens Basalt (Figures 5 and 7). The lower B Steens Basalt plots within or near the field of Pacific MORB in both $^{187}Os/^{188}Os$ versus $^{87}Sr/^{86}Sr$ and $^{187}Os/^{188}Os$ versus $^{206}Pb/^{204}Pb$ (Figure 7). A decrease in $^{87}Sr/^{86}Sr$ and $^{206}Pb/^{204}Pb$ is roughly correlated with an increase in stratigraphic height within this stage of the Steens Basalt (Figures 3 and 7). Os concentrations are unusually high in the lower B Steens Basalt (~0.3–0.9 ppb) relative to the bulk of MORB and OIB (Figure 6a) and are high for given MgO relative to basaltic rocks from diverse tectonic environments worldwide (Figure 6b).

$^{187}Os/^{188}Os$ from the upper Steens Basalt is much more radiogenic (0.2824) than in the lower B Steens Basalt stage; Os concentration is also very low (0.0015 ppb). The upper Steens Basalt flow analyzed for Re-Os is located approximately 250 m into the upper Steens Basalt section at Steens Mountain, where the total thickness of that stage is ~650 m. The MgO content of the sample is ~7 wt.%, comparable to the lower end of MgO among samples analyzed for Re-Os from the lower B Steens Basalt (Figure 6) but among the most mafic in the upper Steens Basalt (Figure 3). Even so, the upper Steens Basalt is significantly higher in $^{187}Os/^{188}Os$, as well as $^{87}Sr/^{86}Sr$ and $^{206}Pb/^{204}Pb$ than the lower B Steens Basalt (Figures 2, 5, and 7). $^{187}Os/^{188}Os$ and Os concentrations in upper Steens Basalt are similar to those in the Grande Ronde Basalt, though slightly less radiogenic (Figure 6).

Osmium generally behaves compatibly in the Steens Basalt; Os decreases with decreasing MgO, Ni and Cr (Figures 6b and 8) and the Steens Basalt is at the high end of the array for CRBG (Figure 6b). Osmium variation with FeO and Cu is more scattered. Within the lower B Steens, FeO decreases with decreasing Os, but other samples of the CRBG are displaced to higher FeO for given Os. Osmium and Cu concentrations in the

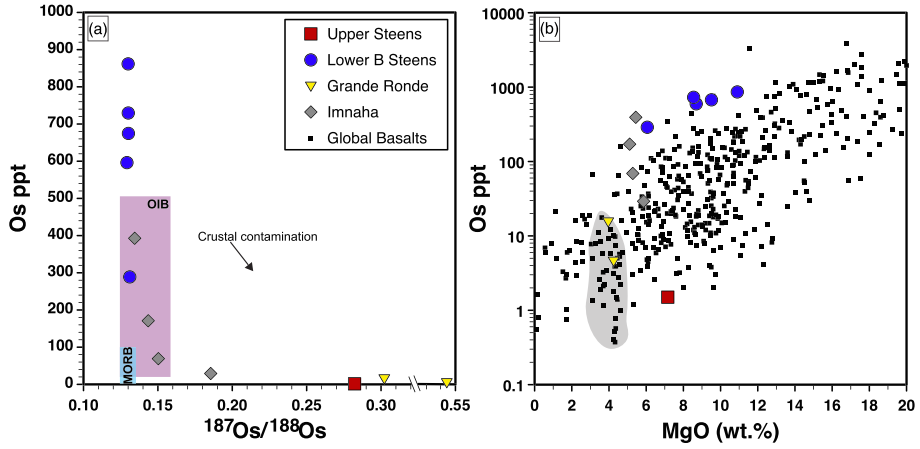

Figure 6. (a) Os concentration versus $^{187}Os/^{188}Os$. MORB and OIB fields represent the bulk of uncontaminated global basalts from Shirey and Walker (1998) and Hauri (2002). Black arrow points in the direction that simple crustal contamination can drive Os isotopic composition and concentrations. Note the scale break at high values of $^{187}Os/^{188}Os$. (b) Os concentration versus MgO for the Steens, Imnaha, Grande Ronde, and Wanapum members of the Columbia River Basalt Group relative to global mafic magmas. Imnaha and Grande Ronde Basalt data from Chesley and Ruiz (1998), with MgO from Hooper and Hawkesworth (1993). Light gray field encompasses the data from one Wanapum Basalt flow (Vye-Brown et al., 2013). Note the switch to log scale in this panel. Citations for global basalt Os data compiled from GeoRoc and additional references listed in supporting information.

lower B Steens Basalt range to higher values than are found in either the Imnaha or Grande Ronde Basalt, but most samples among these three CRBG stages have similar FeO* content overall (Figure 8).

4.3. Oxygen Isotopic Compositions

$\delta^{18}O$ of plagioclase from Steens Basalt lavas ranges from 5.9‰ to 6.6‰ (Figures 9 and 10 and Table 1), a range similar to the Imnaha and Picture Gorge Basalts. A value of 7.4‰ in the stratigraphically highest sample of the lower B Steens Basalt, and 8.5‰ from an upper Steens Basalt dike (Figure 9) are more akin to the less mafic members of the CRBG (the Grande Ronde, Wanapum and Saddle Mountain Basalts), which range from 5.9‰ to 8.3‰ (Figure 10). Plagioclase phenocryst cores have a relatively narrow range of An_{78}-An_{58} (Moore et al., 2018), and thus, $\Delta^{18}O$ plagioclase-melt fractionation for Steens SiO_2 contents can be estimated from −0.17‰ to +0.19‰ (Bindeman, 2008), with the bulk of the data representing a fractionation factor of ~0.1‰. Given this small fractionation factor, plagioclase serves as proxy for melt $\delta^{18}O$ values and be

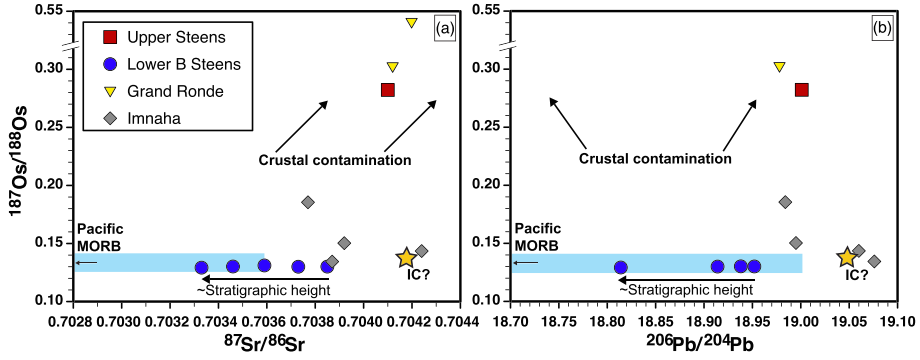

Figure 7. $^{187}Os/^{188}Os$ versus (a) $^{87}Sr/^{86}Sr$ and (b) $^{206}Pb/^{204}Pb$ for the Steens, Imnaha, and Grande Ronde Basalts. Decreasing $^{87}Sr/^{86}Sr$ and $^{206}Pb/^{204}Pb$ at approximately constant $^{187}Os/^{188}Os$ roughly correlates with increasing stratigraphic height in the lower B Steens samples. IC is the Imnaha component defined by Wolff and Ramos (2013), which was not defined in terms of $^{187}Os/^{188}Os$ and is approximated here. Double black arrows point in the directions that crustal contamination can drive Os isotope compositions. Imnaha and Grande Ronde Basalt data from Hooper and Hawkesworth (1993) and Chesley and Ruiz (1998). Pacific MORB field from Gannoun et al. (2007). Note the scale break at high values of $^{187}Os/^{188}Os$.

Table 2
Re-Os Isotopic Compositions for the Steens Basalt

Sample	MgO wt.%	Re (ppb)	Os (ppb)	$^{187}Re/^{188}Os$	$^{187}Os/^{188}Os$	2σ error	$^{187}Os/^{188}Osi$
			Lower B Steens				
JS22	8.69	0.4469	0.5962	3.61	0.12921	0.00007	0.12820
NMSB-5	8.53	0.2829	0.7296	1.86	0.13011	0.00006	0.12878
NMSB-13	6.03	0.4868	0.2889	8.12	0.13113	0.00005	0.12887
NMSB-18	10.62	0.3798	0.8617	2.12	0.13002	0.00006	0.12943
NMSB-19	9.42	0.3041	0.6747	2.17	0.13018	0.00005	0.12958
			Upper Steens				
JS44	7.16	0.3438	0.0015	1126	0.28215	0.00046	

Note. The Re-Os model age for sample JS44 is 8.1 Ma, reflecting post eruption mobility of Re or Os in this sample. MgO compositions from Moore et al. 2018.

compared to previous $\delta^{18}O$ whole rock measurements. Overall, the CRBG has elevated $\delta^{18}O$ compared to the 5.5‰–5.9‰ range of most mantle-derived basaltic magmas (Bindeman, 2008). Compositions in upper Steens Basalt are barely higher on average than lower B Steens Basalt but include the highest values; upper Steens lavas have a mean of 6.4‰ (mode = 6.2‰), compared to a mean of 6.3‰ (mode = 6.1‰) for lower B Steens lavas. An initial increase in $\delta^{18}O$ with stratigraphic height occurs in lower B Steens Basalt samples, followed by a decrease upsection, until reaching the highest outlier value high in that stage (Table 1). There is no systematic change in $\delta^{18}O$ upsection within the upper Steens Basalt (Table 1). There are two trends in $\delta^{18}O$ versus MgO and SiO_2 (Figure 9). Most of the data define slightly increasing $\delta^{18}O$ (5.9 to 6.3‰) over 48–53 wt.% SiO_2 and a decrease in MgO from 9.5 to 4 wt.%. A second trend has markedly higher $\delta^{18}O$ (5.9‰ to 8.5‰) over the same SiO_2 range. The range of $\delta^{18}O$ in the Steens Basalt is comparable to other members of the CRBG, though values do not range as low as those for the Picture Gorge and Imnaha Basalts (Figure 10).

5. Discussion

We evaluate the effects of mantle source variation and contributions by crustal processes to the generation of the Steens magmas over time, in light of the most comprehensive isotopic data set for the Steens Basalt to

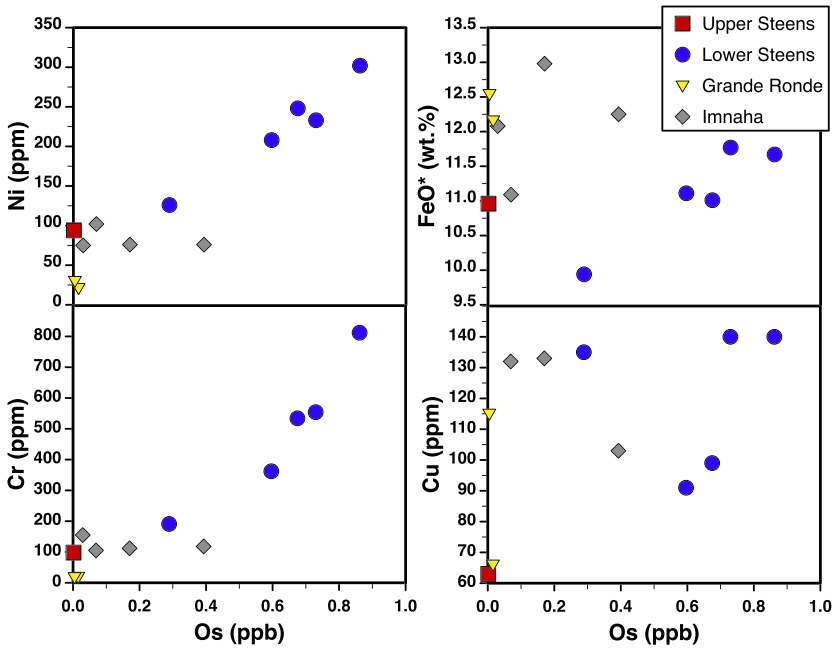

Figure 8. Select major and trace elements versus Os concentration for the Steens, Imnaha, and Grande Ronde Basalts. Imnaha and Grande Ronde Basalt data from Hooper and Hawkesworth (1993) and Chesley and Ruiz (1998).

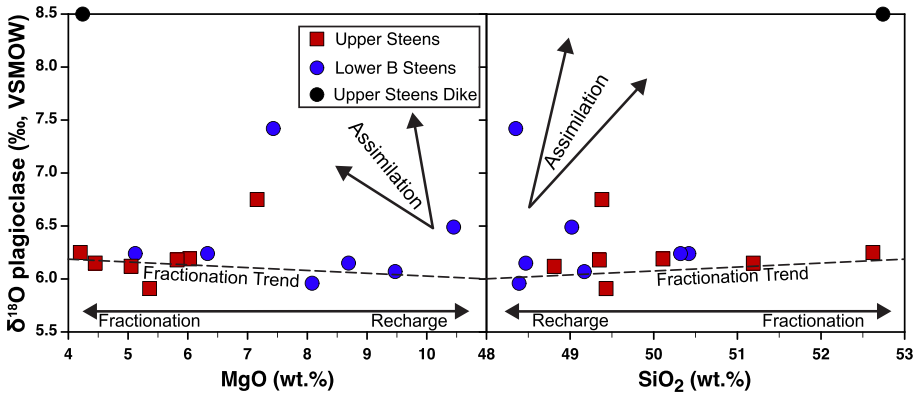

Figure 9. $\delta^{18}O$ of plagioclase versus MgO and SiO_2 for the Steens Basalt. Dashed black lines are fractionation trends from a parent of 11 wt. % MgO, 48 wt.% SiO_2, and 6‰ $\delta^{18}O$, calculated as described in the text. Double black arrows indicate the directions crustal contamination can drive compositions. Double headed black arrow shows the directions that recharge or fractionation can drive compositions.

date and in conjunction with whole rock compositional data. The expanded Steens Basalt isotopic data are consistent with the interpretation by previous CRB workers that two mantle sources contribute to generation of the Steens lavas, a depleted and an enriched source, DS and ES, respectively. We then consider two main ways by which processes modify Steens Basalt compositions during ascent through the crust: by assimilation of accreted terranes in the regional crust and by assimilation of components derived from the crystalline residues of protracted Steens magmatism.

5.1. Mantle Contributions: Sources, Amounts, and Change in Time

5.1.1. Mantle Sources and Proportions

To characterize mantle components that contribute to the generation of the Steens Basalt, we cast the isotope data relative to distinct mantle end-members originally defined by Zindler and Hart et al. (1986) (Figure 11). An additional enriched mantle component, ES (as defined by Rooney et al. (2012) based on the "C" mantle component of Hanan & Graham, 1996) is similar to the Imnaha component (IC; Wolff & Ramos, 2013) and the C2 component of Carlson (1984). The Steens isotope data make an array that lies between ES and a depleted component DS, with isotopic characteristics approaching those of the source of MORB offshore of the Pacific Northwest, in accord with previous workers (Camp & Hanan, 2008; Carlson, 1984; Hooper & Hawkesworth, 1993; Wolff et al., 2008; Wolff & Ramos, 2013). The larger extent of Steens isotopic data requires displacement of the DS component toward MORB-like compositions relative to the depleted component C1 of Carlson (1984). Carlson (1984) and Wolff and Ramos (2013) point out that the DS component is a point on a mixing line rather than a discrete component. The DS component is similar to the source involved in a younger regional basalt province, the high-alumina olivine tholeiites of the Oregon Plateau; eastward enrichment in Pb-, Sr-, and Os-isotope signatures are interpreted to result from a small contribution of variable age lithosphere from accreted terranes in the west across the cratonic boundary to the east (Bailey & Conrey, 1992; Brandon et al., 1993; Brandon & Goles, 1995; Hart et al., 1997). There is no evidence for direct mixing from either EMI or HIMU in the Steens Basalt; none of the samples plot near or toward these end-members in any isotopic space (Figure 11). Contributions from an EMII component are unlikely as well. While the Steens Basalt samples, particularly those from the upper Steens Basalt, trend toward EMII for some isotopic combinations (Figures 11a and 11b), this is not the case in all isotopic spaces (Figures 11d–11g).

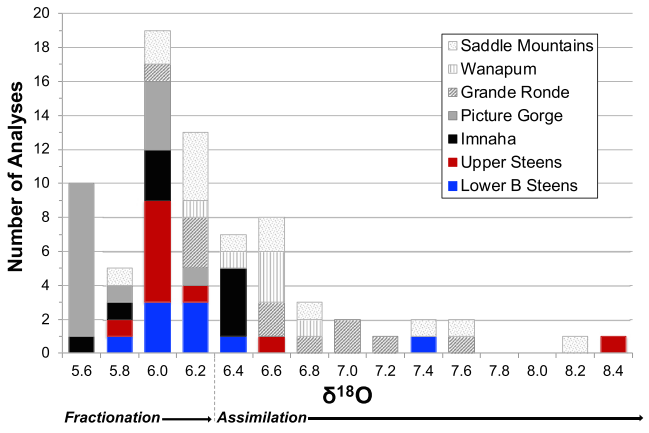

Figure 10. Histogram of $\delta^{18}O$ for formations of the CRBG. The Steens Basalt $\delta^{18}O$ analyses are from plagioclase, some Picture Gorge and Imnaha are from plagioclase (Colón et al., 2015) and all other CRBG $\delta^{18}O$ are from whole rock analysis. See text for discussion of fractionation versus assimilation compositions. CRBG whole rock $\delta^{18}O$ data from Nelson (1983), Carlson (1984), Hooper and Swanson (1990), and Brandon et al. (1993).

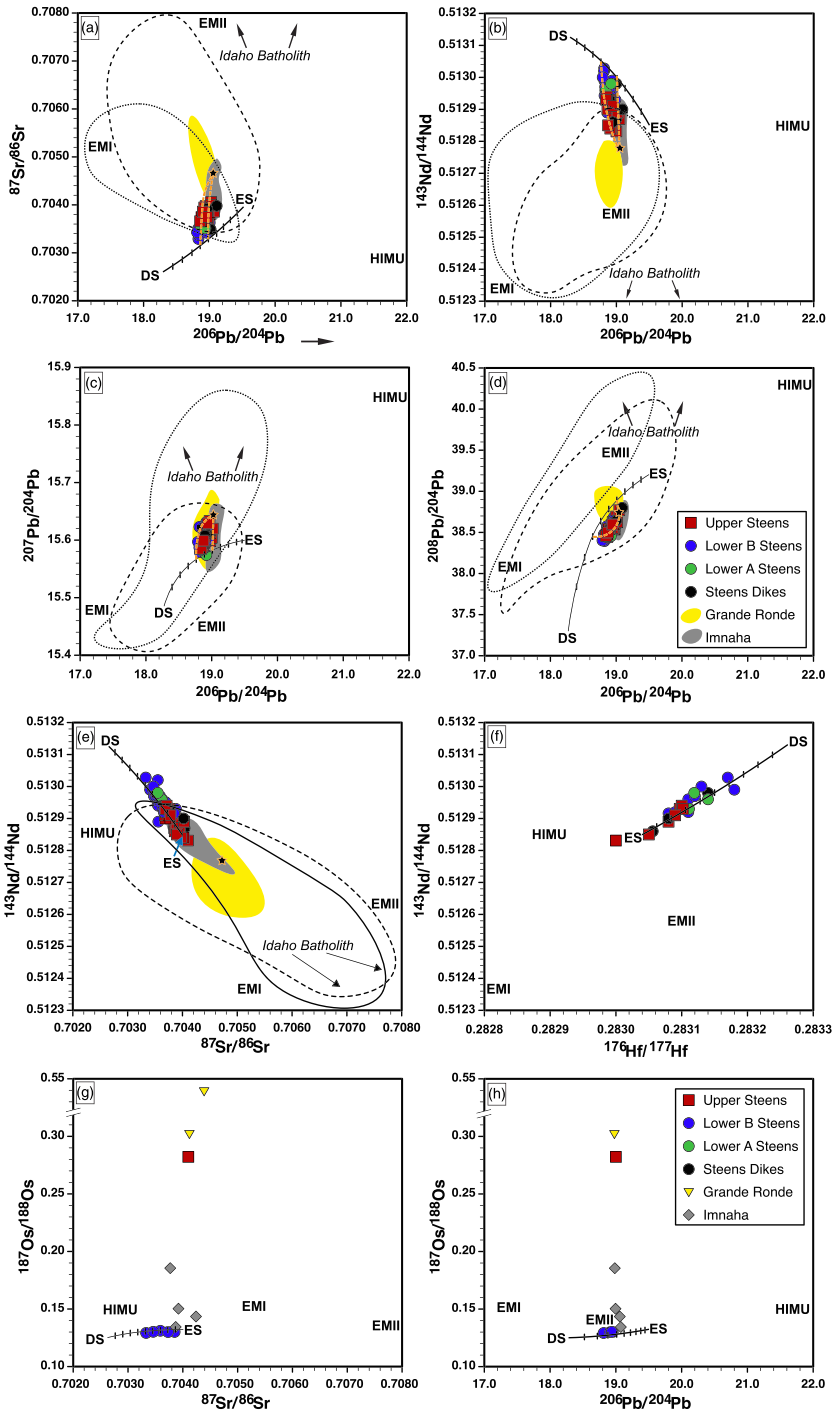

Figure 11. Mantle melt isotopic mixing models for the Steens Basalt. DS (depleted mantle), EMI (enriched mantle I), EMII (enriched mantle II), and HIMU (high μ) are the mantle components of Zindler and Hart (1986), revised by Hart et al. (1992), Hauri et al. (1994), and Stracke et al. (2005). ES = enriched source based on the "C" component of Hanan and Graham (1996) as modified by Rooney et al. (2012). Isotopic mixing curves between 5% partial melts of both depleted (DS) and enriched sources (ES) are shown with tick marks at 10% mixing increments, calculated as described in text. Gray and yellow fields encompass the data from Imnaha and Grande Ronde Basalts, respectively. Black dashed and dotted fields encompass data from the Siberian and Deccan Traps, respectively (from GeoRoc precompiled data files, accessed June, 2016). Black and orange star represents two Olds Ferry Terrane samples (Kurz et al., 2017) as a reasonable crustal contaminant. There is no reported $^{176}Hf/^{177}Hf$ or $^{187}Os/^{188}Os$ for the Olds Ferry Terrane. Black arrows show the direction toward Idaho Batholith compositions (Gaschnig et al., 2011). Note the break in scale at high $^{187}Os/^{188}Os$ in panels (G) and (H). Uncertainties (supporting information) are much smaller than symbol size for all Steens Basalt data. See Figure 12 for zoomed in detail of Steens Basalt data and modeled mixes.

Table 3
Input for Isotope Mixing Models

	ES	DS	Olds Ferry Terrane	ES 5% partial melt	DS 5% partial melt	OFT 5% partial melt
87Sr/86Sr	0.7040	0.7026	0.7047	0.7040	0.7026	0.7047
143Nd/144Nd	0.51285	0.51313	0.51277	0.51285	0.51313	0.51277
206Pb/204Pb	19.50	18.28	19.04	19.50	18.28	19.04
207Pb/204Pb	15.60	15.49	15.64	15.60	15.49	15.64
208Pb/204Pb	39.20	37.30	38.77	39.20	37.30	38.77
176Hf/177Hf	0.28304	0.28326		0.28304	0.28326	
187Os/188Os	0.1325	0.1250		0.1325	0.1250	
Sr (ppm)	21.1	7.6	1025	420	190	695
Nd (ppm)	1.4	0.6	11.5	23	10	77
Pb (ppm)	0.07	0.02	16.77	12	0.4	70
Hf (ppm)	0.31	0.16		2.90	1.50	
Os (ppm)	0.00040	0.00005		0.00004	0.000005	
Ba (ppm)	6	0.6	436	114	11.4	1860
DSr				0	0	1.5
DNd				0.01	0.01	0.1
DPb				0	0	0.2
DHf				0.06	0.06	
DOs				12	12	
DBa				0.01	0.01	0.

Note. ES = enriched source; DS = depleted source; OFT = Olds Ferry Terrane. Olds Ferry composition is sample DC08-01 of Kurz et al. (2017). Elemental concentrations for ES and DS from Sun and McDonough (1989), Shirey and Walker (1998), and Workman and Hart (2005). Other data sources as listed in Figure 11 caption. The 5% partial melts of each source calculated from batch melting equation. See text for discussion.

We compare the Steens Basalt isotope data from the most primitive samples (in lower B Steens) to a mixing array between 5% partial batch melts from each ES and DS. We use the formulation for mixing of two components, 1 and 2, with different isotopic ratios and different concentrations of elements a and b, using the equations:

$$R^a_{mix} = R^a_1 X^a_1 + R^a_2 \left(1 - X^a_1\right)$$

and

$$R^b_{mix} = R^b_1 \left[\frac{X^a_1}{r\left(1 - X^a_1\right) + X^a_1}\right] + R^b_2 \left[\frac{r\left(1 - X^a_1\right)}{r\left(1 - X^a_1\right) + X^a_1}\right]$$

and

$$r = \frac{\left(C^b / C^a\right)_2}{\left(C^b / C^a\right)_1}$$

where R_i is the isotopic ratio of component i, X_i is the elemental fraction contributed to the mixture from component i, and C is the concentration of element a or b in component i (DePaolo, 1981; as derived in Graham et al., 1992). Isotopic and elemental compositions used for the mixing end-member components (DS, ES, and OFT—Olds Ferry Terrane basement) are in Table 3. We choose mixing of melts as more likely than mixing of mantle at these time scales (≤300 ka duration of volcanism; Jarboe et al., 2010). Varying the degree of melt above 5% produces compositions that are not reflective of the primitive Steens Basalt compositional range. We choose the OFT as a source for crustal contamination because it is the closest of the accreted basement terranes of northeastern Oregon and adjacent Idaho that lies just west of the craton margin (0.706 line) for which there is a full suite of Sr, Nd, and Pb isotopic data (Table 3).

The most primitive Steens Basalt compositions can be accounted for by a range of mixing proportions from 40DS:60ES to 70DS:30ES (see mixing lines in Figures 11 and 12). Lower A and B Steens Basalt have subequal contributions of DS and ES for the bulk of the data. Note that the DS and ES components are not

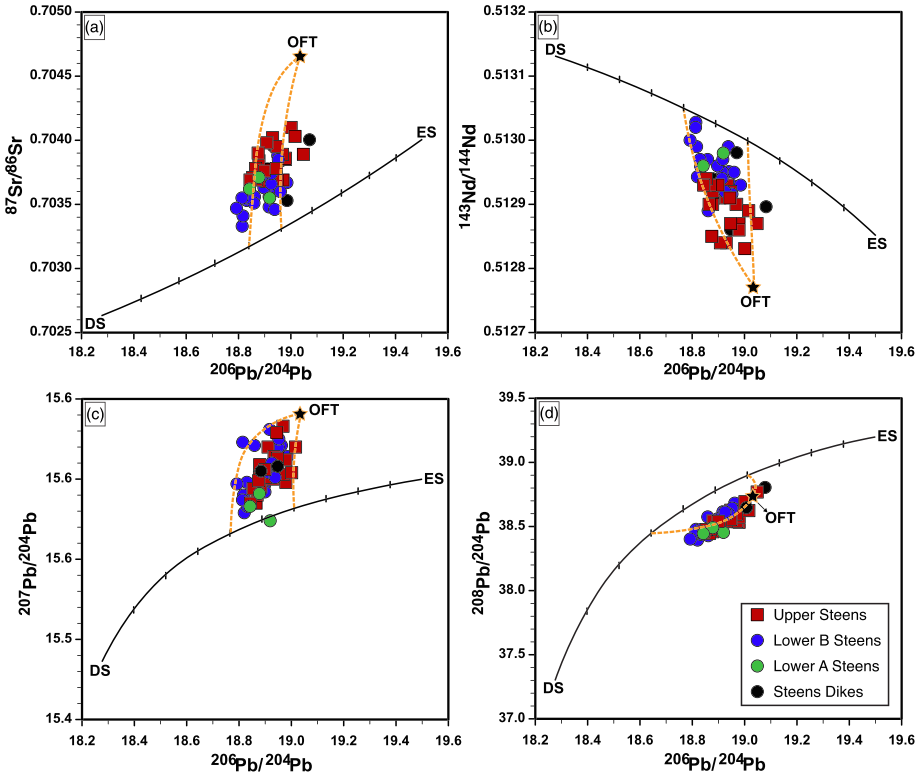

Figure 12. Crustal melt isotopic mixing models for the Steens Basalt. Orange dashed lines are calculated mixing curves between 5% partial melt of Olds Ferry Terrane (OFT, black star; Kurz et al., 2017; Table 3) and various proportions of DS-ES (abbreviated as in Figure 11) partial melt mixes. Isotopic mixing curves between DS and ES from Figure 11 are replicated, and each tick mark represents 10% increments. See text for discussion.

distinguishable in $^{187}Os/^{188}Os$ (Figures 6 and 7). Although upper Steens Basalt isotopic compositions appear to approach 100% ES, we attribute much of the spread to crustal contamination (see section 5.2). A temporal analysis of changing mantle influences follows.

5.1.2. Early Mantle Components—Lower a Steens Basalt

Lower A Steens Basalt isotopic compositions have a subequal contribution from DS and ES and cluster within the range of lower B Steens Basalt in Sr, Nd, Pb, and Hf isotopic spaces (Figures 5, 11, and 12). The lower A Steens Basalt samples have slightly higher ratios of large ion lithophile elements (LILE) to high field strength elements (HFSE) elements (e.g., Ba/Ta and La/Ta) compared to the lower B Steens basalts at similar MgO concentration (Figure 13). Is an additional mantle or crustal component required?

High LILE/HFSE ratios are typically associated with convergent margin magmas, continental crust, and sediments derived from the continents. Mixing such materials with typical mantle peridotite would result in a strong isotopic overprint, because the Sr and Pb concentrations derived from subduction or crustal contaminants in particular are higher than typical mantle. The lack of an obvious isotopic distinction between the lower A and B Steens Basalts therefore precludes involvement of an additional, recently subduction-fluxed mantle, such as suggested by elevated Ba/Ta for the Picture Gorge Basalt (Figure 13; Brandon et al., 1993; Cahoon et al., 2020), or a substantial crustal component. The majority of the lower A Steens Basalt LILE/HFSE enrichment can be accounted for by a model of alternating cycles of Rayleigh fractionation (~40%), punctuated by periodic recharge of 50%, that is addition of half as much as the residual magma (Figure 14). We use a primitive member of the lower B Steens Basalt (onset of model lines, Figure 14) and a primitive recharge magma. Ba increases threefold while Ta only increases twofold over the fractionation-recharge models (Figure 14), leading to higher Ba/Ta ratios in the lower A Steens Basalt (Figure 13). The model can also explain the slightly elevated Sr in lower A Steens Basalt compared to lower B Steens Basalt. More voluminous and frequent recharge keeps the incompatible trace elements diluted during the lower B stage. There is however one lower A Steens Basalt sample with anomalously high Ba/Ta

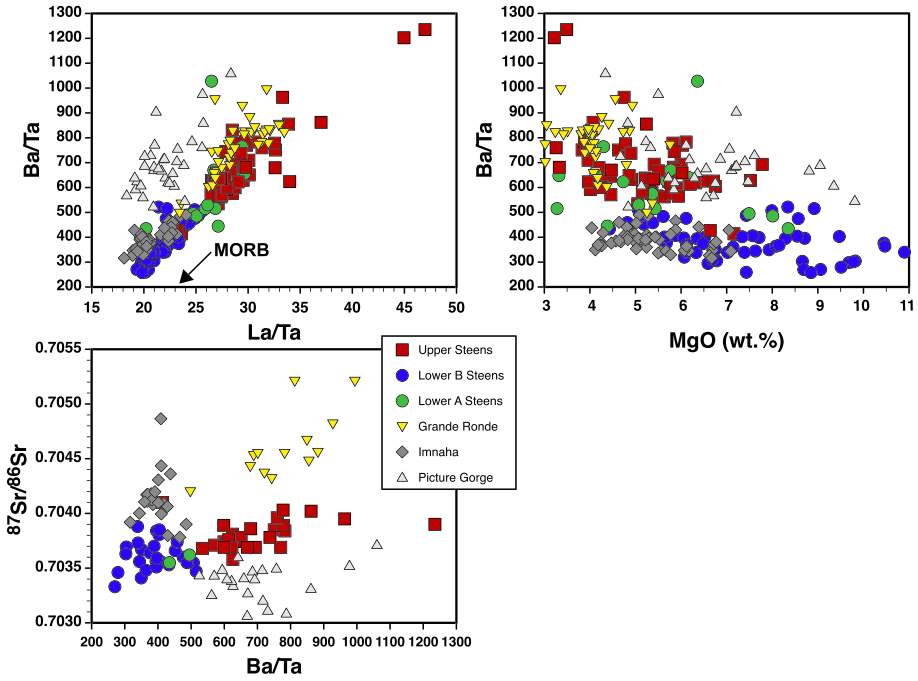

Figure 13. Comparison of LILE/HFSE ratios, $^{87}Sr/^{86}Sr$, and MgO for the Steens Basalt and other main stage formations of the CRBG. The arrow points to the direction where average mid-ocean ridge basalt (MORB) from Sun and McDonough (1989) would plot. Data from Camp and Hanan (2008), Wolff et al. (2008), Moore et al. (2018), and Cahoon et al. (2020).

(~6 wt.% MgO) that is a likely candidate for crustal contamination, given all samples from the other stages at that MgO content have much lower Ba/Ta (Figures 13 and 14).

We conclude that the lower A Steens Basalt represents early injection of basalts that have subequal contribution of ES and DS components and that undergo more crystallization than recharge, reflecting invasion into cool crust.

5.1.3. Increased Depleted Mantle Contribution During Recharge—Lower B Steens Basalt

The lower B Steens section contains the most magnesian samples, which most closely reflect the mantle source(s). The highest MgO samples have the lowest $^{87}Sr/^{86}Sr$ and $^{206}Pb/^{204}Pb$ and both isotope ratios roughly decrease with increasing stratigraphic height in the lower part of the lower B section, just as MgO generally increases; that is, successively higher samples move closer to the DS component that overlaps the Pacific MORB field (Figures 3 and 7). The increased contribution of the depleted mantle component is correlated with the time of greatest eruption rate and greatest magma recharge (see section 2).

Little to no crustal contamination occurs during this stage, given that the lower B Steens Basalt lies on or very near the trend expected for mixing between DS and ES in Sr, Nd, Pb, and Hf isotopic spaces (Figures 5 and 11). Furthermore, lower B samples have mantle values of $^{187}Os/^{188}Os$ (Figures 6 and 7), as well as low LILE/HFSE ratios (Figure 13). The small range of $^{187}Os/^{188}Os$ precludes a significant amount of pyroxenite in the Steens Basalt mantle source, as is suggested for some CFB (e.g., Heinonen et al., 2013; Pertermann & Hirschmann, 2003; Rogers et al., 2010), because pyroxenite tends toward high Re/Os ratios and hence evolves to high $^{187}Os/^{188}Os$ over relatively short time scales.

5.1.4. Late Mantle Components—Upper Steens Basalt

The upper Steens Basalt lavas have higher $^{87}Sr/^{86}Sr$ and lower $^{143}Nd/^{144}Nd$ at a given $^{206}Pb/^{204}Pb$ compared to the lower B Steens Basalt (Figures 11 and 12). This trajectory is similar to but not as pronounced as that of the Grande Ronde Basalts (Figure 11), which are interpreted to have significant cratonic crustal contamination (Carlson, 1984; Wolff et al., 2008; Wolff & Ramos, 2013). To estimate the mantle isotopic contribution, we choose the most mafic and lowest Ba/Ta members of the upper Steens suite that have characteristics similar to the lower A Steens and near the high end of the lower B Steens Ba/Ta array (Figures 13 and 14). These occur both low and midway up the upper Steens section and have $^{87}Sr/^{86}Sr$ similar to many of

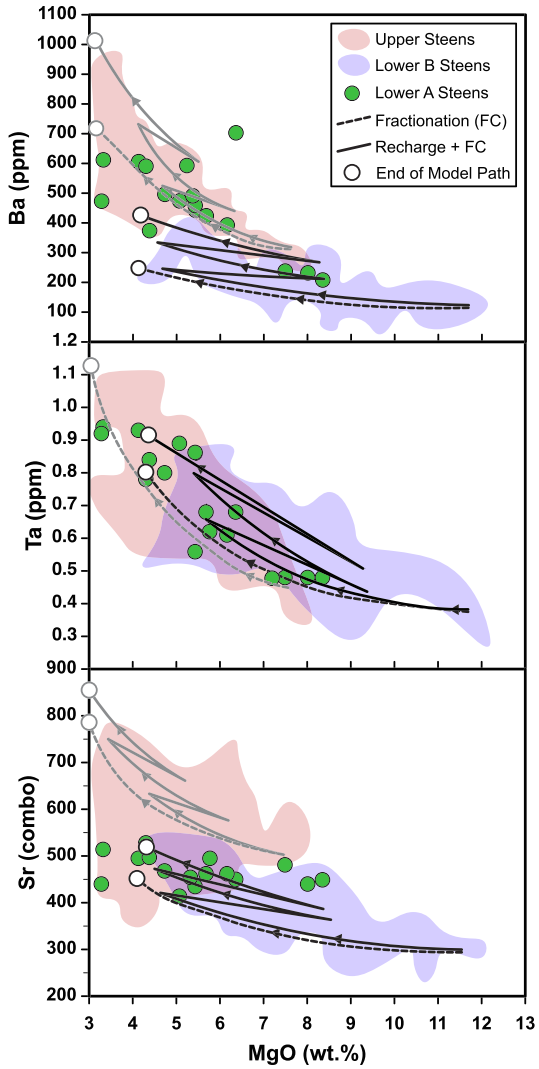

Figure 14. Fractionation (FC—dashed lines) and recharge-fractionation models (RFC—solid lines) for enrichment of select trace elements in Steens Basalt. Recharge events occur after 40% fractional crystallization (see excursions to higher MgO along the solid line paths) using a recharge magma composition calculated by adding 4% lower B Steens Basalt Fo_{86} olivine to the whole rock composition of sample NMSB18 (olivine and whole rock compositions from Moore et al., 2018). Fractionation calculated using $D_{Ba} = 0.01$, $D_{Ta} = 0.02$, and $D_{Sr} = 0.5$. Black solid or dashed lines are models using sample NMSB18 (lower B stage) as a parent, and gray solid or dashed lines are models using NMSB45 (upper Steens stage) as a parent (Moore et al., 2018). Modeled trends end at open black circles, after 50% crystallization in the FC models, and after two recharge and three fractionation episodes in the RFC models. Silica content (not shown) for all model paths stays within range of both lower B and upper Steens Basalts, respectively. The RFC path for the upper Steens parent model in the Ta panel is not shown for clarity and considering the other models cover nearly the full range of Steens Basalt Ta compositions.

the lower A and very earliest lower B Steens lavas. We thereby infer that the mantle source during upper Steens time is as it was during lower A Steens time and at the onset of the lower B Steens stage. Much of the distribution of upper Steens data trend toward and beyond the ES component, which we attribute to crustal effects (see section 5.2).

5.2. The Role of the Crust

The crust plays at least two main roles—as a material addition to the basaltic magmas, and as a host for intrusions and crystal cumulates formed by cooling magmas; these crystalline residua themselves become sources of (new) crustal contamination.

5.2.1. Crustal Assimilation

Addition of a crustal component to basalts during the upper Steens stage is supported by higher $^{87}Sr/^{86}Sr$ and $^{207}Pb/^{204}Pb$ coupled with generally less magnesian compositions and lower $^{143}Nd/^{144}Nd$ and $^{207}Pb/^{204}Pb$ at a given $^{206}Pb/^{204}Pb$ (Figures 11 and 12). Furthermore, $^{187}Os/^{188}Os$ is much higher than in lower B Steens Basalt at similar MgO (Figure 6) and Ba/Ta and La/Ta ratios are similar to the crustally contaminated Grande Ronde Basalt (Figure 13). Inasmuch as coupled recharge and fractionation can generate high Ba/Ta ratios (Figure 14), it is the combination of high Ba/Ta and La/Ta together with crustal isotopic signatures that support crustal contamination in the upper Steens Basalt. Wolff and Ramos (2013) note that although the range of Ba/Ta in the lower B Steens Basalt is small, the ratio increases in range and value in the upper Steens with decreasing MgO and a slight increase in average $^{87}Sr/^{86}Sr$. They propose basalt contamination by mafic accreted terranes, in contrast to a cratonic crust contaminant for Grande Ronde Basalt (which are mainly basaltic andesite lavas), which have higher and more variable $^{87}Sr/^{86}Sr$ and $^{187}Os/^{188}Os$ (Figures 7, 11, and 13). Basaltic rocks generally have very high Re/Os ratios in comparison to mantle peridotite and thus evolve to radiogenic Os quickly, allowing even young accreted mafic terranes to have sufficiently high $^{187}Os/^{188}Os$ (e.g., Carlson et al., 2018) to serve as the contaminant of the upper Steens basalt.

For simple modeling of the potential crustal contribution in the Steens Basalt, we use the OFT, a late Triassic to Cretaceous mafic arc terrane (Kurz et al., 2017) that crops out in the region (Walker et al., 1991). We choose a 5% partial melt of amphibolitic rocks, which would produce a tonalitic contaminant with arc-like isotopic affinities and that could have high $^{187}Os/^{188}Os$ (OFT in Table 3; Kurz et al., 2017). However, no $^{176}Hf/^{177}Hf$ or $^{187}Os/^{188}Os$ data are available for the OFT. We target isotope-isotope and coupled isotope-elemental trends that deviate most from the DS-ES mantle mixing array. These are general models and provide background for full further work on energy-balanced models coupled with detailed petrologic analysis in the future (Moore, 2018).

Mixing was modeled between basalts on or near the DS-ES mixing array and the partial melts from the OFT in each isotopic system, where two mixing curves between the mantle melts and crustal melts bracket the bulk of the data at a high and low end. For example, in $^{87}Sr/^{86}Sr$ versus $^{206}Pb/^{204}Pb$, the calculated mixed melt compositions at 40DS:60ES and 50DS:50ES were each separately mixed with the 5% OFT partial melt to create two separate mixing curves that bracket the bulk of the data (Figure 12). The mixing trends are

cast with variable rates of assimilation relative to crystallization (r of DePaolo, 1981), ranging from 0.2 to 0.8, in order to capture the trends in the Steens Basalt data.

While a contribution of as much as 30% OFT partial melt component could be argued by the mixing curves for a few lower A and B Steens Basalt compositions, neither the major nor trace element compositions require addition of a crustal component (Figure 12). This is also consistent with computational modeling (Graubard, 2016; Moore, 2018; Moore et al., 2018). In contrast, the upper Steens Basalt compositions fall on the mixing curves from 30% to as much as 70% mixing of OFT partial melt to the DS-ES mantle melt mixes. This range of crustal melt addition is inconsistent with the major element compositions in the upper Steens Basalt. The partial melts of OFT are tonalitic with ~69 wt.% SiO_2, and thus, a contribution by 30% or more of this melt composition to a starting composition of 48 wt.% SiO_2 (as in the recharge composition modeled in Figure 14) would result in melts with silica abundances *above* 54 wt.%, whereas 54 wt.% SiO_2 is the *maximum* value in the upper Steens lavas (Moore et al., 2018). Therefore, the amount of crustal contamination must be less than 30%. The true composition of the crustal contaminant may be slightly different than the estimates used here, or the amount of partial melting of the crust could vary, with the caveat that larger degrees of melt require more assimilation and hence more energy.

Binary mixing between partial melts from a strictly DS mantle, mixed with OFT crustal melts, plus fractionation can explain all the trends in the data for $^{87}Sr/^{86}Sr$ and $^{143}Nd/^{144}Nd$ versus 1/Sr and 1/Nd, respectively (Figures 15b and 15c). Fractionation drives compositions off the mixing line of DS melt-OFT melt toward higher Sr and Nd (or lower 1/Sr and 1/Nd). However, the data straddle the DS melt-OFT melt mixing curves in $^{87}Sr/^{86}Sr$ versus Ba and in all Pb isotopes versus 1/Pb (Figure 15), ruling out the possibility that magma generation is solely attributable to DS and OFT components. Only the most primitive lower B Steens Basalt samples, those that most convincingly lack a crustal assimilation signature, trend essentially between ES and DS melts. The bulk of the other Steens Basalt data can be explained by fractional crystallization coupled with minor crustal assimilation ($r \leq 0.1$) from these most primitive samples (Figure 15), with crustal contamination most prevalent in the upper Steens Basalt. A small contribution of such crust cannot be excluded for a few flows in lower A and B Steens Basalt.

Finally, some samples with $\delta^{18}O$ greater than ~6.2‰ (as high as 8.4‰ in upper Steens and 7.4‰ in the uppermost part of lower B Steens) are too high to be explained by crystal fractionation (Figures 9 and 10) and reflect some other open system process. Crustal contamination could be with isotopically immature mafic accreted terranes in these cases.

We estimate a probable upper limit of 15%–20% crustal contamination for some Steens Basalts. Even for low rates of assimilation ($r = 0.1$) of a 5% tonalitic partial melt of OFT composition (Table 3), by 90% remaining melt the model compositions reach ~54 wt.% SiO_2 (not shown), which is too high to account for the overwhelming majority of the Steens Basalt data (Moore et al., 2018). Conversely, this rate of assimilation is too low to account for the highest $\delta^{18}O$ abundances in the lower B and upper Steens (7.4‰ and 8.4‰, respectively; Figure 15). However, a mix between a parent magma of 6‰ $\delta^{18}O$ (represented by the bulk of the Steens Basalt data; Figure 10) and a contaminant with 10‰ $\delta^{18}O$ (from rhyolites coeval with the CRGB; Colón et al., 2015) would require 15% to 25% contamination by crustal melts to produce the highest $\delta^{18}O$ values in the Steens Basalt. This range of crustal melt contamination into a primitive Steens composition with 48 wt.% SiO_2 results in melts with silica contents of 51–54 wt.% SiO_2, within the range of the most evolved Steens Basalt samples (Moore et al., 2018). This simple binary mixing calculation does not take into account concurrent fractional crystallization, but it puts a probable upper limit of 15%–25% crustal felsic melt addition to the few crustally contaminated Steens Basalt lavas measured here. Given the extensive and repeated recharge and crystal fractionation, rates of felsic melt assimilation of a few tenths (r, DePaolo, 1981) relative to crystallization pose no energetic barrier.

5.2.2. Crystallization and Crustal Cumulate Addition

Abundant fractionation is evident in that radiogenic isotopic ratios vary little over a substantial range of MgO in the Steens Basalt (Figure 3). In addition, when taking into account the small fractionation factor between plagioclase and basaltic melt ($\Delta^{18}O$ plagioclase melt) of approximately 0.1‰ (see section 4.3), the bulk of the $\delta^{18}O$ data are recast to indicate a melt range mainly from 5.9‰ to 6.1‰ (Figure 10). This range requires significant fractional crystallization from parental magmas that likely had initial $\delta^{18}O$ of ~5.5‰ (for the bulk of primitive basalts; Bindeman, 2008). Fractionation of the Steens mineral assemblage of olivine,

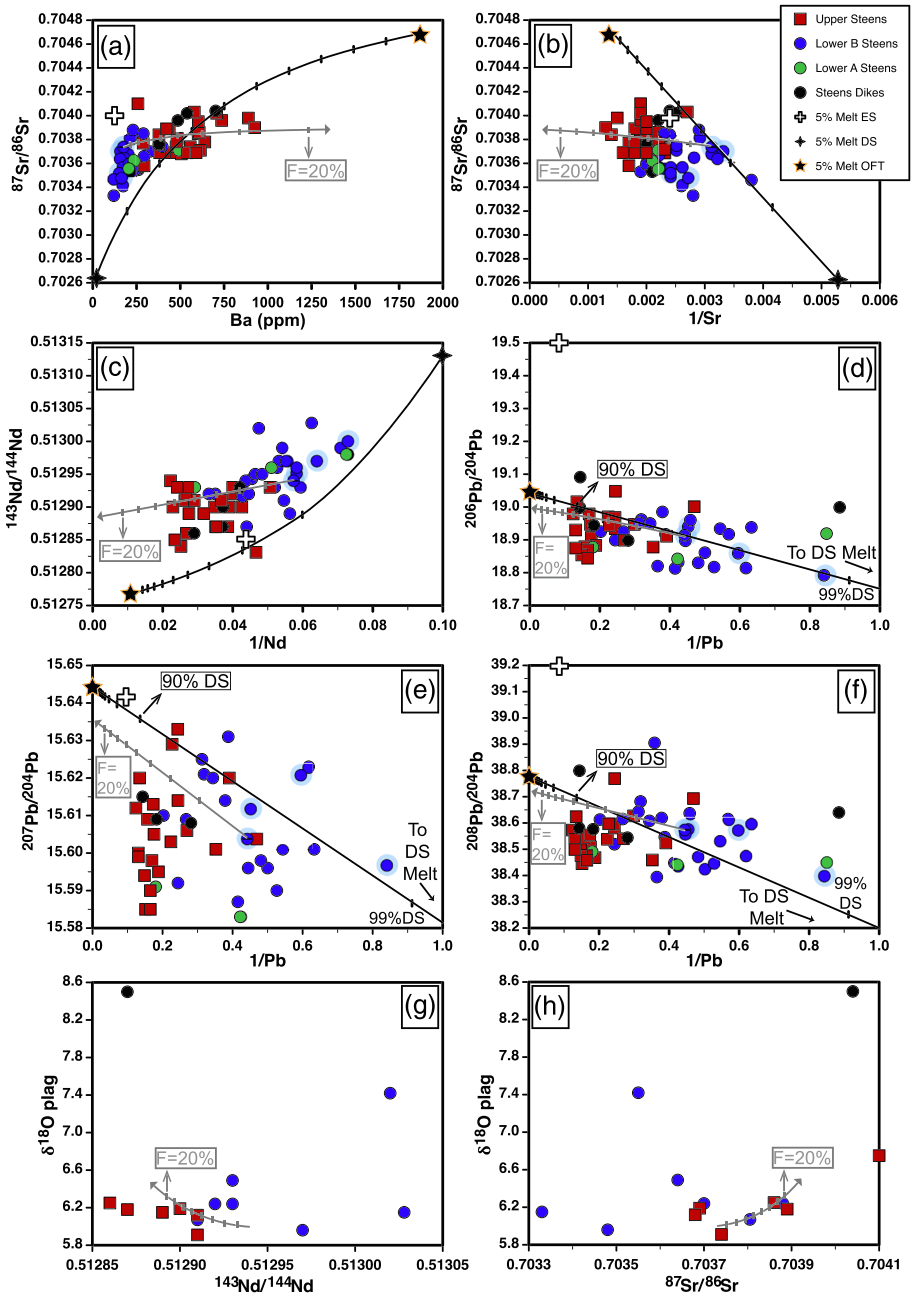

Figure 15. Binary mixing models for 5% partial melts of depleted source (DS) plus Olds Ferry Terrane (OFT) and assimilation-fractional crystallization (AFC) models of primitive lower B Steens melts in select isotope and trace element spaces. Black lines are binary mixing between 5% partial melts of DS and OFT, where tick marks represent 10% increments of mixing, except for the Pb–Pb plots, where ticks for 99% DS-1% OFT are also shown. Light blue highlighted samples are the most primitive samples from the lower B stage, those on the high MgO trend that lack a crustal assimilation signature. A 5% melt of enriched source (ES) mantle is also shown for reference. Gray lines are AFC (assimilation-fractional crystallization) models using the equations of DePaolo (1981), where tick marks appear at 10% decrements of remaining melt and the rate of assimilation to crystallization (r) is 0.1. The models end at 20% remaining melt, just beyond the maximum amount of fractionation allowable to reach the most evolved Steens Basalt compositions. Parent magma for the AFC models is Steens Basalt sample NSMB18 (Moore et al., 2018) and the crustal contaminant is a 5% partial melt of OFT (Table 3).

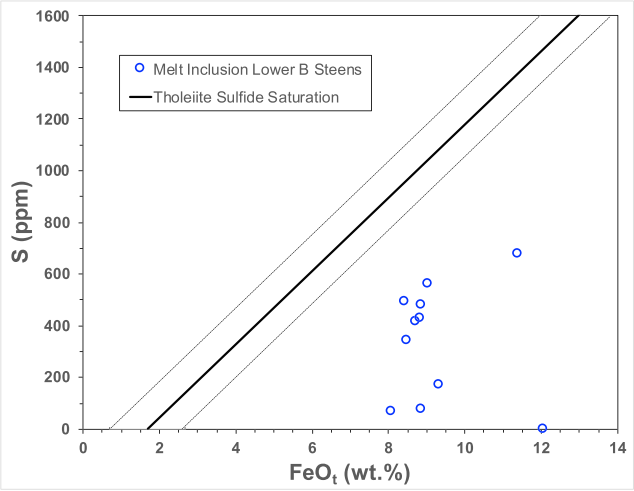

Figure 16. Sulfur versus total FeO for a preliminary set of analysis on rehomogenized melt inclusions in olivine from the lower B Steens Basalt. Black line is the sulfide saturation regression line of Blake et al. (2010) determined by the best fit correlation of MORB and Hawaiian tholeiite basaltic glasses; dashed lines bracketing the regression line are the 1σ error envelope.

clinopyroxene and plagioclase, from 9.5 to 4 wt.% MgO, increases $\delta^{18}O$ by ~0.2‰ (Figure 9), using $\delta^{18}O$ fractionation factors of ~0.4‰ and 1‰, respectively for Δclinopyroxene-melt and Δolivine-melt (e.g., Eiler et al., 2000). Such fractionation leaves ultramafic to gabbroic cumulates behind that may exist as layered mafic intrusions or, if crystal removal is inefficient, in mafic gabbroic bodies.

A combination of abundant clinopyroxene fractionation at depth and of olivine ± plagioclase ± clinopyroxene at shallow crustal levels can explain the bulk of measured $\delta^{18}O$ in the Steens Basalt, as well as much of the range of the other main phase CRBG (Figure 10). Using rhyolite-MELTS (Gualda et al., 2012) and a parent magma of primitive lower B Steens composition (sample NMSB18; Moore et al., 2018), fractionation was modeled over a range of crustal pressures relevant to the crustal thickness in the Steens Mountain region to determine the mineral assemblage at various depths (supporting information Figure S1). Models were run at FMQ and with 0.5% water in the starting composition, consistent with mineral assemblages observed and inferred at depth as well as low water contents indicated by olivine-hosted melt inclusion analyses (supporting information Table S2); higher water suppresses plagioclase and expands orthopyroxene stability. From ~600 to 1,000 MPa, clinopyroxene is the sole liquidus phase, and fractionates alone until 40%–45% crystallization. From ~400–500 MPa, olivine is the liquidus phase, but orthopyroxene, which is not part of the phase assemblage of the Steens Basalt, appears after only a few percent crystallization of olivine. From ~200 to 300 MPa, olivine is the liquidus phase until clinopyroxene begins fractionating after ~11% crystallization. From shallow to 100 MPa, olivine is the liquidus phase until plagioclase begins fractionating after ~11% crystallization. Olivine has the largest Δmineral melt and, thus, is most efficient at increasing the $\delta^{18}O$ of remaining melt; however, fractionation of 27%–30% olivine as the sole crystallizing phase is required to raise $\delta^{18}O$ of melt from 5.5‰ to ~5.9‰. Because either clinopyroxene or plagioclase join olivine as crystallizing phases after only 11% fractionation in the upper crust, there is not enough fractionation of olivine alone at shallow depths to account for the bulk of the data. However, fractionation of ~45%–60% clinopyroxene as the sole crystallizing phase can account for the same increase in $\delta^{18}O$ in Steens Basalt compositions. Barometry and MCS modeling for the Steens Basalt magmatic system suggests a shallow storage regime (Graubard, 2016; Moore, 2018; Moore et al., 2018), but given the phase equilibria, clinopyroxene fractionation must have taken place at greater depth than the mid to upper crustal levels where the basalts last equilibrated. The ~30 km depth below which the phase equilibria project only clinopyroxene fractionation (supporting information Figure S1) also coincides with a ~3 km thick seismically imaged region in the crust beneath Steens Mountain that transitions to higher velocity and density (~7.2–7.4 m/s and 2.95 cm^3, respectively; Eagar et al., 2011). This deep crustal fractionation process may have also efficiently removed clinopyroxene at depth, leaving behind a dense cumulate layer, and is ultimately responsible for the lack of clinopyroxene as a phenocryst phase in most Steens lavas (Moore et al., 2018). The existing mineral assemblage in the erupted lavas is largely in equilibrium with the host rocks, so shallower fractionation overprinted any deeper crustal history recorded in the minerals. This cryptic clinopyroxene fractionation signal has been recognized by other CFB workers (cf. Cox, 1980; Wright et al., 1973).

5.3. Crustal Sulfide Scavenging? High Os in the Lower B Steens Basalt

The lower B Steens Basalt has lavas that are particularly rich in Os (Table 2) for basalts at comparable MgO (Figure 6b). Osmium is extraordinarily compatible in sulfide minerals and even more so in sulfide melts (partition coefficients of 10^4–10^6; Hart & Ravizza, 1996; Roy-Barman et al., 1998; Mungall & Brenan, 2014), so modest accumulation of such phases might account for high Os contents. The absence of petrographic evidence of sulfides in any analyzed sample indicates that the lower B Steens lavas are sulfide undersaturated. Rehomogenized melt inclusions in olivine from two lower B Steens Basalt flows range only as high as 700 ppm S, which is consistent with sulfide undersaturation (Figure 16; supporting information) when applying the Blake et al. (2010) model that uses correlation between increasing FeO$_t$ and S capacity for

determining sulfide saturation in tholeiites at low fO_2. In contrast, Davis et al. (2017) demonstrate that melt inclusions from several Grande Ronde members are sulfide saturated and Wierman (2018) reports sulfide blebs in upper Steens Basalt; both suites have overall more evolved compositions.

The high Os concentrations of the lower B Steens Basalt are unlikely to have been contributed by the ambient crust or by mantle melting. Most crustal rocks have low Os concentrations, and Mesozoic accreted terranes will have elevated $^{187}Os/^{188}Os$. The one upper Steens Basalt sample analyzed here has elevated $^{187}Os/^{188}Os$ and very low Os content (Figure 6), consistent with crustal contamination, and differs from the mantle-like $^{187}Os/^{188}Os$ and elevated Os concentrations of the lower B Steens Basalt. The highest Os concentrations are in the lower B Steens Basalt samples with the highest MgO and so are linked to high recharge. Highest recharge, in turn, is linked to the greatest amount of DS (MORB-like) mantle contribution to magmatism and therefore these magmas are unlikely to be born as Os-rich melt. A different explanation is needed.

High Os concentrations can be achieved by consumption of an Os-rich phase, such as sulfide, during passage through the mantle or, alternatively, by rising magmas scavenging an Os-rich phase (sulfide) out of crystallized gabbroic or ultramafic residua in the crust, produced by prior crystallization in the Steens Basalt magmatic system. Though Cu and Ni are also compatible in sulfides (but not Cr), their partition coefficients in sulfides are orders of magnitude smaller than for Os (Kiseeva et al., 2017; Rajamani & Naldrett, 1978; Sattari et al., 2002). Magmatic scavenging of a minimal amount of sulfide will not significantly affect Ni nor Cu concentrations (Figure 8), whereas the osmium budget is essentially entirely controlled by the sulfide phase. For example, using the distribution coefficients for Ni (351), Cu (913), and Os (48,000) between basaltic melt and sulfide (Francis, 1990; Roy-Barman et al., 1998) and with assumed primary magma composition of Ni = 200 ppm, Cu = 130 ppm, and Os = 0.08 ppb, assimilation of 0.02% of sulfide previously crystallized from a similar composition magma would raise the Os content to 0.85 ppb while increasing Ni by 14 ppm and Cu by 24 ppm.

In light of the oxygen isotopic evidence for deep crustal fractional crystallization of basalt beneath the Steens volcanic locus, we favor a scenario in which sulfides are precipitated at similar depth from fractionation in the Steens Basalt system and consumed by later ascending recharge melts. For basaltic melts at 1200 °C and shallow crustal levels (~1 atm-300 MPa), sulfide saturation is achieved at ~1,000 ppm S (Mavrogenes & O'Neill, 1999). Extensive crystallization of mafic phases (~60%) could cause a basaltic melt to achieve ~700 ppm S and become sulfide saturated at moderate depths in the crust (Mavrogenes & O'Neill, 1999). If a sulfide undersaturated recharge magma is introduced into a chamber that has extensively crystallized to the point of sulfide saturation, the undersaturated recharge magma would consume the sulfides that crystallized from the evolved melt. Given the range of MgO compositions in the lower B Steens Basalt (as low as ~4.5 wt.% MgO), up to 70% fractionation in the more evolved melts is realistic. As an example, a basaltic mantle melt generated at 5,000 MPa and 1350 °C is sulfide saturated at 385 ppm S (Mavrogenes & O'Neill, 1999). As this melt ascends, it immediately becomes sulfide undersaturated, as decreasing pressure increases the sulfur content of sulfide saturation. If such a melt stalls and fractionates only clinopyroxene at 1,000 MPa, ~52% crystallization is necessary to increase the S content to 730 ppm, which is the S content for sulfide saturation at that pressure (Mavrogenes & O'Neill, 1999). This amount of deep clinopyroxene crystallization is in agreement with the 45%–60% crystallization that we suggest achieves the elevated $\delta^{18}O$ compositions of some Steens Basalt lavas, and 730 ppm S is comparable to the highest S contents measured in melt inclusions from olivine in the lower B Steens Basalt (up to 700 ppm; supporting information). Therefore, consumption of Os-rich sulfide during recharge magma ascent through crust containing juvenile gabbroic, sulfide bearing cumulates is a plausible explanation for high Os concentrations in the lower B Steens Basalt. This favored scenario of elevating Os concentrations by sulfide scavenging in the lower B Steens Basalt, combined with our interpreted changes in mantle sources, crustal contributions, and variation of dominant differentiation processes in time provides a schematic view of the Steens Basalt magmatic system from mantle to crust throughout the three-stage evolution (Figure 17).

Attributing the high Os concentrations in the lower B Steens Basalt to their mantle source is difficult given uncertainty in the sulfide abundance and composition of various mantle sources. Hauri (2002) calls on accumulation of disaggregated peridotite to explain OIB Os concentrations of 1 ppb. Hart and Ravizza (1996) report Os concentrations of 4.1 ppm in sulfides from Kilbourne Hole lherzolites; if this is a typical value

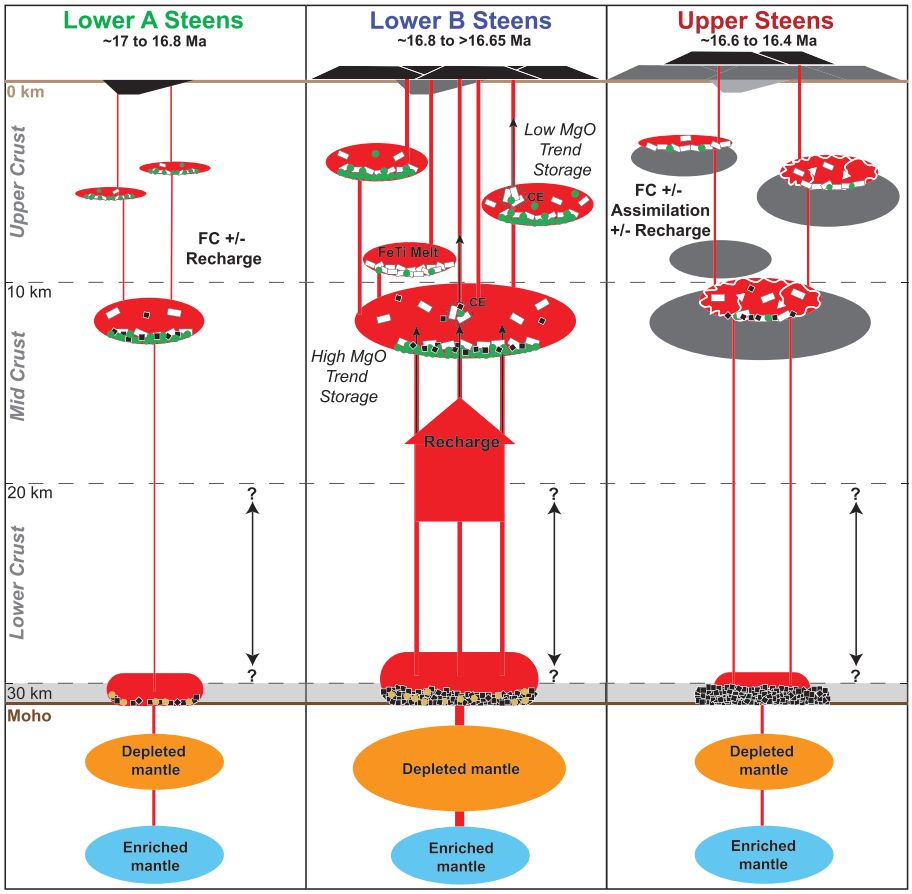

Figure 17. Schematic summary of mantle sources, crustal process and contributions to the three-stage evolution of the Steens Basalt. From left to right: emplacement of lower A Steens Basalt, topography filling; lower B Steens Basalt, the main, most widely distributed eruption sequence; upper Steens Basalt, latest and not as widely distributed (see Bondre & Hart, 2008; Brueseke et al., 2007; Camp et al., 2013; Moore et al., 2018). Green circles represent olivine crystallization, black squares are clinopyroxene, white rectangles are plagioclase, and gold hexagons are sulfides. FC = fractional crystallization; CE = cumulate entrainment; Fe-Ti melt = iron and titanium rich melt; see text for discussion of processes. Question marks in lower crust reflect uncertainty of exact depth of cryptic clinopyroxene only crystallization, as clinopyroxene is the liquidus phase through 40% crystallization from ~30 up to ~20 km. Light gray transparent range at the base of the crust represents the ~3 km thick region seismically imaged to have higher velocity and density (~7.2–7.4 m/s and 2.95/cm^3; Eagar et al., 2011), which coincides with a proposed region of abundant clinopyroxene only fractionation from this study. This region is also the probable location of sulfide fractionation and consumption by later recharge melts. White curves and arrows indicate assimilation of crustal melts. Gray magma chambers in upper Steens panel represent the solid cumulate residue of prolonged fractionation of olivine, clinopyroxene, and plagioclase, resulting in shoaling of the magmatic system through time.

for Os in mantle sulfide, then very minor sulfide consumption (~0.03%) can produce basalt concentrations as high as 1 ppb, as in the lower B Steens Basalt (up to 0.9 ppb). A partial melt from the ES mantle used in the models presented here is likely generated at a higher pressure compared to a partial melt from the modeled DS mantle. Decreasing pressure during magma ascent increases sulfide solubility, causing sulfide saturated melts to become undersaturated as they depressurize. If an ascending sulfide undersaturated melt then encounters residual sulfides in the surrounding mantle through which it passes, it will scavenge those sulfides (Mavrogenes & O'Neill, 1999). During the onset of the lower B Steens Basalt stage, the recharge magma has a larger ES source contribution; these samples have comparably elevated $^{87}Sr/^{86}Sr$ and $^{206}Pb/^{204}Pb$ and contain high Os concentrations (up to 0.73 ppb) and some relatively high MgO lavas (Figure 3). $^{87}Sr/^{86}Sr$ and $^{206}Pb/^{204}Pb$ decrease late in the lower B Steens section, where the DS component contribution increases and where MgO and Os concentrations are the highest in the lower B Steens (up to ~12% and 0.86 ppb, respectively; Figures 3, 6, and 7). If the mantle sources do contribute to the high Os

signature, then they must have similar Os compositions or sulfide abundances, which is highly improbable due to the nature of a depleted source. Sulfide consumption in the mantle is also difficult to support taking into consideration there are few worldwide mantle derived/parental magmas with the high Os concentrations observed in the lower B Steens Basalt (Figure 6b).

Alternatively, some workers have proposed that accumulation of lithospheric and/or xenocrystic olivine can also produce magmas with high Os concentrations (Hopkins et al., 2016; Reisberg et al., 1993). Partition coefficients estimated for Os in olivine/melt range from 1 to 20, with one value from a disequilibrium case as high as 200 (Hart & Ravizza, 1996; Luguet et al., 2007; Martin et al., 1994). Though Os is compatible in this mineral phase, partition coefficients are at least 1,000 times lower than those estimated for Os in sulfide/melt. Hart and Ravizza (1996) report Os concentrations in olivine from mantle lherzolite and primitive basalts mostly ~0.2 ppb, but one analysis from an olivine in lherzolite contains ~2.4 ppb. Addition of olivine with Os concentrations ~0.2 ppb is insufficient to raise Os to the values in the lower B Steens Basalt; addition of ~35% olivine with Os concentrations of 2.4 ppb would be required to raise a melt of ~0.05 ppb (an average basalt) to 0.9 ppb. This is an unreasonable amount of olivine accumulation given the required increase in MgO that would accompany such a process, producing a new melt + cumulates of ~20 wt.% MgO (from a starting melt of ~9 wt.% MgO). Some lower B Steens Basalt samples may contain accumulated cognate olivine, but as a very minor component given MgO is ≤12 wt.%. There is no textural evidence of xenocrystic olivine, and forsterite compositions of olivine are homogeneous within crystals (Moore et al., 2018). Contributions by assimilated lithospheric olivine are unlikely given olivine in the lower B Steens Basalt is not in equilibrium with the mantle, as would be expected if olivine was accumulated from such a component (Fo ≤ 86 in lower B Steens; Moore et al., 2018). The lack of evidence of accumulative olivine in the petrographic and geochemical data leads us to the conclusion that this is an unlikely scenario for obtaining the elevated Os concentrations in the lower B Steens Basalt. Though Os is also highly compatible in chromite, magma consumption of chromite poses a similar issue to that of olivine. Accumulation of modest amounts of chromite can achieve the Os compositions of the lower B Steens Basalt; for example, Os in chromites from an Hawaiian tholeiite and a MORB from the East Pacific Rise are 24.6 and 7.2 ppb, respectively (Pagé & Barnes, 2016). Addition of ~5% and 12% chromite of these compositions respectively can raise an average basaltic melt from ~0.05 to 0.9 ppb Os. However, given these same chromites have ~46% and ~30 wt.% Cr_2O_3, respectively, accumulation of that amount of chromite will produce magmas with a few percent Cr_2O_3, whereas the lower B Steens Basalt compositions are ~0.1 wt.% Cr_2O_3 or less (Moore et al., 2018).

6. Conclusions

New and existing radiogenic isotopic compositions require at least two distinct mantle sources for the Steens Basalt: an enriched component similar to the source of Imnaha basalts and a depleted mantle component similar to the source of Pacific MORB. A third component is required by isotopic compositions of some Steens Basalt lavas; contamination by mafic accreted terrane crust, similar in composition to the OFT, is likely responsible for this trend.

The lower A Steens Basalt isotopic compositions can be modeled by mixing of roughly equal proportions of depleted and enriched mantle sources. These lavas show little evidence of crustal assimilation, as relatively high Ba/Ta ratios can largely be explained by repeated episodes of fractionation and recharge. Mixing of the depleted and enriched mantle sources in approximately equal proportions continues into the waxing stage, the lower B Steens Basalt. The homogeneity of $^{187}Os/^{188}Os$ in the lower B Steens Basalt lavas suggests that the $^{187}Os/^{188}Os$ ratio of depleted and enriched mantle sources is similar. Input of the DS component increases in time within the lower B Steens Basalt and contributes as much as 70% of the mantle source for some lavas erupted later in the stage, during initiation of the waning period, when fractionation begins to outpace recharge. Lower B Steens Basalt Os concentrations require a contribution from an Os-rich source, most likely from consumption of a cognate sulfide phase while recharge magmas ascend through the crust. Lower B Steens Basalt generally lacks isotopic and trace element signatures reflective of assimilation of crustal melts, and crustal contamination is not required for most lavas from this stage by isotopic mixing models. Voluminous fractionation at both deep and shallow crustal levels occurs during this stage, elevating $\delta^{18}O$ above parental basaltic melt values, which continues into the upper Steens stage.

During the upper Steens Basalt stage, the depleted and enriched mantle end-members contribute subequal proportions, with some samples suggesting a greater contribution by the enriched mantle. The magmatic system is now well established in this stage; magmatism has thermally primed the mafic accreted terrane crust in which the magmas have stalled and fractionated. This allows for melting of mafic terrane crust, similar in composition to the OFT, which assimilates with mantle melts that together generate the upper Steens Basalt.

The data presented here further resolves changing mantle source and crustal effects during the three-stage petrochemical evolution proposed for the Steens Basalt. A more detailed schematic view from the mantle through the crust in the Steens Basalt magmatic system is elucidated. The Steens Basalt mantle source and crustal contamination model presented here is similar to models proposed for other continental flood basalts and suggests that continental flood basalt provinces share a similar generation and evolution history.

Data Availability Statement

The data set for this research is available in the EarthChem Library at doi.org/10.1594/IEDA/111473 (Moore et al. 2020, Steens Basalt Sr, Nd, Pb, Hf, Os, and O Isotopic Compositional Data).

Acknowledgments

Funding for this project was provided by the NSF (EAR 1427716 and 1427737) and a Geological Society of America Graduate Student Research Grant. Very special thanks to Dave Graham for his assistance in the Noble Gas Geochemistry Lab at Oregon State University, for clarifying He analytical methods, for his helpful thoughts and advice on isotope mixing models, and for his contributions to the interpretation of new Steens Basalt isotopic data. We thank Matt Brueseke, John Shervais, and an anonymous reviewer for their insightful and thorough comments that contributed to improvement of this manuscript.

References

Anderson, D. L. (2005). Large igneous provinces, delamination, and fertile mantle. *Elements*, *1*, 271–275. https://doi.org/10.2113/gselements.1.5.271

Bailey, D. G., & Conrey, R. M. (1992). Common parent magma for Miocene to Holocene mafic volcanism in the northwestern United States. *Geology*, *20*, 1131–1,134. https://doi.org/10.1130/0091-7613(1992)020<1131:cpmfmt>2.3.co;2

Bailey, M. M. (1989). Revisions to stratigraphic nomenclature of the Picture Gorge Basalt Subgroup, Columbia River Basalt Group. *Geological Society of America Special Papers*, *239*, 67–84. https://doi.org/10.1130/spe239-p67

Baksi, A. K. (2010). Comment on "Distribution and geochronology of Oregon Plateaus (U.S.A) flood basalt volcanism: The Steens Basalt revisited". *Journal of Volcanology and Geothermal Research*, *196*, 134–138. https://doi.org/10.1016/j.jvolgeores.2010.04.007

Barry, T. L., Kelley, S. P., Reidel, S. P., Camp, V. E., Self, S., Jarboe, N. A., et al. (2013). Eruption chronology of the Columbia River Basalt Group. *Geological Society of America Special Papers*, *497*, 45–66. https://doi-org.ccl.idm.oclc.org/10.1130/SPE497

Bendaña, S., Bohrson, W. A., Graubard, M. A., Moore, N. E., & Grunder, A. L. (2017). *Quantification of mantle vs. crustal contributions to the Steens Flood Basalt magmatic system*. Portland, OR: IAVCEI Scientific Assembly. Abstract ME23C-070

Bendaña, S. J. (2016). *Documenting mantle and crustal contributions to flood basalt magmatism via computational modeling of the Steens Basalt, southeast Oregon [M.S. Thesis]*. Ellensburg, WA: Central Washington University. 183 p

Bindeman, I. (2008). Oxygen isotopes in mantle and crustal magmas as revealed by single crystal analysis. *Reviews in Mineralogy and Geochemistry*, *69*, 445–478. https://doi.org/10.2138/rmg.2008.69.12

Blake, S., Self, S., Sharma, K., & Sephton, S. (2010). Sulfur release from the Columbia River Basalts and other flood lava eruptions constrained by a model of sulfide saturation. *Earth and Planetary Science Letters*, *299*, 328–338. https://doi.org/10.1016/j.epsl.2010.09.013

BlichertToft, J., Chauvel, C., & Albarède, F. (1997). Separation of Hf and Lu for high precision isotope analysis of rock samples by magnetic sector-multiple collector ICPMS. *Contributions to Mineralogy and Petrology*, *127*, 248–260. https://doi.org/10.1007/s004100050278

Bohrson, W. A., & Spera, F. J. (2001). Energy-constrained open-system magmatic processes II: Application of energy-constrained assimilation-fractional crystallization (EC-AFC) model to magmatic systems. *Journal of Petrology*, *42*, 1019–1,041. https://doi.org/10.1093/petrology/42.5.1019

Bohrson, W. A., Spera, F. J., Ghiorso, M. S., Brown, G. A., Creamer, J. B., & Mayfield, A. (2014). Thermodynamic model for energy-constrained open-system evolution of crustal magma bodies undergoing simultaneous recharge, assimilation and crystallization: The magma chamber simulator. *Journal of Petrology*, *55*, 1685–1717. https://doi.org/10.1093/petrology/egu036

Bondre, N. R., & Hart, W. K. (2008). Morphological and textural diversity of the Steens Basalt lava flows Southeastern Oregon, USA: Implications for emplacement style and nature of eruptive episodes. *Bulletin of Volcanology*, *70*, 999–1018. https://doi.org/10.1007/s00445-007-0182-x

Brandon, A. D., & Goles, G. G. (1988). A Miocene subcontinental plume in the Pacific Northwest: geochemical evidence. *Earth and Planetary Science Letters*, *88*, 273–283. https://doi.org/10.1016/0012-821x(88)90084-2

Brandon, A. D., & Goles, G. G. (1995). Assessing subcontinental lithospheric mantle source for basalts Neogene volcanism in the Pacific Northwest, USA as a test case. *Contributions to Mineralogy and Petrology*, *121*, 364–379. https://doi.org/10.1007/s004100050102

Brandon, A. D., Hooper, P. R., Goles, G. G., & Lambert, R. S. J. (1993). Evaluating crustal contamination in continental basalts: The isotopic composition of the Picture Gorge Basalt of the Columbia River Basalt Group. *Contributions to Mineralogy and Petrology*, *114*, 452–464. https://doi.org/10.1007/bf00321750

Brueseke, M. E., Heizler, M. T., Hart, W. K., & Mertman, S. A. (2007). Distribution and geochronology of Oregon Plateaus (U.S.A) flood basalt volcanism: The Steens Basalt revisited. *Journal of Volcanology and Geothermal Research*, *161*, 187–214. https://doi.org/10.1016/j.jvolgeores.2006.12.004

Cahoon, E. B., Streck, M. J., Koppers, A. A. P., & Miggins, D. P. (2020). Reshuffling the Columbia River Basalt chronology—Picture Gorge Basalt, the earliest- and longest-erupting formation. *Geology*, *48*, 348–352. https://doi.org/10.1130/G47122.1

Camp, V. E., & Hanan, B. B. (2008). A plume-triggered delamination origin for the Columbia River Basalt Group. *Geosphere*, *4*(3), 480. https://doi.org/10.1130/ges00175.1

Camp, V. E., & Ross, M. E. (2004). Mantle dynamics and genesis of mafic magmatism in the Intermontane Pacific Northwest. *Journal of Geophysical Research*, *109*, B08204. https://doi.org/10.1029/2003JB002838

Camp, V. E., Ross, M. E., Duncan, R. A., Jarboe, N. A., Coe, R. S., Hanan, B. B., & Johnson, J. A. (2013). The Steens Basalt: Earliest lavas of the Columbia River Basalt Group. In *Geological Society of America Special Papers* (Vol. 497, pp. 87–116). Boulder, CO: https://doi-org.ccl.idm.oclc.org/10.1130/SPE497

Camp, V. E., Ross, M. E., & Hanson, W. E. (2003). Genesis of flood basalts and Basin and Range volcanic rocks from Steens Mountain to the Malheur River Gorge, Oregon. *Geological Society of America Bulletin*, *115*, 105–128. https://doi.org/10.1130/0016-7606(2003)115<0105:gofbab>2.0.co;2

Carlson, R. W. (1984). Isotopic constraints on Columbia River flood basalt genesis and the nature of the subcontinental mantle. *Geochimica et Cosmochimica Acta*, *48*, 2,357–2,372. https://doi.org/10.1016/0016-7037(84)90231-x

Carlson, R. W., Grove, T. L., & Donnelly-Nolan, J. (2018). Origin of primitive tholeiitic and calc-alkaline basalts at Newberry Volcano, Oregon. *Geochemistry, Geophysics, Geosystems*, *19*, 1360–1,377. https://doi.org/10.1029/2018GC007454

Carlson, R. W., & Hart, W. K. (1987). Crustal genesis on the Oregon Plateau. *Journal of Geophysical Research*, *92*, 6191–6206. https://doi.org/10.1029/jb092ib07p06191

Carlson, R. W., Lugmair, G. W., & Macdougall, J. D. (1981). Columbia River volcanism: The question of mantle heterogeneity or crustal contamination. *Geochimica et Cosmochimica Acta*, *45*, 2483–2,499. https://doi.org/10.1016/0016-7037(81)90100-9

Cheng, L. L., Yang, Z. F., Zeng, L., Wang, Y., & Luo, Z. H. (2014). Giant plagioclase growth during storage of basaltic magma in Emeishan Large Igneous Province, SW China. *Contributions to Mineralogy and Petrology*, *167*, 1–20. https://doi.org/10.1007/s00410-014-0971-0

Chesley, J. T., & Ruiz, J. (1998). Crust–mantle interaction in large igneous provinces: implications from the Re–Os isotope systematics of the Columbia River flood basalts. *Earth and Planetary Science Letters*, *154*, 1–11. https://doi.org/10.1016/s0012-821x(97)00176-3

Coffin, M. F., & Eldholm, O. (1994). Large igneous provinces: crustal structure, dimensions, and external consequences. *Reviews of Geophysics*, *32*, 1–36. https://doi.org/10.1029/93rg02508

Colón, D. P., Bindeman, I. N., Stern, R. A., & Fisher, C. M. (2015). Isotopically diverse rhyolites coeval with the Columbia River Flood Basalts: Evidence for mantle plume interaction with the continental crust. *Terra Nova*, *27*, 270–276. https://doi.org/10.1111/ter.12156

Courtillot, V. E., & Renne, P. R. (2003). On the ages of flood basalt events. *Comptes Rendus Geoscience*, *335*, 113–140. https://doi.org/10.1016/s1631-0713(03)00006-3

Cox, K. G. (1978). Flood basalts, subduction and the break-up of Gondwanaland. *Nature*, *274*, 47–49. https://doi.org/10.1038/274047a0

Cox, K. G. (1980). A model for flood basalt vulcanism. *Journal of Petrology*, *21*, 629–650. https://doi.org/10.1093/petrology/21.4.629

Davis, K. N., Wolff, J. A., Rowe, M. C., & Neill, O. K. (2017). Sulfur release from main-phase Columbia River Basalt eruptions. *Geology*, *45*, 1043–1,046. https://doi.org/10.1130/g39371.1

DePaolo, D. J. (1981). Trace element and isotopic effects of combined wallrock assimilation and fractional crystallization. *Earth and Planetary Science Letters*, *53*, 189–202. https://doi.org/10.1016/0012-821x(81)90153-9

Eagar, K. C., Fouch, M. J., James, D. E., & Carlson, R. W. (2011). Crustal structure beneath the High Lava Plains of eastern Oregon and surrounding regions from receiver function analysis. *Journal of Geophysical Research*, *116*, B02313. https://doi.org/10.1029/2010jb007795

Eiler, J. M., Crawford, A., Elliott, T. I. M., Farley, K. A., Valley, J. W., & Stolper, E. M. (2000). Oxygen isotope geochemistry of oceanic-arc lavas. *Journal of Petrology*, *41*, 229–256. https://doi.org/10.1093/petrology/41.2.229

Elkins-Tanton, L. T. (2005). Continental magmatism caused by lithospheric delamination. *Geological Society of America Special Papers*, *388*, 449–462. https://doi.org/10.1130/0-8137-2388-4.449

Ernst, R. E. (2014). *Large Igneous Provinces*. Cambridge: Cambridge University Press. 653 p.

Francis, R. D. (1990). Sulfide globules in mid-ocean ridge basalts (MORB), and the effect of oxygen abundance in Fe-S-O liquids on the ability of those liquids to partition metals from MORB and komatiite magmas. *Chemical Geology*, *85*, 199–213. https://doi.org/10.1016/0009-2541(90)90001-n

Gannoun, A., Burton, K. W., Parkinson, I. J., Alard, O., Schiano, P., & Thomas, L. E. (2007). The scale and origin of the osmium isotope variations in mid-ocean ridge basalts. *Earth and Planetary Science Letters*, *259*, 541–556. https://doi.org/10.1016/j.epsl.2007.05.014

Garfunkel, Z. (2008). Formation of continental flood volcanism—The perspective of setting of melting. *Lithos*, *100*(1–4), 49–65. https://doi.org/10.1016/j.lithos.2007.06.015

Gaschnig, R. M., Vervoort, J. D., Lewis, R. S., & Tikoff, B. (2011). Isotopic evolution of the Idaho batholith and Challis intrusive province, northern US Cordillera. *Journal of Petrology*, *52*, 2397–2429. https://doi.org/10.1093/petrology/egr050

Graham, D. W., Blichert-Toft, J., Russo, C. J., Rubin, K. H., & Albarède, F. (2006). Cryptic striations in the upper mantle revealed by hafnium isotopes in southeast Indian ridge basalts. *Nature*, *440*, 199–202.

Graham, D. W., Hanan, B. B., Hémond, C., Blichert-Toft, J., & Albarède, F. (2014). Helium isotopic textures in Earth's upper mantle. *Geochemistry, Geophysics, Geosystems*, *15*, 2048–2074. https://doi.org/10.1002/2014GC005264

Graham, D. W., Jenkins, W. J., Schilling, J. G., Thompson, G., Kurz, M. D., & Humphris, S. E. (1992). Helium isotope geochemistry of mid-ocean ridge basalts from the South Atlantic. *Earth and Planetary Science Letters*, *110*, 133–147. https://doi.org/10.1016/0012-821x(92)90044-v

Graubard, M., 2016, Evolution of a flood basalt crustal magmatic system: In situ mineral data and computational modeling of the Steens Basalt [M.S. Thesis]: Central Washington University, 190 p.

Gualda, G. A., Ghiorso, M. S., Lemons, R. V., & Carley, T. L. (2012). Rhyolite-MELTS: A modified calibration of MELTS optimized for silica-rich, fluid-bearing magmatic systems. *Journal of Petrology*, *53*, 875–890. https://doi.org/10.1093/petrology/egr080

Gunn, B. M., & Watkins, N. D. (1970). Geochemistry of the Steens Mountain basalts, Oregon. *Geological Society of America Bulletin*, *81*, 1497–1516. https://doi.org/10.1130/0016-7606(1970)81[1497:gotsmb]2.0.co;2

Hanan, B. B., & Graham, D. W. (1996). Lead and helium isotope evidence from oceanic basalts for a common deep source of mantle plumes. *Science*, *272*, 991–995. https://doi.org/10.1126/science.272.5264.991

Hart, S. R., Gerlach, D. C., & White, W. M. (1986). A possible new Sr-Nd-Pb mantle array and consequences for mantle mixing. *Geochimica et Cosmochimica Acta*, *50*, 1551–1557. https://doi.org/10.1016/0016-7037(86)90329-7

Hart, S. R., Hauri, E. H., Oschmann, L. A., & Whitehead, J. A. (1992). Mantle plumes and entrainment: Isotopic evidence. *Science*, *256*(520), 517. https://doi.org/10.1126/science.256.5056.517

Hart, S. R., & Ravizza, G. E. (1996). Os partitioning between phases in lherzolite and basalt. *American Geophysical Union Monograph*, *95*, 123–144. https://doi.org/10.1029/gm095p0123

Hart, W. K., Carlson, R. W., & Shirey, S. B. (1997). Radiogenic Os in primitive basalts from the northwestern U.S.A.: Implications for petrogenesis. *Earth and Planetary Science Letters*, *150*, 103–116. https://doi.org/10.1016/s0012-821x(97)00075-7

Hauri, E. H. (2002). Osmium isotopes and mantle convection. *Philosophical Transactions of the Royal Society of London A: Mathematical, Physical and Engineering Sciences*, *360*, 2,371–2,382. https://doi.org/10.1098/rsta.2002.1073

Hauri, E. H., Whitehead, J. A., & Hart, S. R. (1994). Fluid dynamic and geochemical aspects of entrainment in mantle plumes. *Journal of Geophysical Research*, *99*, 24,275–24,300. https://doi.org/10.1029/94jb01257

Hawkesworth, C., Kelley, S., Turner, S., le Roex, A., & Storey, B. (1999). Mantle processes during Gondwana break-up and dispersal. *Journal of African Earth Sciences*, *28*(1), 239–261. https://doi.org/10.1016/s0899-5362(99)00026-3

Heinonen, J. S., Luttinen, A. V., & Bohrson, W. A. (2016). Enriched continental flood basalts from depleted mantle melts: Modeling the lithospheric contamination of Karoo lavas from Antarctica. *Contributions to Mineralogy and Petrology*, *171*(9). https://doi.org/10.1007/s00410-015-1214-8

Heinonen, J. S., Luttinen, A. V., Riley, T. R., & Michallik, R. M. (2013). Mixed pyroxenite peridotite sources for mafic and ultramafic dikes from the Antarctic segment of the Karoo continental flood basalt province. *Lithos*, *177*, 366–380. https://doi.org/10.1016/j.lithos.2013.05.015

Helmke, P. A., & Haskin, L. A. (1973). Rare-earth elements, Co, Sc and Hf in the Steens Mountain basalts. *Geochimica et Cosmochimica Acta*, *37*, 1513–1,529. https://doi.org/10.1016/0016-7037(73)90087-2

Higgins, M. D., & Chandrasekharam, D. (2007). Nature of sub-volcanic magma chambers, Deccan Province, India: Evidence from quantitative textural analysis of plagioclase megacrysts in the Giant Plagioclase Basalts. *Journal of Petrology*, *48*, 885–900. https://doi.org/10.1093/petrology/egm005

Hooper, P. R., Camp, V. E., Reidel, S. P., & Ross, M. E. (2007). The origin of the Columbia River flood basalt province: Plume versus nonplume models. In G. R. Foulger, & D. M. Jurdy (Eds.), *Plates, Plumes, and Planetary Processes: Geological Society of America Special Paper* (Vol. 430, pp. 635–668). Boulder, CO: https://doi.org/10.1130/2007.2430(30)

Hooper, P. R., & Hawkesworth, C. J. (1993). Isotopic and geochemical constraints on the origin and evolution of the Columbia River basalt. *Journal of Petrology*, *34*, 1203–1,246. https://doi.org/10.1093/petrology/34.6.1203

Hooper, P. R., Kleck, W. D., Knowles, C. R., Reidel, S. P., & Thiessen, R. L. (1984). Imnaha Basalt, Columbia River Basalt Group. *Journal of Petrology*, *25*, 473–500. https://doi.org/10.1093/petrology/25.2.473

Hooper, P. R., & Swanson, D. A. (1990). The Columbia River Basalt Group and associated volcanic rocks of the Blue Mountains province. *US Geological Survey Professional Paper*, *1,437*, 63–99.

Hopkins, J. L., Timm, C., Millet, M. A., Poirier, A., Wilson, C. J., & Leonard, G. S. (2016). Os isotopic constraints on crustal contamination in Auckland Volcanic Field basalts, New Zealand. *Chemical Geology*, *439*, 83–97. https://doi.org/10.1016/j.chemgeo.2016.06.019

Ingle, S., & Coffin, M. F. (2004). Impact origin for the greater Ontong Java Plateau? *Earth and Planetary Science Letters*, *218*, 123–134. https://doi.org/10.1016/s0012-821x(03)00629-0

Jarboe, N. A., Coe, R. S., Renne, P. R., & Glen, J. M. G. (2010). The age of the Steens reversal and the Columbia River Basalt Group. *Chemical Geology*, *274*(3-4), 158–168. https://doi.org/10.1016/j.chemgeo.2010.04.001

Jarboe, N. A., Coe, R. S., Renne, P. R., Glen, J. M. G., & Mankinen, E. A. (2008). Quickly erupted volcanic sections of the Steens Basalt, Columbia River Basalt Group: Secular variation, tectonic rotation, and the Steens Mountain reversal. *Geochemistry, Geophysics, Geosystems*, *9*(11). https://doi.org/10.1029/2008gc002067

Johnson, J. A., Hawkesworth, C. J., Hooper, P. R., & Binger, G. B. (1998). Major and trace element analyses of Steens Basalt, southeastern Oregon. In *U.S. Geological Survey Open File Report 98-482* (pp. 26). Reston, VA.

Kasbohm, J., & Schoene, B. (2018). Rapid eruption of the Columbia River flood basalt and correlation with the mid-Miocene climate optimum. *Science*, *4*. https://doi.org/10.1126/sciadv.aat8223

Kiseeva, E. S., Fonseca, R. O., & Smythe, D. J. (2017). Chalcophile elements and sulfides in the upper mantle. *Elements*, *13*, 111–116. https://doi.org/10.2113/gselements.13.2.111

Kistler, R. W., & Peterman, Z. E. (1973). Variations in Sr, Rb, K, Na, and initial $^{87}Sr/^{86}Sr$ in Mesozoic granitic rocks and intruded wall rocks in central California. *Geological Society of America Bulletin*, *84*, 3489–3,512. https://doi.org/10.1130/0016-7606(1973)84<3489:visrkn>2.0.co;2

Kurz, G. A., Schmitz, M. D., Northrup, C. J., & Vallier, T. L. (2017). Isotopic compositions of intrusive rocks from the Wallowa and Olds Ferry arc terranes of northeastern Oregon and western Idaho: Implications for Cordilleran evolution, lithospheric structure, and Miocene magmatism. *Lithosphere*, *9*, 235–264. https://doi.org/10.1130/l550.1

Loewen, M. W., & Bindeman, I. N. (2015). Oxygen isotope and trace element evidence for three stage petrogenesis of the youngest episode (260–79 ka) of Yellowstone rhyolitic volcanism. *Contributions to Mineralogy and Petrology*, *170*, 39. https://doi.org/10.1007/s00410-015-1189-5

Luguet, A., Shirey, S. B., Lorand, J. P., Horan, M. F., & Carlson, R. W. (2007). Residual platinum-group minerals from highly depleted harzburgites of the Lherz massif (France) and their role in HSE fractionation of the mantle. *Geochimica et Cosmochimica Acta*, *71*, 3082–3097. https://doi.org/10.1016/j.gca.2007.04.011

Luttinen, A. V., Leat, P. T., & Furnes, H. (2010). Bjornnutane and Sembberget basalt lavas and the geochemical provinciality of Karoo magmatism in western Dronning Maud Land, Antarctica. *Journal of Volcanology and Geothermal Research*, *198*(1–2), 1–18. https://doi.org/10.1016/j.jvolgeores.2010.07.011

Mahood, G. A., & Benson, T. R. (2017). Using $^{40}Ar/^{39}Ar$ ages of intercalated silicic tuffs to date flood basalts: Precise ages for Steens Basalt Member of the Columbia River Basalt Group. *Earth and Planetary Science Letters*, *459*, 340–351. https://doi.org/10.1016/j.epsl.2016.11.038

Martin, C. E., Carlson, R. W., Shirey, S. B., Frey, F. A., & Chen, C. Y. (1994). Os isotopic variation in basalts from Haleakala Volcano, Maui, Hawaii: A record of magmatic processes in oceanic mantle and crust. *Earth and Planetary Science Letters*, *128*, 287–301. https://doi.org/10.1016/0012-821x(94)90151-1

Mavrogenes, J. A., & O'Neill, H. S. C. (1999). The relative effects of pressure, temperature and oxygen fugacity on the solubility of sulfide in mafic magmas. *Geochimica et Cosmochimica Acta*, *63*, 1173–1,180. https://doi.org/10.1016/s0016-7037(98)00289-0

McKenzie, D. (1984). A possible mechanism for epeirogenic uplift. *Nature*, *307*, 616–618. https://doi.org/10.1038/307616a0

Melluso, L., Mahoney, J. J., & Dallai, L. (2006). Mantle sources and crustal input as recorded in high-Mg Deccan Traps basalts of Gujarat (India). *Lithos*, *89*, 259–274. https://doi.org/10.1016/j.lithos.2005.12.007

Moore, N. E. (2018). *Petrogenesis of the Steens Basalt: Variation in source contributions and effects of crustal passage during the onset of Columbia river flood basalt volcanism [Ph.D. Dissertation]*. Corvallis, OR: Oregon State University. https://ir.library.oregonstate.edu/concern/graduate_thesis_or_dissertations/jq085r45v

Moore, N. E., Grunder, A. L., & Bohrson, W. A. (2018). The three-stage petrochemical evolution of the Steens Basalt compared to large igneous provinces and layered mafic intrusions. *Geosphere*, *14*(6), 2505–2,532. https://doi.org/10.1130/GES01665.1

Moore, N., Grunder, A., Bohrson, W., Carlson, R., & Bindeman, I. (2020). *Steens Basalt Sr, Nd, Pb, Hf, Os, and O Isotopic Compositional Data, Version 1.0. Interdisciplinary Earth Data Alliance (IEDA)*. https://doi.org/10.1594/IEDA/111473. Accessed 2020-07-20.

Mungall, J. E., & Brenan, J. M. (2014). Partitioning of platinum-group elements and Au between sulfide liquid and basalt and the origins of mantle–crust fractionation of the chalcophile elements. *Geochimica et Cosmochimica Acta*, *125*, 265–289. https://doi.org/10.1016/j.gca.2013.10.002

Nelson, D. O. (1983). Implications of oxygen-isotope data and trace-element modeling for a large- scale mixing model for the Columbia River Basalt. *Geology*, *11*, 248–251. https://doi.org/10.1130/0091-7613(1983)11<248:ioodat>2.0.co;2

Pagé, P., & Barnes, S. J. (2016). The influence of chromite on osmium, iridium, ruthenium and rhodium distribution during early magmatic processes. *Chemical Geology*, *420*, 51–68. https://doi.org/10.1016/j.chemgeo.2015.11.002

Pertermann, M., & Hirschmann, M. M. (2003). Partial melting experiments on a MORB like pyroxenite between 2 and 3 GPa: Constraints on the presence of pyroxenite in basalt source regions from solidus location and melting rate. *Journal of Geophysical Research*, *108*, 2125. https://doi.org/10.1029/2000JB000118

Pierce, K. L., & Morgan, L. A. (2009). Is the track of the Yellowstone hotspot driven by a deep mantle plume?—Review of volcanism, faulting, and uplift in light of new data. *Journal of Volcanology and Geothermal Research*, *188*, 1–25. https://doi.org/10.1016/j.jvolgeores.2009.07.009

Potter, K. E., Shervais, J. W., Christiansen, E. H., & Vetter, S. K. (2018). Evidence for cyclical fractional crystallization, recharge, and assimilation in basalts of the Kimama drill core, central Snake River Plain, Idaho: 5.5- Million-Years of petrogenesis in a mid-crustal sill complex. *Frontiers in Earth Science*, *16*. https://doi.org/10.3389/feart.2018.00010

Rajamani, V., & Naldrett, A. J. (1978). Partitioning of Fe, Co, Ni, and Cu between sulfide liquid and basaltic melts and the composition of Ni-Cu Sulfide Deposits. *Economic Geology*, *73*, 82–93. https://doi.org/10.2113/gsecongeo.73.1.82

Reidel, S. P., Camp, V. E., Tolan, T. L., & Martin, B. S. (2013). The Columbia River flood basalt province: Stratigraphy, areal extent, volume, and physical volcanology. *Geological Society of America Special Papers*, *497*, 1–43. https://doi.org/10.1130/2013.2497(01)

Reidel, S. P., Fecht, K. R., Hagood, M. C., Tolan, T. L., & Hooper, P. R. (1989). The geologic evolution of the central Columbia Plateau. *Geological Society of America Special Papers*, *239*, 247–264. https://doi.org/10.1130/spe239-p247

Reisberg, L., Zindler, A., Marcantonio, F., White, W., Wyman, D., & Weaver, B. (1993). Os isotope systematics in ocean island basalts. *Earth and Planetary Science Letters*, *120*, 149–167. https://doi.org/10.1016/0012-821x(93)90236-3

Richards, M. A., Duncan, R. A., & Courtillot, V. E. (1989). Flood basalts and hot-spot tracks: Plume heads and tails. *Science*, *246*, 103–107. https://doi.org/10.1126/science.246.4926.103

Rogers, N. W., Davies, M. K., Parkinson, I. J., & Yirgu, G. (2010). Osmium isotopes and Fe/Mn ratios in Ti-rich picritic basalts from the Ethiopian flood basalt province: No evidence for core contribution to the Afar plume. *Earth and Planetary Science Letters*, *296*, 413–422. https://doi.org/10.1016/j.epsl.2010.05.027

Rooney, T. O., Hanan, B. B., Graham, D. W., Furman, T., Blichert-Toft, J., & Schilling, J. G. (2012). Upper mantle pollution during Afar plume–continental rift interaction. *Journal of Petrology*, *53*, 365–389. https://doi.org/10.1093/petrology/egr065

Roy-Barman, M., Wasserburg, G. J., Papanastassiou, D. A., & Chaussidon, M. (1998). Osmium isotopic compositions and Re–Os concentrations in sulfide globules from basaltic glasses. *Earth and Planetary Science Letters*, *154*, 331–347. https://doi.org/10.1016/s0012-821x(97)00180-5

Sattari, P., Brenan, J. M., Horn, I., & McDonough, W. F. (2002). Experimental constraints on the sulfide- and chromite-silicate melt partitioning behavior of rhenium and platinum-group elements. *Economic Geology*, *97*, 385–398. https://doi.org/10.2113/gsecongeo.97.2.385

Shervais, J. W., Vetter, S. K., & Hanan, B. B. (2006). Layered mafic sill complex beneath the eastern Snake River Plain: Evidence from cyclic geochemical variations in basalt. *Geology*, *34*, 365–368. https://doi.org/10.1130/G22226.1

Sheth, H. (2016). Giant plagioclase basalts, Continental flood basalt–induced remobilization of anorthositic mushes in a deep crustal sill complex. *Geological Society of America Bulletin*, *128*, 916–925. https://doi.org/10.1130/b31404.1

Shirey, S. B., & Walker, R. J. (1998). The Re-Os isotope system in cosmochemistry and high temperature geochemistry. *Annual Review of Earth and Planetary Sciences*, *26*, 423–500. https://doi.org/10.1146/annurev.earth.26.1.423

Spera, F. J., & Bohrson, W. A. (2001). Energy-constrained open-system magmatic processes I: general model and energy-constrained assimilation–fractional crystallization (EC-AFC) formulation. *Journal of Petrology*, *42*, 999–1,018. https://doi.org/10.1093/petrology/42.5

Stracke, A., Bizimis, M., & Salters, V. J. (2003). Recycling oceanic crust: Quantitative constraints. *Geochemistry, Geophysics, Geosystems*, *4*, 8003. https://doi.org/10.1029/2001gc000223

Stracke, A., Hofmann, A. W., & Hart, S. R. (2005). FOZO, HIMU, and the rest of the mantle zoo. *Geochemistry, Geophysics, Geosystems*, *6*, Q05007. https://doi.org/10.1029/2004GC000824

Sun, S. S., & McDonough, W. S. (1989). Chemical and isotopic systematics of oceanic basalts: implications for mantle composition and processes. In A. D. Saunders, & M. J. Norry (Eds.), *Magmatism in the Ocean Basins* (Vol. 42, pp. 313–345). London, UK: Geological Society of London Special Publications.

Takahahshi, E., Nakajima, K., & Wright, T. L. (1998). Origin of the Columbia River basalts: Melting model of a heterogeneous plume head. *Earth and Planetary Science Letters*, *162*(1), 63–80. https://doi.org/10.1016/s0012-821x(98)00157-5

Tanaka, T., Togashi, S., Kamioka, H., Amakawa, H., Kagami, H., Hamamoto, T., et al. (2000). JNdi1: A neodymium isotopic reference in consistency with LaJolla neodymium. *Chemical Geology*, *168*, 279–281. https://doi.org/10.1016/s0009-2541(00)00198-4

Thompson, R., Morrison, M., Dickin, A., & Hendry, G. (1983). *Continental flood basalts... arachnids rule OK?: Continental basalts and mantle xenoliths* (pp. 158–185). New York, NY: Birkhäuser.

Todt, W., Cliff, R. A., Hanser, A., & Hofmann, A. W. (1996). Evaluation of a ^{202}Pb–^{205}Pb double spike for high precision lead isotope analysis. In S. R. Hart, & A. Basu (Eds.), *Earth Processes: Reading the Isotope Code*, *Geophysical Monograph 95* (pp. 429–437). Washington, DC: AGU.

Toth, C. (2018). *Giant plagioclase in the Steens Basalt, SE Oregon: Cumulate entrainment revealed by textural and in situ chemical analysis [M.S. Thesis]* (pp. 105), Ellensburg, WA: Central Washington University.

Turner, S., Hawkesworth, C., Gallagher, K., Stewart, K., Peate, D., & Mantovani, M. (1996). Mantle plumes, flood basalts, and thermal models for melt generation beneath continents: Assessment of a conductive heating model and application to the Parana. *Journal of Geophysical Research*, *101*(B5), 11,503–11,518. https://doi.org/10.1029/96jb00430

Vye-Brown, C., Gannoun, A., Barry, T. L., Self, S., & Burton, K. W. (2013). Osmium isotope variations accompanying the eruption of a single lava flow field in the Columbia River Flood Basalt Province. *Earth and Planetary Science Letters*, *368*, 183–194. https://doi.org/10.1016/j.epsl.2013.02.003

Walker, G. W., MacLeod, N. S., Russell, D., & Earnest, P. (1991). Geologic map of Oregon. In *US Geological Survey*. Reston, VA.

White, R., & McKenzie, D. (1989). Magmatism at rift zones: the generation of volcanic continental margins and flood basalts. *Journal of Geophysical Research*, *94*, 7685–7729. https://doi.org/10.1029/jb094ib06p07685

Wierman, C.T., 2018, Copper partitioning in mid-Miocene flood basalts from the Northern Great Basin (U.S.A): Implications for Cu behavior in flood basalt provinces [Master's thesis] Kansas State University, 134 pp.
Wolff, J. A., & Ramos, F. C. (2013). Source materials for the main phase of the Columbia River Basalt Group: Geochemical evidence and implications for magma storage and transport. *Geological Society of America Special Papers*, *497*, 273–291.https://doi-org.ccl.idm.oclc.org/10.1130/SPE497
Wolff, J. A., Ramos, F. C., Hart, G. L., Patterson, J. D., & Brandon, A. D. (2008). Columbia River flood basalts from a centralized crustal magmatic system. *Nature Geoscience*, *1*(3), 177–180. https://doi.org/10.1038/ngeo124
Workman, R. K., & Hart, S. R. (2005). Major and trace element composition of the depleted MORB mantle (DMM). *Earth and Planetary Science Letters*, *231*, 53–72. https://doi.org/10.1016/j.epsl.2004.12.005
Wright, T. L., Grolier, M. J., & Swanson, D. A. (1973). Chemical variation related to the stratigraphy of the Columbia River basalt. *Geological Society of America Bulletin*, *84*, 371–386. https://doi.org/10.1130/0016-7606(1973)84<371:cvrtts>2.0.co;2
Zindler, A., & Hart, S. (1986). Chemical geodynamics. *Annual Review of Earth and Planetary Sciences*, *14*, 493–571. https://doi.org/10.1146/annurev.ea.14.050186.002425

References From the Supporting Information

Abzalov, M. Z., & Both, R. A. (1997). The Pechenga Ni-Cu deposits, Russia: Data on PGE and Au distribution and sulfur isotope composition. *Mineralogy and Petrology*, *61*, 119–143. https://doi.org/10.1007/bf01172480
Aldanmaz, E., Pickard, M., Meisel, T., Altunkaynak, S., Sayit, K., Sen, P., Hanan, B. B., & Furman, T. (2015). Source components and magmatic processes in the genesis of Miocene to Quaternary lavas in western Turkey: Constraints from HSE distribution and Hf-Pb-Os isotopes. *Contributions to Mineralogy and Petrology*, *170*, 1–20. https://doi.org/10.1007/S00410-015-1,176-X
Araujo, A. L. N., Carlson, R. W., Gaspar, J. C., & Bizzi, L. A. (2001). Petrology of kamafugites and kimberlites from the Alto Paranaiba alkaline province, Minas Gerais, Brazil. *Contributions to Mineralogy and Petrology*, *142*, 163–177. https://doi.org/10.1007/s004100100280
Arguin, P., Page, P., Barnes, S., Yu, S., & Song, X. (2016). The effect of chromite crystallization on the distribution of osmium, iridium, ruthenium and rhodium in picritic magmas: An example from the Emeishan Large Igneous Province, Southwestern China. *Journal of Petrology*, *57*, 1019, Georem-Id: 10082–1,048. https://doi.org/10.1093/Petrology/Egw033
Bennett, V. C., Esat, T. M., & Norman, M. D. (1996). Two mantle-plume components in Hawaiian picrites inferred from correlated Os-Pb isotopes. *Nature*, *381*, 221–223. https://doi.org/10.1038/381221a0
Bennett, V. C., Norman, M. D., & Garcia, M. O. (2000). Rhenium and platinum group element abundances correlated with mantle source components in Hawaiian picrites: Sulphides in the plume. *Earth Planetary Science Letters*, *183*, 513–521. https://doi.org/10.1016/s0012-821x(00)00295-8
Bizzi, L. A., De Wit, M. J., Smith, C. B., McDonald, I., & Armstrong, R. A. (1995). Heterogeneous enriched mantle materials and DUPAL-type magmatism along the SW margin of the Sao Francisco craton, Brazil. *Journal of Geodynamics*, *20*, 469–491. https://doi.org/10.1016/0264-3,707(95)00028-8
Blondes, M. S., Reiners, P. W., Ducea, M. N., Singer, B. S., & Chesley, J. T. (2008). Temporal-compositional trends over short and long time-scales in basalts of the Big Pine volcanic field, California. *Earth Planetary Science Letters*, *269*, 140, georem-id: 4024–154. https://doi.org/10.1016/j.epsl.2008.02.012
Blusztajn, J., & Hegner, E. (2002). Osmium isotopic systematics of melilitites from the Tertiary central European volcanic province in SW Germany. *Chemical Geology*, *189*, 91, georem-id: 1181–103. https://doi.org/10.1016/s0009-2,541(02)00143-2
Brandon, A. D., Graham, D. W., Waight, T., & Gautason, B. (2007). ^{186}Os and ^{187}Os enrichments and high-^{3}He/^{4}He sources in the Earth's mantle: Evidence from Icelandic picrites. *Geochimica et Cosmochimica Acta*, *71*, 4570, georem-id: 3182–4,591. https://doi.org/10.1016/j.gca.2007.07.015
Brügmann, G. E., Hanski, E. J., Naldrett, A. J., & Smolokin, V. F. (2000). Sulphide segregation in ferropicrites from the Pechenga Complex, Kola Peninsula, Russia. *Journal of Petrology*, *41*, 1721–1742. https://doi.org/10.1093/petrology/41.12.1721
Callegaro, S., Marzoli, A., Bertrand, H., Chiaradia, M., Reisberg, L., Meyzen, C. M., Bellieni, G., Weems, R. E., & Merle, R. E. (2013). Upper and lower crust recycling in the source of camp basaltic dykes from southeastern North America. *Earth and Planetary Science Letters*, *376*, 186–199. https://doi.org/10.1016/j.epsl.2013.06.023
Callegaro, S., Rapaille, C., Marzoli, A., Bertrand, H., Chiaradia, M., Reisberg, L., Bellieni, G., Martins, L., Madeira, J., Mata, J., Youbi, N., De Min, A., Azevedo, M. R., & Bensalah, M. K. (2014). Enriched mantle source for the central Atlantic magmatic province: new supporting evidence from southwestern Europe. *Lithos*, *188*, 15–32. https://doi.org/10.1016/j.lithos.2013.10.021
Carlson, R. W., Czamanske, G. K., Fedorenko, V. A., & Ilupin, I. P. (2006). A comparison of Siberian meimechites and kimberlites: implications for the source of high-Mg alkalic magmas and flood basalts. *Geochemistry Geophysics Geosystems*, *7*, georem-id: 2429. https://doi.org/10.1029/2006gc001342
Carlson, R. W., de Araujo, A. L. N., Junqueira-Brod, T. C., Gaspar, J. C., Brod, J. A., Petrinovic, I. A., de Hollanda, M. H. B. M., Pimentel, M. M., & Sichel, S. E. (2007). Chemical and isotopic relationships between peridotite xenoliths and mafic-ultrapotassic rocks from southern Brazil. *Chemical Geology*, *242*, 415–437. https://doi.org/10.1016/j.chemgeo.2007.04.009
Carlson, R. W., Esperança, S., & Svisero, D. P. (1996). Chemical and Os isotopic study of Cretaceous potassic rocks from southern Brazil. *Contributions to Mineralogy Petrology*, *125*, 393–405. https://doi.org/10.1007/s004100050230
Carlson, R. W., Grove, T. L., & Donnelly-Nolan, J. M. (2018). Origin of primitive tholeiitic and calc-alkaline basalts at Newberry Volcano, Oregon. *Geochemistry Geophysics Geosystems*, *19*, 1,360–1,377. https://doi.org/10.1029/2018GC007454
Chen, S., Fan, W., Shi, R., Liu, X., & Zhou, X. (2018). 118–115 Ma magmatism in the Tethyan Himalaya igneous province: Constraints on Early Cretaceous rifting of the northern margin of greater India. *Earth Planetary Science Letters*, *491*, 21–33. https://doi.org/10.1016/j.epsl.2018.03.034
Chesley, J. T., Ruiz, J., Righter, K., Ferrari, L., & Gomez-Tuena, A. (2002). Source contamination versus assimilation: an example from the trans-Mexican volcanic arc. *Earth Planetary Science Letters*, *195*, 211–221. https://doi.org/10.1016/s0012-821x(01)00580-5
Chu, Z., Harvey, J., Liu, C., Guo, J., Wu, F., Tian, W., Zhang, Y., & Yang, Y. (2013). Source of highly potassic basalts in northeast China: Evidence from Re-Os, Sr-Nd-Hf isotopes and PGE geochemistry. *Chemical Geology*, *52–66*, GeoReM-id: 7646. https://doi.org/10.1016/j.chemgeo.2013.08.007
Chu, Z., Yan, Y., Zeng, G., Tian, W., Li, C., Yang, Y., & Guo, J. (2017). Petrogenesis of Cenozoic basalts in central-eastern China: Constraints from Re-Os and PGE geochemistry. *Lithos*, *278–281*, 72, GeoReM-id: 10632–83. https://doi.org/10.1016/j.lithos.2017.01.022

Connolly, B. D., Puchtel, I. S., Walker, R. J., Arevalo, R. Jr., Piccoli, P. M., Byerly, G. R., Robin-Popieul, C., & Arndt, N. T. (2011). Highly siderophile element systematics of the 3.3 Ga Weltevreden komatiites, South Africa: Implications for early Earth history. *Earth Planetary Science Letters*, *311*, 253, georem-id: 5990–263. https://doi.org/10.1016/j.epsl.2011.09.039

Conticelli, S., Carlson, R. W., Widom, E., & Serri, G. (2007). Chemical and isotopic composition (Os, Pb, Nd, and Sr) of Neogene to Quaternary calc-alkalic, shoshonitic, and ultrapotassic mafic rocks from the Italian Peninsula: Inferences on the nature of their mantle sources. *Geological Society of America, Special Paper*, *418*, 171–202. https://doi.org/10.1130/2007.2418(09)

Crocket, J. H. (2000). PGE in fresh basalt, hydrothermal alteration products, and volcanic incrustations of Kilauea volcano, Hawaii. *Geochimica et Cosmochimica Acta*, *64*, 1791–1807. https://doi.org/10.1016/s0016-7,037(00)00340-9

Crocket, J. H. (2002). Platinum-group elements in basalts from Maui, Hawaii: Low abundances in alkali basalts. *Canadian Mineralogist*, *40*, 595–609. https://doi.org/10.2113/gscanmin.40.2.595

Dale, C. W., Kruijer, T. S., & Burton, K. W. (2016). Highly siderophile element and 182w evidence for a partial late veneer in the source of 3.8 Ga rocks from Isua, Greenland. *Earth Planetary Science Letters*, *458*, 394, GeoReM-id: 10773–404. https://doi.org/10.1016/j.epsl.2016.11.001

Dale, C. W., Kruijer, T. S., & Burton, K. W. (2017). Highly siderophile element and 182 W evidence for a partial late veneer in the source of 3.8 Ga rocks from Isua, Greenland. *Earth Planetary Science Letters*, *458*, 394, GeoReM-id: 10773–404. https://doi.org/10.1016/j.epsl.2016.11.001

Dale, C. W., MacPherson, C. G., Pearson, D. G., Hammond, S. J., & Arculus, R. J. (2012). Inter-element fractionation of highly siderophile elements in the Tonga Arc due to flux melting of a depleted source. *Geochimica et Cosmochimica Acta*, *89*, 202, georem-id: 6887–225. https://doi.org/10.1016/j.gca.2012.03.025

Dale, C. W., Yu, M. A., Macpherson, C. G., Pearson, D. G., & Hickey-Vargas, R. (2008). Extreme platinum-group element fractionation and variable Os isotope compositions in Philippine Sea Plate basalts: Tracing mantle source heterogeneity. *Chemical Geology*, *248*, 213, GeoReM-id: 3745–238. https://doi.org/10.1016/j.chemgeo.2007.11.007

Day, J. M. D., Harvey, R. P., & Hilton, D. R. (2019). Melt-modified lithosphere beneath Ross Island and its role in the tectono-magmatic evolution of the West Antarctic rift system. *Chemical Geology*, *518*, 45–54. https://doi.org/10.1016/j.chemgeo.2019.04.012

Day, J. M. D., Pearson, D. G., & Hulbert, L. J. (2008). Rhenium-osmium isotope and platinum-group element constraints on the origin and evolution of the 1.27 Ga Muskox Layered Intrusion. *Journal of Petrology*, *49*, 1255, GeoReM-id: 4072–1,295. https://doi.org/10.1093/petrology/egn024

Day, J. M. D., Pearson, D. G., & Hulbert, L. J. (2013). Highly siderophile element behavior during flood basalt genesis and evidence for melts from intrusive chromitite formation in the Mackenzie Large Igneous Province. *Lithos*, *182–183*, 242, GeoReM-id: 7368–258. https://doi.org/10.1016/j.lithos.2013.10.011

Day, J. M. D., Pearson, D. G., Macpherson, C. G., Lowry, D., & Carracedo, J. C. (2010). Evidence for distinct proportions of subducted oceanic crust and lithosphere in Himu-type mantle beneath El Hierro and La Palma, Canary Islands. *Geochimica et Cosmochimica Acta*, *74*, 6565, georem-id: 5600–6,589. https://doi.org/10.1016/j.gca.2010.08.021

Dowling, S. E., & Hill, R. E. T. (1992). The distribution of PGE in fractionated Archaean komatiites, western and central ultramafic units, Mt. Keith region, western Australia. *Australian Journal of Earth Sciences*, *39*, 349–363. https://doi.org/10.1080/08120099208728029

Dreher, S. T., Macpherson, C. G., Pearson, D. G., & Davidson, J. P. (2005). Re-Os isotope studies of Mindanao adakites: Implications for sources of metals and melts. *Geology*, *33*, 957–960. https://doi.org/10.1130/G21755.1

Drignon, M. J., Nielsen, R. L., Tepley, F. J. III, & Bodnar, R. J. (2018). Upper mantle origin of plagioclase megacrysts from plagioclase-ultraphyric mid-oceanic ridge basalt. *Geology*, *47*, 43–46. https://doi.org/10.1130/g45542.1

Eisele, J., Sharma, M., Galer, S. J. G., Blichert-Toft, J., Devey, C. W., & Hofmann, A. W. (2002). The role of sediment recycling in EM-1 inferred from Os, Pb, Hf, Nd, Sr isotope and trace element systematics of the Pitcairn hotspot. *Earth and Planetary Science Letters*, *196*, 197–212. https://doi.org/10.1016/s0012-821x(01)00601-x

Escrig, S., Doucelance, R., Moreira, M. A., & Allegre, C.-J. (2005). Os isotope systematics in Fogo Island: evidence for lower continental crust fragments under the Cape Verde southern islands. *Chemical Geology*, *219*, 93–113. https://doi.org/10.1016/j.chemgeo.2005.02.011

Francis, D. M. (1993). Chemical interaction between picritic magmas and upper crust along the margins of the Muskok Intrusion, Northwest Territories. In , *Canadian Geological Survey Special Paper* (Vol. 92–12, pp. 94). Ottowa, ON, Canada.

Frank, E. A., Maier, W. D., & Mojzsis, S. J. (2016). Highly siderophile element abundances in Eoarchean komatiite and basalt protoliths. *Contributions to Mineralogy and Petrology*, *171*(29). https://doi.org/10.1007/s00410-016-1,243-y

Gangopadhyay, A., Sproule, R. A., Walker, R. J., & Lesher, C. M. (2005). Re-Os systematics of komatiites and komatiitic basalts at Dundonald Beach, Ontario, Canada: Evidence for a complex alteration history and implications of a late-Archean chondritic mantle source. *Geochimica et Cosmochimica Acta*, *69*, 5087–5,098. https://doi.org/10.1016/j.gca.2005.04.021

Gangopadhyay, A., & Walker, R. J. (2003). Re-Os systematics of the 2.7-ga komatiite from Alexo, Ontario, Canada. *Chemical Geology*, *196*, 147–162. https://doi.org/10.1016/S0009-2541(02)00411-4

Gangopadhyay, A., Walker, R. J., Hanski, E. J., & Solheid, A. (2006). Origin of Paleoproterozoic komatiites at Jeesiörova, Kittilä greenstone complex, Finnish Lapland. *Journal of Petrology*, *47*, 773–789. https://doi.org/10.1093/petrology/egi093

Gao, R., Lassiter, J. C., & Ramirez, G. (2017). Origin of temporal compositional trends in monogenetic vent eruptions: Insights from the crystal cargo in the Papoose Canyon sequence, Big Pine Volcanic Field, CA. *Earth Planetary Science Letters*, *457*, 227, GeoReM-id: 10750–237. https://doi.org/10.1016/j.epsl.2016.10.013

Gao, S., Rudnick, R. L., Xu, W., Yuan, H., Liu, Y., Walker, R. J., Puchtel, I. S., Liu, X., Huang, H., Wang, X., & Yang, J. (2008). Recycling deep cratonic lithosphere and generation of intraplate magmatism in the north China craton. *Earth Planetary Science Letters*, *270*, 41, georem-id: 4029–53. https://doi.org/10.1016/j.epsl.2008.03.008

Godel, B. M., Barnes, S.-J., & Sarah-Jane, B. (2013). Deposition mechanisms of magmatic sulphide liquids: Evidence from high-resolution X-ray computed tomography and trace element chemistry of komatiite-hosted disseminated. *Journal of Petrology*, *54*, 1455–1,481. https://doi.org/10.1093/petrology/egt018

Graham, S., Lambert, D. D., & Shee, S. R. (2004). The petrogenesis of carbonatite, melnoite and kimberlite from the eastern Goldfields province, Yilgarn Craton. *Lithos*, *76*, 519–533. https://doi.org/10.1016/j.lithos.2004.03.031

Graham, S., Lambert, D. D., Shee, S. R., Smith, C. B., & Hamilton, R. (1999). Re-Os and Sm-Nd isotopic constraints on the sources of kimberlites and melnoites, Earaheedy Basin, western Australia. In J. J. Gurney, J. L. Gurney, M. D. Pascoe, & S. H. Richardson (Eds.), *Proceedings of the VIIth International Kimberlite Conference* (Vol. 1, pp. 280–290). Cape Town: Red Roof Design.

Hanski, E. J. (1992). Petrology of the Pechanga ferropicrites and cogenetic, Ni-bearing gabbro-wehrlite intrusions, Kola Peninsula, Russia. *Bulletin of the Geological Survey of Finland*, *367*, 1–193.

Hanski, E. J., Walker, R. J., Huhma, H., Polyakov, G. V., Balykin, P. A., Hoa, T. T., & Phuong, N. T. (2004). Origin of the Permian–Triassic komatiites, northwestern Vietnam. *Contributions to Mineralogy and Petrology*, *147*, 453–469. https://doi.org/10.1007/s00410-004-0567-1

Hanyu, T., Tejada, M. L. G., Shimizu, K., Ishizuka, O., Fujii, T., Kimura, J.-I., Chang, Q., Senda, R., Miyazaki, T., Hirahara, Y., Vaglarov, B. S., Goto, K. T., & Ishikawa, A. (2017). Collision-induced post-plateau volcanism: Evidence from a seamount on Ontong Java Plateau. *Lithos*, *294–295*, 87, GeoReM-id: 10693–96. https://doi.org/10.1016/j.lithos.2017.09.029

Hart, S. R., & Ravizza, G. E. (1996). Os partitioning between phases in lherzolite and basalt. In A. Basu, & S. R. Hart (Eds.), *Earth Processes, Reading the Isotopic Code*: Geophysical Monograph (Vol. 95, pp. 123–134). Washington, DC: AGU. https://doi.org/10.1029/gm095p0123

Hauri, E. H., & Kurz, M. D. (1997). Melt migration and mantle chromatography, 2: A time-series Os isotope study of Mauna Loa volcano, Hawaii. *Earth Planetary Science Letters*, *153*, 21–36. https://doi.org/10.1016/s0012-821x(97)00158-1

Hauri, E. H., Lassiter, J. C., & DePaolo, D. J. (1996). Osmium isotope systematics of drilled lavas from Mauna Loa, Hawaii. *Journal of Geophysical Research*, *101*(B5), 11,793–11,806. https://doi.org/10.1029/95jb03346

Hayes, B., Bedard, J. H., Hryciuk, M., Wing, B. A., Nabelek, P. I., MacDonald, W. G., & Lissenberg, C. J. (2015). Sulfide immiscibility induced by wall-rock assimilation in a fault-guided basaltic feeder system, Franklin Large Igneous Province, Victoria Island (Arctic Canada). *Economic Geology*, *110*, 1697–1717. https://doi.org/10.2113/econgeo.110.7.1697

Heinonen, J. S., Carlson, R. W., & Luttinen, A. V. (2010). Isotopic (Sr, Nd, Pb, and Os) composition of highly magnesian dikes of Vestfjella, western Dronning Maud Land, Antarctica: A key to the origins of the Jurassic Karoo large igneous province? *Chemical Geology*, *277*, 227, georem-id: 5200–244. https://doi.org/10.1016/j.chemgeo.2010.08.004

Hopkins, J. L., Timm, C., Millet, M.-A., Poirier, A., Wilson, C. J. N., & Leonard, G. S. (2016). Os isotopic constraints on crustal contamination in Auckland volcanic field basalts, New Zealand. *Chemical Geology*, *439*, 83, GeoReM-id: 9204–97. https://doi.org/10.1016/j.chemgeo.2016.06.019

Hou, T., Zhang, Z., Encarnacion, J. P., Santosh, M., & Sun, Y. (2013). The role of recycled oceanic crust in magmatism and metallogeny: Os-Sr-Nd isotopes, U–Pb geochronology and geochemistry of picritic dykes in the Panzhihua giant Fe-Ti oxide deposit, central Emeishan large igneous province, SW China. *Contributions to Mineralogy and Petrology*, *165*, 805–822. https://doi.org/10.1007/s00410-012-0836-3

Huang, F., Chen, J., Xu, J., Wang, B., & Li, J. (2015). Os-Nd-Sr isotopes in Miocene ultrapotassic rocks of southern Tibet: Partial melting of a pyroxenite-bearing lithospheric mantle? *Geochimica et Cosmochimica Acta*, *163*, 279–298. https://doi.org/10.1016/j.gca.2015.04.053

Hughes, H. S. R., McDonald, I., Faithfull, J. W., Upton, B. G. J., & Loocke, M. (2016). Cobalt and precious metals in sulphides of peridotite xenoliths and inferences concerning their distribution according to geodynamic environment: A case study from the Scottish lithospheric mantle. *Lithos*, *240–243*, 202, GeoReM-id: 9794–227. https://doi.org/10.1016/j.lithos.2015.11.007

Hughes, H. S. R., McDonald, I., Goodenough, K. M., Ciborowski, T. J. R., Kerr, A. C., Davies, J. H. F. L., & Selby, D. (2014). Enriched lithospheric mantle keel below the Scottish margin of the North Atlantic craton: Evidence from the Paleoproterozoic Scourie dyke swarm and mantle xenoliths. *Precambrian Research*, *250*, 97, GeoReM-id: 8270–126. https://doi.org/10.1016/j.precamres.2014.05.026

Hughes, H. S. R., McDonald, I., & Kerr, A. C. (2015). Platinum-group element signatures in the North Atlantic igneous province: Implications for mantle controls on metal budgets during continental breakup. *Lithos*, *233*, 89, GeoReM-id: 8910–110. https://doi.org/10.1016/j.lithos.2015.05.005

Izokh, A. E., Ya, M. A., Fedoseev, G. S., Polyakov, G. V., & Nikolaeva, I. V. (2016). Distribution of PGE in Permo-Triassic basalts of the Siberian large igneous province. *Russian Geology and Geophysics*, *57*, 809–821. https://doi.org/10.1016/j.rgg.2016.04.005

Jackson, M. G., Hart, S. R., Saal, A. E., Shimizu, N., Kurz, M. D., Blusztajn, J., & Skovgaard, A. C. (2008). Globally elevated titanium, tantalum, and niobium (titan) in ocean island basalts with high $^{3}He/^{4}He$. *Geochemistry Geophysics Geosystems*, *9*. https://doi.org/10.1029/2007GC001876

Jamais, M., Lassiter, J. C., & Brügmann, G. (2008). PGE and Os-isotopic variations in lavas from Kohala Volcano, Hawaii: Constraints on PGE behavior and melt/crust interaction. *Chemical Geology*, *250*, 16–28. https://doi.org/10.1016/j.chemgeo.2008.01.028

Larrea, P., Gale, C., Ubide, T., Widom, E., Lago, M., & Franca, Z. T. M. (2014). Magmatic evolution of Graciosa (Azores, Portugal). *Journal of Petrology*, *55*, 2125, GeoReM-id: 7877–2,154. https://doi.org/10.1093/petrology/egu052

Larrea, P., Widom, E., Siebe, C., Salinas, S., & Kuentz, D. (2019). A re-interpretation of the petrogenesis of Paricutin Volcano: Distinguishing crustal contamination from mantle heterogeneity. *Chemical Geology*, *504*, 66–82. https://doi.org/10.1016/j.chemgeo.2018.10.026

Larsen, L. M., Pedersen, A. K., Sundvoll, B., & Frei, R. (2003). Alkali picrites formed by melting of old metasomatized lithospheric mantle: Manitdlat Member, Vaigat Formation, Paleocene of west Greenland. *Journal of Petrology*, *43*, 3–38. https://doi.org/10.1093/petrology/44.1.3

Lassiter, J. C. (2003). Rhenium volatility in subaerial lavas: Constraints from subaerial and submarine portions of the HSDP-2 Mauna Loa Drillcore. *Earth and Planetary Science Letters*, *214*, 311–325. https://doi.org/10.1016/s0012-821x(03)00385-6

Lassiter, J. C., Blichert-Toft, J., Hauri, E. H., & Barsczus, H. G. (2004). Isotope and trace element variations in lavas from Raivavae and Rapa, Cook-Austral Islands: Constraints on the nature of Himu- and EM-mantle and the origin of mid-plate volcanism in French Polynesia. *Chemical Geology*, *202*, 115–138. https://doi.org/10.1016/j.chemgeo.2003.08.002

Li, C., Tao, Y., Qi, L., & Ripley, E. M. (2012). Controls on PGE fractionation in the Emeishan picrites and basalts: Constraints from integrated lithophile-siderophile elements and Sr-Nd isotopes. *Geochimica et Cosmochimica Acta*, *90*, 12–32. https://doi.org/10.1016/j.gca.2012.04.046

Li, J., Wang, X., Ren, Z., Xu, J., Bin, H., & Xu, Y. (2014). Chemical heterogeneity of the Emeishan mantle plume: Evidence from highly siderophile element abundances in picrites. *Journal of Asian Earth Sciences*, *79*, 191–205. https://doi.org/10.1016/j.jseaes.2013.09.009

Li, J., Xu, J., Suzuki, K., He, B., Xu, Y., & Ren, Z. (2010). Os, Nd and Sr isotope and trace element geochemistry of the Muli picrites: Insights into the mantle source of the Emeishan large igneous province. *Lithos*, *119*, 108, georem-id: 5323–122. https://doi.org/10.1016/j.lithos.2010.06.002

Li, X., Li, J., Bader, T., Mo, X., Scheltens, M., Chen, Z., Xu, J., Yu, X., & Huang, X. (2015). Evidence for crustal contamination in intra-continental OIB-like basalts from west Qinling, central China: A Re-Os perspective. *Journal of Asian Earth Sciences*, *98*, 436–445. https://doi.org/10.1016/j.jseaes.2014.10.02.7

Li, Y., Li, Z., Sun, Y., Chen, H., Yang, S., & Yu, X. (2010). PGE and geochemistry of Wajilitag ultramafic cryptoexplosive brecciated rocks from Tarim Basin: Implications for petrogenesis. *Acta Petrologica Sinica (yanshi-xuebao)*, *11*, 3307–3318.

Li, Y., Li, Z., Sun, Y., Santosh, M., Langmuir, C. H., Chen, H., Yang, S., Chen, Z., & Yu, X. (2012). Platinum-group elements and geochemical characteristics of the Permian continental flood basalts in the Tarim Basin, northwest China: Implications for the evolution of the Tarim large igneous province. *Chemical Geology*, *328*, 278, georem-id: 6740–289. https://doi.org/10.1016/j.chemgeo.2012.03.007

Li, Y., Ma, C., Robinson, P. T., Zhou, Q., & Liu, M. (2015). Recycling of oceanic crust from a stagnant slab in the mantle transition zone: Evidence from Cenozoic continental basalts in Zhejiang Province, SE China. *Lithos*, *230*, 146, GeoReM-id: 8853–165. https://doi.org/10.1016/j.lithos.2015.05.021

Liu, D., Zhao, Z., Zhu, D., Niu, Y., Widom, E., Teng, F.-Z., Depaolo, D. J., Ke, S., Ji, X., Wang, Q., & Mo, X. (2015). Identifying mantle carbonatite metasomatism through Os-Sr-Mg isotopes in Tibetan ultrapotassic rocks. *Earth and Planetary Science Letters*, *430*, 458, GeoReM-id: 8654–469. https://doi.org/10.1016/j.epsl.2015.09.005

Lustrino, M., Fedele, L., Melluso, L., Morra, V., Ronga, F., Geldmacher, J., Duggen, S., Agostini, S., Cucciniello, C., Franciosi, L., & Meisel, T. (2013). Origin and evolution of Cenozoic magmatism of Sardinia (Italy): A combined isotopic (Sr-Nd-Pb-O-Hf-Os) and petrological view. *Lithos*, *180–181*, 138, GeoReM-id: 7329–158. https://doi.org/10.1016/j.lithos.2013.08.022

Ma George, S.-K., Malpas, J. G., Nordlie, B. E., Lo, C., Wang, K., Iizuka, Y., & Xenophontos, C. (2013). Evolution and origin of the Miocene intraplate basalts on the Aleppo Plateau, NW Syria. *Chemical Geology*, *335*, 149–171. https://doi.org/10.1016/J.Chemgeo.2012.11.001

Ma George, S.-K., Malpas, J. G., Xenophontos, C., Suzuki, K., & Lo, C. (2011). Early Cretaceous volcanism of the coastal ranges, NW Syria: Magma genesis and regional dynamics. *Lithos*, *126*, 290, Georem-Id: 6335–306. https://doi.org/10.1016/J.Lithos.2011.07.025

Maier, W. D., Barnes, S.-J., & Marsh, J. S. (2003). The concentrations of the noble metals in southern African flood-Type basalts and MORB: Implications for petrogenesis and magmatic sulphide exploration. *Contributions to Mineralogy and Petrology*, *146*, 44, Georem-Id: 411–61. https://doi.org/10.1007/S00410-003-0480-Z

Maier, W. D., O'Brien, H. O., Peltonen, P., & Barnes, S. J. (2017). Platinum-group element contents of Karelian kimberlites: Implications for the PGE Budget of the sub-continental lithospheric mantle. *Geochimica et Cosmochimica Acta*, *216*, 358, Georem-Id: 10452–337. https://doi.org/10.1016/J.Gca.2017.07.002

Maier, W. D., Rasmussen, B., Fletcher, I. R., Godel, B. M., Barnes, S. J., Fisher, L. A., Yang, S., Huhma, H., & Lahaye, Y. (2015). Petrogenesis of the 2·77 Ga Monts de Cristal Complex, Gabon: Evidence for direct precipitation of Pt-arsenides from basaltic magma. *Journal of Petrology*, *56*, 1285, Georem-Id: 8622–1,308. https://doi.org/10.1093/Petrology/Egv035

Maier, W. D., Roelofse, F., & Barnes, S.-J. (2003). The concentration of the platinum-group elements in South African komatiites: Implications for mantle sources, melting regime and PGE fractionation during crystallization. *Journal of Petrology*, *44*, 1787, Georem-Id: 445–1804. https://doi.org/10.1093/Petrology/Egg059

Manikyamba, C., Ray, J., Ganguly, S., Singh, M. R., Santosh, M., Saha, A., & Satyanarayanan, M. (2015). Boninitic metavolcanic rocks and island arc tholeiites from the older metamorphic group (OMG) of Singhbhum Craton, Eastern India: Geochemical evidence for Archean subduction processes. *Precambrian Research*, *271*, 138–159. https://doi.org/10.1016/J.Precamres.2015.09.028

Marcantonio, F., Zindler, A., Elliott, T. R., & Staudigel, H. (1995). Os Isotope systematics of La Palma, Canary Islands: Evidence for recycled crust in the mantle source of Himu ocean island. *Earth and Planetary Science Letters*, *133*, 397–410. https://doi.org/10.1016/0012-821x(95)00092-Q

Marzoli, A., Bertrand, H., Youbi, N., Callegaro, S., Merle, R. E., Reisberg, L., Chiaradia, M., Brownlee, S. I., Jourdan, F., Zanetti, A., Davies, J. H. F. L., Shirahase, T., Mahmoudi, A., Medina, F., Renne, P. R., Bellieni, G., Crivellari, S., El Hachimi, H., Bensalah, M. K., Meyzen, C. M., & Tegner, C. (2019). The Central Atlantic Magmatic Province (CAMP) in Morocco. *Journal Petrology*, *60*, 945–996. https://doi.org/10.1093/Petrology/Egz021

McBride, J. S., Lambert, D. D., Nicholls, I. A., & Price, R. C. (2001). Osmium isotopic evidence for crust–mantle interaction in the genesis of continental intraplate basalts from the Newer Volcanics Province, Southeastern Australia. *Journal Petrology*, *42*, 1197, Georem-Id: 1597–1,218. https://doi.org/10.1093/Petrology/42.6.1197

McDonald, I., De Wit, M. J., Smith, C. B., Bizzi, L. A., & Viljoen, K. S. (1995). The geochemistry of the platinum-group elements in Brazilian and Southern African Kimberlites. *Geochimica et Cosmochimica Acta*, *59*, 2883–2,903. https://doi.org/10.1016/0016-7,037(95)00183-2

Merle, R. E., Marzoli, A., Bertrand, H., Reisberg, L., Verati, C., Zimmermann, C., Chiaradia, M., Bellieni, G., & Ernesto, M. (2011). $^{40}Ar/^{39}Ar$ ages and Sr-Nd-Pb-Os geochemistry of CAMP tholeiites from Western Maranhao Basin (NE Brazil). *Lithos*, *122*, 137–151. https://doi.org/10.1016/J.Lithos.2010.12.010

Merle, R. E., Marzoli, A., Reisberg, L., Bertrand, H., Nemchin, A. A., Chiaradia, M., Callegaro, S., Jourdan, F., Bellieni, G., Kontak, D. J., Puffer, J. H., & McHone, J. G. (2014). Sr, Nd, Pb and Os isotope systematics Of CAMP tholeiites from Eastern North America (Ena): Evidence of a subduction-enriched mantle source. *Journal of Petrology*, *55*, 133–180. https://doi.org/10.1093/Petrology/Egt063

Mincato, R. L. (2000). *Metalogenia dos Elementos do Grupo da Platina com base na Estratigrafia e Geoquímica da Provincia Ígnea Continental do Paraná*. Campinas – SP (pp. 1–172). (Tese de Doutorado, IG-UNICAMP)

Mouri, H., Maier, W. D., & Brandl, G. (2013). on the possible occurrence of komatiites in the Archaean high-grade polymetamorphic central zone of the Limpopo Belt, South Africa. *South African Journal of Geology*, *116*, 55–66. https://doi.org/10.2113/Gssajg.116.1.55

Mukherjee, R., Mondal, S. K., Zhong, H., Bai, Z., Balaram, V., & Ravindra Kumar, G. R. (2014). Platinum-group element geochemistry of komatiite-derived 3.1 Ga ultramafic-mafic rocks and chromitites from The Nuggihalli Greenstone Belt, Western Dharwar Craton (India). *Chemical Geology*, *386*, 190, Georem-Id: 8046–208. https://doi.org/10.1016/J.Chemgeo.2014.08.007

Munteanu, M., Wilson, A. H., Costin, G., Yao, Y., Lum, J. E., Jiang, S., Jourdan, F., Chunnett, G., & Cioaca, M.-E. (2017). The mafic-ultramafic dykes in the Yanbian Terrane (Sichuan province, SW China): Record of magma differentiation and emplacement in the Emeishan Large Igneous Province. *Journal of Petrology*, *58*, 513–538. https://doi.org/10.1093/Petrology/Egx025

Nelson, W. R., Hanan, B. B., Graham, D. W., Shirey, S. B., Yirgu, G., Ayalew, D., & Furman, T. (2019). Distinguishing plume and metasomatized lithospheric mantle contributions to post-flood basalt volcanism on the southeastern Ethiopian Plateau. *Journal of Petrology*, *60*, 1063, Georem-Id: 11853–1,094. https://doi.org/10.1093/Petrology/Egz024

Papunen, H., Halkoaho, T., & Luukkonen, E. (2009). Archean evolution of the Tipasjärvi-Kuhmo-Suomussalmi Greenstone Complex, Finland. *Bulletin of the Geological Survey of Finland*, *403*, 1–68.

Peate, D. W., Baker, J. A., Blichert-Toft, J., Hilton, D. R., Storey, M., Kent, A. J. R., Brooks, C. K., Hansen, H., Pedersen, A. K., & Duncan, R. A. (2003). The Prinsen Af Wales Bjerge Formation lavas, East Greenland: The transition from tholeiitic to alkalic magmatism during Paleogene continental breakup. *Journal of Petrology*, *44*, 279–304. https://doi.org/10.1093/Petrology/44.2.279

Peltonen, P., & Brügmann, G. E. (2006). Origin of layered continental mantle (Karelian Craton, Finland): Geochemical And Re-Os Isotope Constraints. *Lithos*, *89*, 405–423. https://doi.org/10.1016/J.Lithos.2005.12.013

Peters, B. J., & Day, J. M. D. (2017). A geochemical link between plume head and tail volcanism. *Geochemical Perspectives Letters*, *5*, 29–34. https://doi.org/10.7185/Geochemlett.1742

Peters, B. J., Day, J. M. D., Greenwood, R. C., Hilton, D. R., Gibson, J., & Franchi, I. A. (2017). Helium-oxygen-osmium isotopic and elemental constraints on the mantle sources of the Deccan Traps. *Earth and Planetary Science Letters*, *478*, 245–257. https://doi.org/10.1016/J.Epsl.2017.08.042

Peters, B. J., Day, J. M. D., & Taylor, L. A. (2016). Early mantle heterogeneities in the Reunion hotspot source inferred from highly siderophile elements in cumulate xenoliths. *Earth and Planetary Science Letters*, *448*, 150, Georem-Id: 9785–160. https://doi.org/10.1016/J.Epsl.2016.05.015

Puchtel, I. S., Blichert-Toft, J., Touboul, M., Horan, M. F., & Walker, R. J. (2016). The coupled 182 W-142ND record of early terrestrial mantle differentiation. *Geochemistry Geophysics Geosystems*, *17*, 2168, Georem-Id: 9910–2,193. https://doi.org/10.1002/2016gc006324

Puchtel, I. S., Blichert-Toft, J., Touboul, M., & Walker, R. J. (2018). 182 W And HSE Constraints From 2.7 Ga Komatiites on the heterogeneous nature of the Archean mantle. *Geochimica et Cosmochimica Acta*, *228*, 1–26. https://doi.org/10.1016/J.Gca.2018.02.030

Puchtel, I. S., Brandon, A. D., & Humayun, M. (2004). Precise Pt-Re-Os isotope systematics of the mantle from 2.7-Ga Komatiites. *Earth and Planetary Science Letters*, *224*, 157–174. https://doi.org/10.1016/J.Epsl.2004.04.035

Puchtel, I. S., Brandon, A. D., Humayun, M., & Walker, R. J. (2005). Evidence for the early differentiation of the core from Pt-Re-Os isotope systematics of 2.8-Ga komatiites. *Earth and Planetary Science Letters*, *237*, 118–134. https://doi.org/10.1016/J.Epsl.2005.04.023

Puchtel, I. S., & Humayun, M. (2000). Platinum group elements in Kostomuksha komatiites and basalts: Implications for oceanic crust recycling and core–mantle interaction. *Geochimica et Cosmochimica Acta*, *64*, 4227, georem-id: 2034–4,242. https://doi.org/10.1016/S0016-7037(00)00492-0

Puchtel, I. S., & Humayun, M. (2005). Highly siderophile element geochemistry of 187Os-enriched 2.8 Ga Kostomuksha komatiites, Baltic Shield. *Geochimica et Cosmochimica Acta*, *69*, 1,607, Georem-Id: 1837–1,618. https://doi.org/10.1016/J.Gca.2004.09.007

Puchtel, I. S., Humayun, M., Campbell, A. J., Sproule, R. A., & Lesher, C. M. (2004). Platinum group element geochemistry of komatiites from the Alexo and Pyke Hill areas, Ontario, Canada. *Geochimica et Cosmochimica Acta*, *68*, 1361, georem-id: 691–1,383. https://doi.org/10.1016/j.gca.2003.09.013

Puchtel, I. S., Humayun, M., & Walker, R. J. (2007). Os-Pb-Nd isotope and highly siderophile and lithophile trace element systematics of komatiitic rocks from the Volotsk Suite, SE Baltic Shield. *Precambrian Research*, *158*, 119, Georem-Id: 3601–137. https://doi.org/10.1016/J.Precamres.2007.04.004

Puchtel, I. S., Touboul, M., Blichert-Toft, J., Walker, R. J., Brandon, A. D., Nicklas, R. W., Kulikov, V. S., & Samsonov, A. V. (2016). Lithophile and siderophile element systematics of Earth's mantle at the Archean-Proterozoic boundary: Evidence from 2.4 ga komatiites. *Geochimica et Cosmochimica Acta*, *180*, 227, Georem-Id: 9330–255. https://doi.org/10.1016/J.Gca.2016.02.027

Puchtel, I. S., Walker, R. J., Anhaeusser, C. R., & Gruau, G. (2009). Re-Os isotope systematics and HSE abundances of the 3.5 Ga Schapenburg komatiites, South Africa: Hydrous melting or prolonged survival of primordial heterogeneities in the mantle? *Chemical Geology*, *262*, 355–369. https://doi.org/10.1016/J.Chemgeo.2009.02.006

Puchtel, I. S., Walker, R. J., Brandon, A. D., & Nisbet, E. G. (2009). Pt-Re-Os and Sm-Nd isotope and HSE and REE systematics of the 2.7 Ga Belingwe and Abitibi komatiites. *Geochimica et Cosmochimica Acta*, *73*, 6367, Georem-Id: 5231–6,389. https://doi.org/10.1016/J.Gca.2009.07.022

Qi, L., Wang, C. Y., & Zhou, M. (2008). Controls on the PGE distribution of Permian Emeishan alkaline and peralkaline volcanic rocks in Longzhoushan, Sichuan Province, SW China. *Lithos*, *106*, 222, georem-id: 4213–236. https://doi.org/10.1016/j.lithos.2008.07.012

Qi, L., & Zhou, M. (2008). Platinum-group elemental and Sr-Nd-Os isotopic geochemistry of Permian Emeishan flood basalts in Guizhou Province, SW China. *Chemical Geology*, *248*, 83, georem-id: 3726–103. https://doi.org/10.1016/j.chemgeo.2007.11.004

Rankenburg, K., Lassiter, J. C., & Brey, G. P. (2005). The role of continental crust and lithospheric mantle in the genesis of Cameroon volcanic line lavas: Constraints from isotopic variations in lavas and megacrysts from the Biu and Jos plateau. *Journal of Petrology*, *46*, 169–190. https://doi.org/10.1093/petrology/egh067

Rasoazanamparany, C., Widom, E., Siebe, C., Guilbaud, M.-N., Spicuzza, M. J., Valley, J. W., Valdez, G., & Salinas, S. (2016). Temporal and compositional evolution of Jorullo volcano, Mexico: Implications for magmatic processes associated with a monogenetic eruption. *Chemical Geology*, *434*, 62, GeoReM-id: 9213–80. https://doi.org/10.1016/j.chemgeo.2016.04.004

Rasoazanamparany, C., Widom, E., Valentine, G. A., Smith, E. I., Cortes, J. A., Kuentz, D., & Johnsen, R. (2015). Origin of chemical and isotopic heterogeneity in a mafic, monogenetic volcanic field: A case study of the Lunar Crater volcanic field, Nevada. *Chemical Geology*, *397*, 76, GeoReM-id: 8770–93. https://doi.org/10.1016/J.CHEMGEO.2015.01.004

Rhodes, J. M. (1996). Geochemical stratigraphy of lava flows sampled by the Hawaii Scientific Drilling Project. *Journal of Geophysical Research*, *101*(B5), 11,729–11,746. https://doi.org/10.1029/95jb03704

Righter, K., Chesley, J. T., & Ruiz, J. (2002). Genesis of primitive, arc-type basalt: Constraints from Re, Os and Cl on the depth of melting and role of fluids. *Geology*, *30*, 619–622. https://doi.org/10.1130/0091-7,613(2002)030<0619:GOPATB>2.0.CO;2

Rogers, N. W., Davies, M. K., Parkinson, I. J., & Yirgu, G. (2010). Osmium isotopes and Fe/Mn ratios in Ti-rich picritic basalts from the Ethiopian flood basalt province: No evidence for core contribution to the Afar plume. *Earth and Planetary Science Letters*, *296*, 413, georem-id: 5149–422. https://doi.org/10.1016/j.epsl.2010.05.027

Rosenthal, A., Foley, S. F., Pearson, D. G., Nowell, G. M., & Tappe, S. (2009). Petrogenesis of strongly alkaline primitive volcanic rocks at the propagating tip of the western branch of the East African Rift. *Earth and Planetary Science Letters*, *284*, 236, georem-id: 3972–248. https://doi.org/10.1016/j.epsl.2009.04.036

Saha, A., Manikyamba, C., Santosh, M., Ganguly, S., Khelen, A. C., & Subramanyam, K. S. V. (2015). Platinum group elements (PGE) geochemistry of komatiites and boninites from Dharwar craton, India: Implications for mantle melting processes. *Journal of Asian Earth Sciences*, *105*, 300–319. https://doi.org/10.1016/j.jseaes.2015.01.020

Said, N., Kerrich, R., Maier, W. D., & McCuaig, C. (2011). Behavior of Ni-PGE-Au-Cu in mafic-ultramafic volcanic suites of the 2.7 Ga Kambalda sequence, Kalgoorlie Terrane, Yilgarn craton. *Geochimica et Cosmochimica Acta*, *75*, 2882, georem-id: 6027–2,910. https://doi.org/10.1016/j.gca.2011.02.032

Sakhno, V. G., Krymsky, R. S., Belyatsky, B. V., Shevchenko, S. S., & Sergeev, S. A. (2015). Mantle sources of Quaternary volcanism on Zhokhov Island (De Long Islands, East Arctic): Isotope-geochemical features of the basalts and spinel lherzolite xenoliths. *Doklady Earth Sciences*, *460*, 123–129. https://doi.org/10.1134/S1028334X1502004X

Schiano, P., David, K., Vlastelic, I., Gannoun, A.-M., Klein, M., Nauret, F., & Bonnand, P. (2012). Osmium isotope systematics of historical lavas from Piton de la Fournaise (Réunion Island, Indian Ocean). *Contributions to Mineralogy and Petrology*, *164*, 805, georem-id: 6673–820. https://doi.org/10.1007/s00410-012-0774-0

Schmidt, M. E., Grunder, A. L., Rowe, M. C., & Chesley, J. T. (2013). Re and Os isotopes of the central Oregon Cascades and along the arc indicate variable homogenization and mafic growth in the deep crust. *Geochimica et Cosmochimica Acta*, *109*, 345–364. https://doi.org/10.1016/j.gca.2013.02.003

Singh, T. D., Manikyamba, C., Subramanyam, K. S. V., Ganguly, S., Khelen, A. C., & Reddy, N. R. (2018). Mantle heterogeneity, plume-lithosphere interaction at rift controlled ocean-continent transition zone: Evidence from trace-PGE geochemistry of Vempalle flows, Cuddapah Basin, India. *Geoscience Frontiers*, *9*, 1809–1827. https://doi.org/10.1016/j.gsf.2017.12.013

Skovgaard, A. C., Storey, M., Baker, J. A., & Blusztajn, J. (2001). Osmium-oxygen isotopic evidence for a recycled and strongly depleted component in the Iceland mantle plume. *Earth and Planetary Science Letters*, *194*, 259–275. https://doi.org/10.1016/S0012-821X(01)00549-0

Sun, Y., Ying, J., Zhou, X., Shao, J., Chu, Z., & Su, B.-X. (2014). Geochemistry of ultrapotassic volcanic rocks in Xiaogulihe NE China: Implications for the role of ancient subducted sediments. *Lithos*, 208, 53, GeoReM-id: 8394–209, 56. https://doi.org/10.1016/j.lithos.2014.08.026

Szilas, K., Hoffmann, J. E., Schersten, A., Kokfelt, T. F., & Münker, C. (2013). Archaean andesite petrogenesis: Insights from the Graedefjord supracrustal belt, southern west Greenland. *Precambrian Research*, *236*, 1–15. https://doi.org/10.1016/j.precamres.2013.07.013

Szilas, K., Kelemen, P. B., & Rosing, M. T. (2015). The petrogenesis of ultramafic rocks in the >3.7 Ga Isua supracrustal belt, southern west Greenland: geochemical evidence for two distinct magmatic cumulate trends. *Gondwana Research*, *28*, 565–580. https://doi.org/10.1016/j.gr.2014.07.010

Tang, G.-J., Wyman, D. A., Wang, Q., Li, J., Baker, P. E., Zhao, Z.-H., & Sun, W.-D. (2012). Asthenosphere-lithosphere interaction triggered by a slab window during ridge subduction: Trace element and Sr-Nd-Hf-Os isotopic evidence from late carboniferous tholeiites in the western Junggar area (NW China). *Earth and Planetary Science Letters*, *329–330*, 84–96. https://doi.org/10.1016/j.epsl.2012.02.009

Tejada, M. L. G., Hanyu, T., Ishikawa, A., Senda, R., Suzuki, K., Fitton, J. G., & Williams, R. J. (2014). Re-Os isotope and platinum group elements of a focal zone mantle source, Louisville Seamounts Chain, Pacific Ocean. *Geochemistry Geophysics Geosystems*, *16*, 486, GeoReM-id: 9085–504. https://doi.org/10.1002/2014GC005629

Thebaud, N., Barnes, S.-J., & Fiorentini, M. L. (2012). Komatiites of the Wildara-Leonora belt, Yilgarn Craton, WA: The missing link in the Kalgoorlie Terrane? *Precambrian Research*, *196–197*, 234–246. https://doi.org/10.1016/j.precamres.2011.11.008

Theriault, R. J., Barnes, S.-J., & Severson, M. J. (1997). The influence of country-rock assimilation and silicate to sulfide ratios (*r* factor) on the genesis of the Dunka road Cu-Ni-platinum-group element deposit, Duluth Complex, Minnesota. *Canadian Journal of Earth Sciences*, *34*, 375–389. https://doi.org/10.1139/e17-033

Thompson, R. N., Ottley, C. J., Smith, P. M., Pearson, D. G., Dickin, A. P., Morrison, M. A., Leat, P. T., & Gibson, S. A. (2005). Source of the quaternary alkalic basalts, picrites and basanites of the Potrillo volcanic field, New Mexico, USA: Lithosphere or convecting mantle? *Journal of Petrology*, *46*, 1603–1,643. https://doi.org/10.1093/petrology/egi028

Upton, B. G. J., Skovgaard, A. C., McClurg, J., Kirstein, L. A., Cheadle, M., Emeleus, C. H., Wadsworth, W. J., & Fallick, A. E. (2002). Picritic magmas and the Rum ultramafic complex, Scotland. *Geological Magazine*, *139*, 437–452. https://doi.org/10.1017/S0016756802006684

Vye-Brown, C., Gannoun, A.-M., Barry, T. L., Self, S., & Burton, K. W. (2013). Osmium isotope variations accompanying the eruption of single lava flow field in the Columbia River flood basalt province. *Earth and Planetary Science Letters*, *368*, 183–194. https://doi.org/10.1016/j.epsl.2013.02.003

Walker, R. J., Shirey, S. B., & Stecher, O. (1988). Comparative Re-Os, Sm-Nd and Rb-Sr isotope and trace element systematics for Archean komatiite flows from Munro Township, Abitibi belt, Ontario. *Earth and Planetary Science Letters*, *87*, 1–12. https://doi.org/10.1016/0012-821X(88)90060-X

Walker, R. J., & Stone, W. E. (2001). Os isotope constraints on the origin of the 2.7 Ga Boston Creek flow, Ontario, Canada. *Chemical Geology*, *175*, 567–579. https://doi.org/10.1016/S0009-2541(00)00358-2

Wang, B., Chen, J., Xu, J., & Wang, L. (2014). Geochemical and Sr-Nd-Pb-Os isotopic compositions of Miocene ultrapotassic rocks in southern Tibet: Petrogenesis and implications for the regional tectonic history. *Lithos*, *208–209*, 237, GeoReM-id: 8383–250. https://doi.org/10.1016/j.lithos.2014.09.008

Wang, J., Hattori, K., & Stern, C. R. (2008). Metasomatic origin of garnet orthopyroxenites in the subcontinental lithospheric mantle underlying Pali Aike volcanic field, southern South America. *Mineralogy and Petrology*, *94*, 243–258. https://doi.org/10.1007/s00710-008-0017-2

Wang, Q., Li, Z.-X., Chung, S.-L., Wyman, D. A., Sun, Y.-L., Zhao, Z.-H., Zhu, Y.-T., & Qiu, H.-N. (2011). Late Triassic high-mg andesite/dacite suites from northern Hohxil, north Tibet: Geochronology, geochemical characteristics, petrogenetic processes and tectonic implications. *Lithos*, *126*, 54, georem-id: 6342–67. https://doi.org/10.1016/j.lithos.2011.06.002

Wang, R., Richards, J. P., Zhou, L.-M., Hou, Z., Stern, R. A., Creaser, R. A., & Zhu, J.-J. (2015). The role of Indian and Tibetan lithosphere in spatial distribution of Cenozoic magmatism and porphyry Cu-Mo deposits in the Gangdese Belt, southern Tibet. *Earth Science Reviews*, *150*, 68–94. https://doi.org/10.1016/j.earscirev.2015.07.003

Watanabe, S., Widom, E., Ui, T., Miyaji, N., & Roberts, A. M. (2006). The evolution of a chemically zoned magma chamber: The 1707 eruption of Fuji volcano, Japan. *Journal of Volcanology and Geothermal Research*, *152*, 1, georem-id: 1119–19. https://doi.org/10.1016/j.jvolgeores.2005.08.002

Waters, C. L., Day, J. M. D., Watanabe, S., Sayit, K., Zanon, V., Olson, K. M., Hanan, B. B., & Widom, E. (2020). Sulfide mantle source heterogeneity recorded in basaltic lavas from the Azores. *Geochimica et Cosmochimica Acta*, *268*, 422–445. https://doi.org/10.1016/j.gca.2019.10.012

Wei, T., Wang, S., Liu, F., Chu, Z., Wang, B., Chen, M., & Prichard, J. (2017). Archean-Paleoproterozoic lithospheric mantle at the northern margin of the north China craton represented by tectonically exhumed peridotites. *Acta Geologica Sinica (Dizhi-Xuebao)*, *91*, 2041–2057. https://doi.org/10.1111/1755-6724.13449

Widom, E., Hoernle, K. A., Shirey, S. B., & Schmincke, H.-U. (1999). Os isotope systematics in the Canary Islands and Madeira: Lithospheric contamination and mantle plume signatures. *Journal of Petrology*, *40*, 279–296. https://doi.org/10.1093/petroj/40.2.279

Widom, E., & Shirey, S. B. (1996). Os isotope systematics in the Azores: Implications for mantle plume sources. *Earth and Planetary Science Letters*, *142*, 451–465. https://doi.org/10.1016/0012-821X(96)00111-2

Woodland, S. J., Pearson, D. G., & Thirlwall, M. F. (2002). A platinum group element and Re-Os isotope investigation of siderophile element recycling in subduction zones: Comparison of Grenada, Lesser Antilles arc, and the Izu-Bonin arc. *Journal of Petrology*, *43*, 171–198. https://doi.org/10.1093/petrology/43.1.171

Workman, R. K., Hart, S. R., Jackson, M. G., Regelous, M., Farley, K. A., Blusztajn, J., Kurz, M. D., & Staudigel, H. (2004). Recycled metasomatized lithosphere as the origin of the enriched mantle II (EM2) end-member: Evidence from the Samoan volcanic chain. *Geochemistry Geophysics Geosystems*, *5*. https://doi.org/10.1029/2003gc000623

Xia, Y., Zhu, D., Wang, Q., Zhao, Z., Liu, D., Wang, L., & Mo, X. (2014). Picritic porphyrites and associated basalts from the remnant Comei large igneous province in SE Tibet: Records of mantle-plume activity. *Terra Nova*, *26*, 487–494. https://doi.org/10.1111/TER.12124

Xu, J., Suzuki, K., Xu, Y., Mei, H., & Li, J. (2007). Os, Pb, and Nd isotope geochemistry of the Permian Emeishan continental flood basalts: Insights into the source of a large igneous province. *Geochimica et Cosmochimica Acta*, *71*, 2104, georem-id: 3284–2,119. https://doi.org/10.1016/j.gca.2007.01.027

Ya, M. A. (2016). Platinum group elements in Permo-Triassic volcanics in West Siberia (the first data). *Russian Geology and Geophysics*, *54*, 664–670. https://doi.org/10.1016/J.Rgg.2013.06.002

Yang, H., Frey, F. A., Weis, D., Giret, A., Pyle, D. G., & Michon, G. (1998). Petrogenesis of the flood basalts forming the northern Kerguelen Archipelago: Implications for the Kerguelen plume. *Journal of Petrology*, *39*, 711–748. https://doi.org/10.1093/petroj/39.4.711

Yang, S., Huhma, H., & Lahaye, Y. (2015). Petrogenesis of the 2·77 Ga Monts de Cristal complex, Gabon: Evidence for direct precipitation of Pt-arsenides from basaltic magma. *Journal of Petrology*, *56*, 1285, georem-id: 8622–1,308. https://doi.org/10.1093/petrology/egv035

Yudovskaya, M. A., Tessalina, S., Distler, V. V., Chaplygin, I. V., Chugaev, A. V., & Dikov, Y. P. (2008). Behavior of highly-siderophile elements during magma degassing: A case study at the Kudryavy Volcano. *Chemical Geology*, *248*, 318, georem-id: 3751–341. https://doi.org/10.1016/j.chemgeo.2007.12.008

Zhang, J., Liu, Y., Ling, W., & Gao, S. (2017). pressure-dependent compatibility of iron in garnet: Insights into the origin of ferropicritic melt. *Geochimica et Cosmochimica Acta*, *197*, 356, GeoReM-id: 10381–377. https://doi.org/10.1016/j.gca.2016.10.047

Zhang, X., Wilde, S. A., Zhang, H., & Zhai, M. (2011). Early Permian high-K calc-alkaline volcanic rocks from NW inner Mongolia, North China: Geochemistry, origin and tectonic implications. *Journal of the Geological Society of London*, *168*, 525–543. https://doi.org/10.1144/0016-76,492,010-094

Zhao, J.-H., & Zhou, M.-F. (2013). Neoproterozoic high-Mg basalts formed by melting of ambient mantle in south China. *Precambrian Research*, *233*, 193, georem-id: 7683–205. https://doi.org/10.1016/j.precamres.2013.04.017